ABSTRACT

Title of Dissertation: Combinatorial Investigation of Intermetallics Using Electron-beam Deposition

Hiroyuki Oguchi, Doctor of Philosophy, 2008

Directed By: Professor Ichiro Takeuchi, Materials Science & Engineering

We have systematically studied subtle changes in physical properties of intermetallics using the combinatorial strategy where a large number of samples with systematically changed parameters can be rapidly studied. We have developed a new combinatorial electron-beam (e-beam) deposition chamber which allows us to perform layer-by-layer deposition as well as co-deposition. For my thesis, two particular topics of significant technological impacts involving intermetallic systems were investigated. They are exchange-coupled soft/hard magnetic bilayer systems and hydrogen storage Mg–(transiton metal) (TM) binary systems. The first topic is discussed in Chapter 2 – Chapter 4, and the second topic is duscussed in Chapter 5 – Chapter 7. Summary of the thesis work and future plans are discussed in Chapter 8.

We have studied the effect of magnetic parameters of the soft layer on the exchange coupling behavior of soft/hard magnetic bilayer systems. The magnetic parameters of the soft layer were systematically changed in a combinatorial manner by changing the composition of the soft layer. The exchange coupling behavior was monitored by M-H hysteresis loops taken by a magneto-optical Kerr effect (MOKE)

measurement set up. The MOKE M-H hysteresis loops successfully delineated the exchange coupling behavior dependence on the magnetic parameters.

We have also studied the effect of the crystallinity and grain-texturing of the hard layer on the exchange coupling behavior of hard/soft magnetic bilayer systems. The crystallinity and the degree of grain-texturing were controlled by growth temperature and the post-annealing process of the hard layer. The MOKE M-H hysteresis loops successfully revealed that attaining a single phase, single orientation hard layer is the key to achieving a good exchange coupling behavior.

We have developed a new infrared (IR) imaging set up to perform high-throughput screening of hydrogen storage properties of Mg-TM systems. In order to demonstrate the utility of the set up, we studied promising Mg-TM binary systems. We have fabricated Mg-TM binary composition spread thin films using the combinatorial e-beam chamber. For each composition, IR intensity as a function of measurement time were monitored by analyzing images collected continuously and periodically during measurements. The change in IR intensity curves successfully gave systematic trends in hydrogen absorption/desorption properties of Mg-TM composition spread thin films.

We have established a novel way to use an IR imaging and succeeded to measure propagation of hydride formation from the top of hydrogen storage thin film. IR images of thickness gradient $Mg_{0.95}Ti_{0.05}$ thin films enabled us to directly determine the propagation of the hydride formation front quantitatively.

COMBINATORIAL INVESTIGATION OF INTERMETALLICS USING ELECTRON-BEAM DEPOSITION

By

Hiroyuki Oguchi

Dissertation submitted to the Faculty of the Graduate School of the
University of Maryland, College Park, in partial fulfillment
of the requirements for the degree of
Doctor of Philosophy
2008

Advisory Committee:
Professor Ichiro Takeuchi, Chairman/Advisor
Professor Richard Greene
Professor John Cumings
Professor Samuel Lofland
Professor Lourdes Salamanca-Riba

Dedication

To my wife

ACKNOWLEDGEMENTS

I would like to acknowledge everyone who has helped me and everyone I have interacted with during the course of my research in the past five years. I could not have done this thesis without their help.

First, I would like to express my gratitude to my advisor Professor Ichiro Takeuchi. It was him who opened a gate of great experience to learn at the University of Maryland for me. His energetic and enthusiastic attitude to research has always inspired me. His abundant knowledge about science has helped me whenever I was in need of new ideas or directions. At the same time, his patience and kindness have always saved me from being discouraged and motivated me to work on difficult challenges. Moreover, his cheerful personality has made me feel at home even in serious discussions. I have been and will be truly happy to always be his student.

Second, I would like to express my great appreciation to Dr. Leonid Bendersky at National Institute of Standards and Technology (NIST). He has given me great opportunity to work at NIST. His expertise in materials research has played a key role in my gaining knowledge and skills. He has given me freedom, responsibility and at the same time great guidance. Thanks to his trust in me, I was able to manage many difficult experiments by my self. His detailed directions were often critical in navigating through difficult problems.

I would like to thank my research partners Antonio Zambano, Ming-hui Yu, and Jason Hattrick-Simpers. They have kindly shared a lot of experiments, measurements, and painful moments in our research. Especially, hard discussions

with Antonio Zambano have improved my skills to tackle difficult problems. I also would like to express my gratitude to other lab members: Kao-Shuo Chang, Olugbenga Famodu, Maria Aronova, Makoto Murakami, Chuan-Lan Lin, Shigehiro Fujino, Christian Long, Sung Hwan Lim, Dwight Hunter, Daisuke Kan, Naoyuki Taketoshi, Peng Zhao, Arun Luykx, Ryota Takahashi, and Debjani Banerjee. Their friendships have made my graduate life extremely fruitful.

I am grateful to Dr. Daniel Josell at NIST for his tremendous technical support for our combinatorial electron beam chamber. Without his help, I could not have done any deposition at all. I am also grateful to Dr. Edwin Heilweil at NIST for his kindness in performing infrared measurements. His knowledge of infrared has played an important role in interpreting the data.

Our collaborator Prof. Samuel Lofland at Rowan University has helped me greatly with magnetic measurements. His suggestions have shed important light on understanding of physics often hidden in the sea of combinatorial experimental data. Also, I was able to set up a MOKE system in our lab thanks to his assistance.

Our experiments on exchange-coupled bilayers were supported by the ONR/MURI project on exchange-coupled nanocomposites under Grant No. N00014-05-1-0497. We are indebted to Dr. Mihal Gross for her support and guidance. I'm grateful to all of the MURI collaborators involved in our experiments including Dr. Ping Liu, Dr. Zhong Lin Wang, and Dr. Yuzi Liu.

I am grateful to other NIST scientists and researchers including Dr. Alex Shapiro, Mr. Chris Amigo, Dr. John bonevich, Dr. Albert Davydov, Dr. Peter Schenck, Dr. Frank Gale, Dr. Kil-Won Moon, Dr. Chun Chiu, Dr. Mark Vaudin, as

well as Ms. Shari Tobery, and Ms. Jannet Williams. They have created great working environment for me at NIST.

Dr. Makoto Otani, as a friend and an experienced researcher, has personally given me many precious advices on research. I am deeply indebted to him.

I am grateful to Dr. Phil Piccoli of the Geology Department for his constant help with WDS measurement.

My student life has been supported by many university staffs: Dr. Kathleen Hart, Ms. Annette Mateus, Mr. Mike McNicholas, Ms. Kay Morris, and Ms. Olivia Noble in Department of Materials Science and Engineering, Dr. Dale Morey in Engineering Information Technology. They have helped me to overcome many problems I encountered during the course of my graduate life.

Finally, I give my thanks to my family. I was able to finish the long graduate student life with many ups and downs thanks to their constant and warm support. Of my family, I have to say special thanks to my wife. Her daily support was more than anything else the most important factor in continuously helping and encouraging me. I will forever cherish all the memorable moments I shared with her living in the United States.

The University of Maryland, College Park: this wonderful land had offered me the great opportunity to fulfill my Ph. D. dream. I am so honored to be a member of the alumni. I thank you forever.

Table of Contents

List of Tables

List of Figures

Chapter 1 Introduction to combinatorial approach to materials discovery and high-throughput techniques

In this chapter, the combinatorial approach is briefly reviewed. In the first half, the concept, advantages, its history, typical sample synthesis methods are quickly introduced. Then, the motivation for the development of the electron-beam (e-beam) deposition based combinatorial approach is discussed together with the high-throughput measurements used in our investigation. Finally, the chapter gives illustration of the power of the combinatorial approach with two examples we studied here.

1.1 Introduction to the combinatorial approach

Traditionally, new materials have been explored and discovered via the one-by-one trial-and-error method. New materials were generally not pursued until a satisfactory prediction of their properties was made either by inference from properties published in literature, or through theoretical calculations. This conventional approach is too slow and time-consuming for the modern competitive world where stringent demands for performance are made for new materials in a variety of technological fields. There is increasingly a need for a more efficient approach to discover new materials.

The concept of combinatorial synthesis, which allows thousands of different samples to be made in parallel, was developed accordingly. It was first developed in the pharmaceutical industry in 1980s to accelerate the discovery of new drugs. In this

approach, a large collection of samples with varying compositions are synthesized under the same condition, and they are processed and screened for specific applications. Once the desired properties of the specific materials systems are achieved in some compounds, they are analyzed in more detail, and subsequently large scale synthesis is pursued. Fig. 1.1 shows the flow process of a combinatorial synthesis experiment based on a thin film technique. This efficient synthesis strategy can potentially create an abundance of useful materials in a given experiment, and thus there is a strong impetus to carry out such experiments.

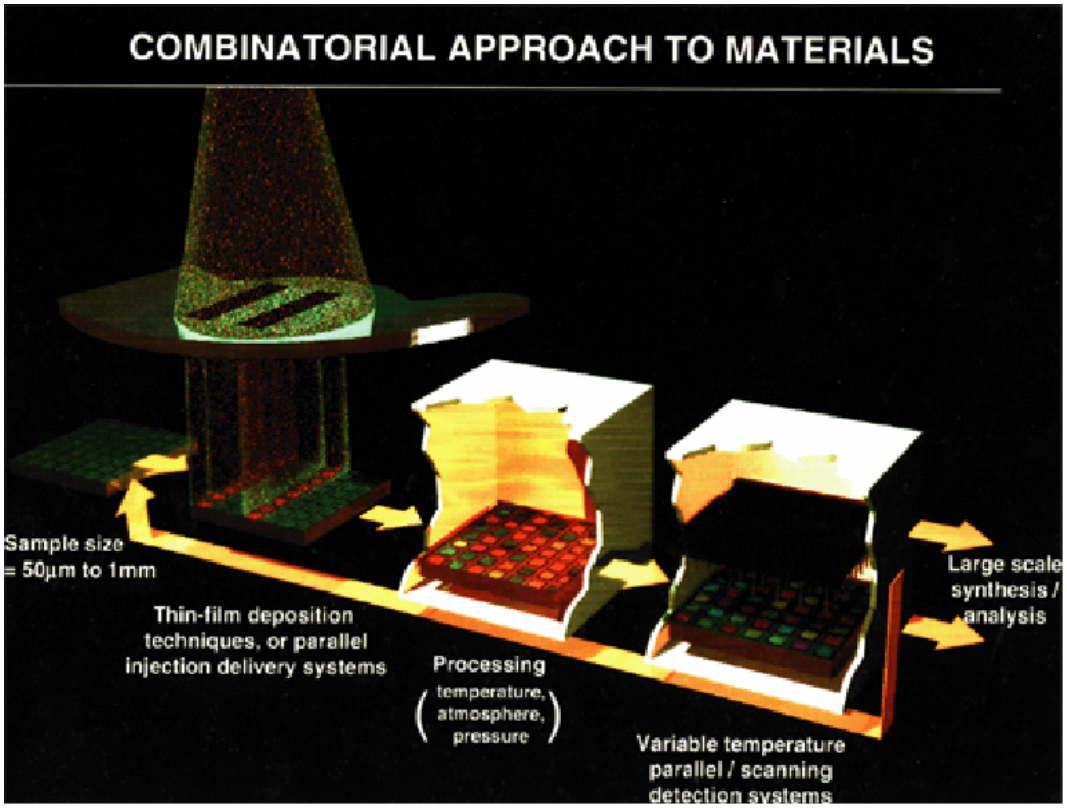

Fig. 1.1 The flow diagram of the concept of combinatorial approach to materials.

A bio-tech company, Affymax, founded by Peter G. Schultz in 1989, was the first commercial corporation to use the combinatorial synthesis approach to accelerate the exploration of catalytic antibodies. This approach has since been adopted by many companies in the pharmaceutical industry in the past decade. These efforts established the foundation for combinatorial synthesis of inorganic materials. In 1993, this approach was first extended to discovery of functional inorganic materials by Peter G. Schultz *et al*. [1, 2].

In almost any technological field where new materials are needed, there are an enormously large number of new compositions to be explored. Combinatorial synthesis provides the right platform to approach this problem. When one surveys the literature and history of materials science of inorganic compounds, he or she finds that most of the basic binary compounds have been explored, and most of their properties are known. But as soon as one moves to other multi-element compounds such as ternary or quaternary systems, he or she finds that a large fraction of all possible compounds (formed by combining different elements) remain unexplored. J. C. Phillips estimated that there were about 24,000 known inorganic materials at the end of 1980s. 16,000 of those are binary compounds, and only 8,000 are ternary and other multi-element compounds.[3] If one is simply to pick out any three or four elements (there are about 60 non-radioactive and non-gaseous elements) from the periodic table for forming different compounds, there are over 30,000 possible ternary combinations and 500,000 possible quaternary combinations. Clearly, there are an extremely large number of new compounds that are yet to be explored. Any effort to systemically explore them using the one-by-one traditional approach would

take a prohibitively long time. Combinatorial synthesis offers a potential solution to the problem.

If one looks at the process of development of materials in modern society, there is a trend that more complex compounds tend to have more desirable physical properties. For example, Fig. 1.2 shows the critical temperature (T_c) of superconductors as a function of number of elements required to make the compounds.[3] It clearly shows that T_c increases for more complex compounds consisting of a larger number of elements.

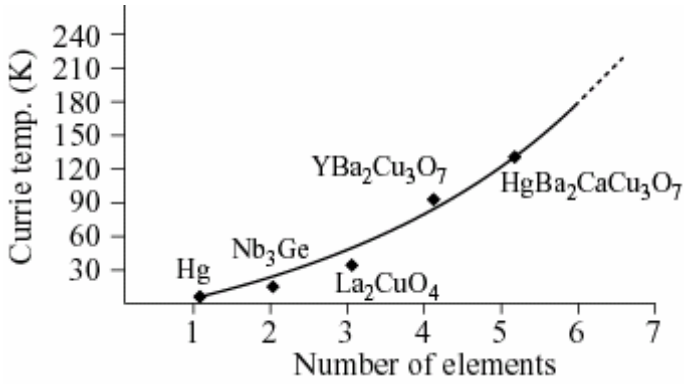

Fig. 1.2 The correlation between materials complexity (reflected in the number of elements required to make up the compounds) and a physical property (T_c) for superconductors.

Materials scientists are increasingly taking advantage of the efficiency of combinatorial synthesis and extending it to accelerate the discovery of complex compounds in a variety of areas such as dielectrics/ferroelectric materials,[4-7] ferromagnetic materials,[8-10] colossal magnetoresistant materials,[11,12] polymers,[13-15] catalysts, [16,17] and luminescent materials.[2,6] In addition to

serving the immediate materials need of industry, combinatorial techniques can also be used to tackle fundamental issues of materials physics and chemistry. For example, composition spread and phase-diagram mapping experiments have proved to be highly effective in rapidly uncovering and delineating the complex composition-structure-property relationships of unknown materials systems.[18-20] The knowledge gained from such a library can be very subtle, and some compositional trends are nontrivial to detect unless one were systematically studying the variation in a continuous manner. This underscores the strength of the combinatorial approach as applied to investigation of interdependence of various physical parameters.

The success of combinatorial synthesis experiments is largely dependent on the capability and availability of high-throughput characterization techniques. Recognizing that optimized materials properties often exist in a multidimensional parameter space, it is desirable to be able to map the properties of materials not just as a function of composition, but also as functions of other parameters such as processing conditions (temperatures, background gas, etc.) at the same time.[21,22] Such a comprehensive characterization strategy is becoming increasingly more important in future combinatorial investigations.

1.2 Combinatorial thin film synthesis

Combinatorial synthesis has been used to make libraries of both bulk materials and thin films. Thin film techniques are more popular because they have several advantages over bulk materials: 1) readily available thin film deposition techniques lend themselves to library synthesis techniques; 2) physical parameters such as thickness and composition can be easily and systematically controlled; 3) the

smaller amount of materials required make thin film techniques more economical and efficient.

There are two major methods to create large compositional variation in combinatorial libraries and composition spreads: (1) solution-based synthesis and (2) solid-state thin films. We used the latter methods because they allow us to control the composition much easier than the former one. The basic premise of library fabrication is that compositional variation is achieved across a library through spatially selective materials synthesis and deposition. In the next subsections, the way to deposit spatially selective thin films and some common solid-state thin film fabrication techniques are reviewed.

1.2.1 Spatially selective thin film deposition schemes using shadow masks

The key feature of a combinatorial thin film synthesis is a set of physical masks for defining the film deposition site through physical shadowing inside of a deposition chamber. By synchronizing the deposition source switching with mask movements, synthesis of a number of composition varying materials can be coordinated on a single substrate (Fig. 1.3(a), (b), (c)). In another mode of operation, by automating the motion of the shadow mask during depositions, one can fabricate atomically mixed, epitaxially grown, continuous composition spreads. Fig. 1.3(d), (e), (f) illustrate this synthesis procedure for epitaxially grown composition spread of $A_{1-x}B_x$ ($0 \leq x \leq 1$). More details of combinatorial synthesis will be discussed in Chapter 3 and Chapter 4.

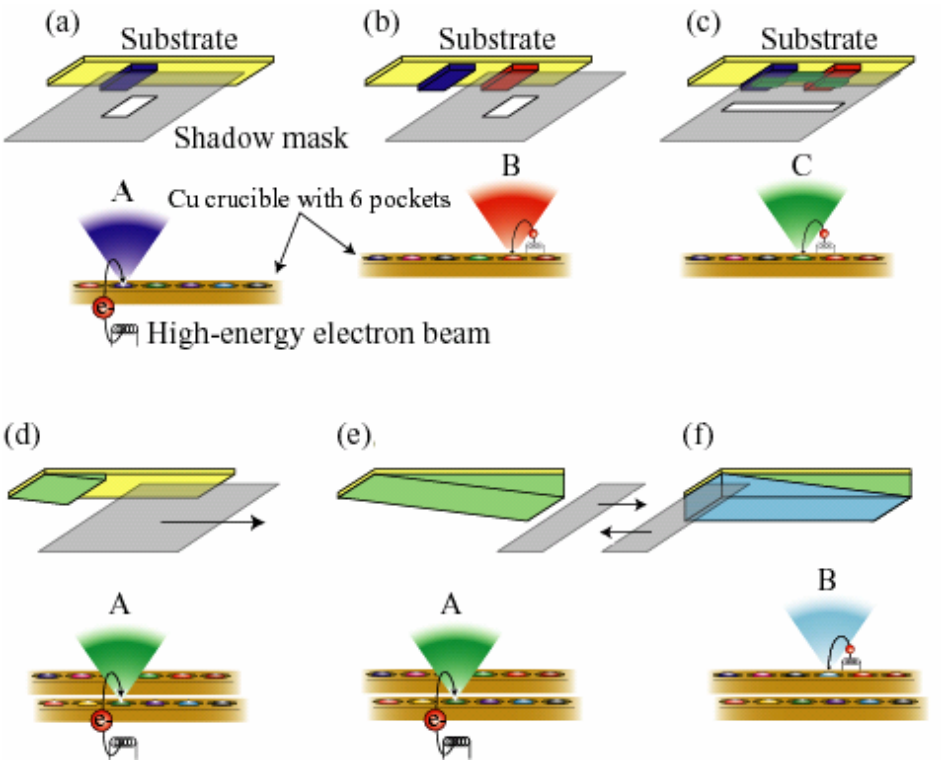

Fig. 1.3 Combinatorial thin film synthesis. (a)-(c) Three successive depositions of three different materials spatially coordinated on a single substrate. (d)-(f) Synthesis procedure of $A_{1-x}B_x$ ($0 \leq x \leq 1$) composition spread thin film.

1.2.2 Solid-state thin film fabrication techniques

There are many thin film synthesis techniques such as electron beam (e-beam) deposition, pulsed laser deposition (PLD), sputtering, chemical vapor deposition (CVD), and molecular beam epitaxy (MBE). They can all be applied to fabrication of thin film combinatorial libraries. Each technique has intrinsic advantages and disadvantages. Here we provide a brief survey of some of these techniques.

(1) With sputtering, metal or insulator films can be deposited. In this technique, a plasma is created by discharging a gas which is guided to bombard the target. Argon is typically used as the gas. ac or radio-frequency (RF) power is applied

to avoid Ar^+ build-up in the target surface. The major disadvantages of this technique are: 1) due to different vapor pressures of various elements, the film compositions do not necessarily reflect the target compositions, and thus controlling the stoichiometry of deposited films can be problematic; 2) it is sometimes difficult to deposit uniform thickness thin film across large areas; and 3) ion-bombardment can degrade the film quality.

In performing combinatorial investigation of metallic alloy systems, co-deposition off of two or more spatially separated sources can be used to obtain samples with a natural composition gradient (Fig. 1.4).[40,43,51] The co-sputtering technique is very effective for this purpose. The advantage of co-sputtering is that the material is intimately mixed in the as-deposited state, and the deposition time can be relatively short. However, co-sputtering creates "natural" composition spreads, meaning that composition variation across a wafer is not controlled *a priori*. Large wafers are often required (up to 3~4'' wafers), and the variation needs to be determined in a separate composition mapping measurement.

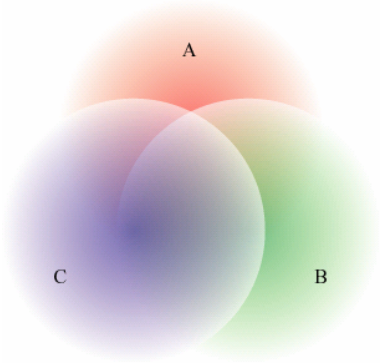

Fig. 1.4 Schematic of co-deposition off of three spatially separated sources on a wafer.

(2) Chemical vapor deposition (CVD) is the most popular industry-adopted technique. Its advantages include high deposition rate, large area uniformity, and ability to apply to large-area processing. However, due to the complex precursor chemistry involved, controlling stoichiometry is often a big issue. It is also not an evaporative technique, and thus, simple spatially selective deposition schemes using shadow masks for library fabrication can not be applied.

(3) In molecular beam epitaxy (MBE), deposition sequence of atomic layers is precisely controlled in order to fabricate high quality thin films in ultra high vacuum (better than 10^{-10} Torr). However, contamination from source materials, difficulty to replenish sources, and expensive price of the source cell can be problematic.

(4) Pulsed laser deposition (PLD) is one of the modern techniques of depositing thin films, where a high-power laser is focused onto the source target surface to evaporate source. PLD is a very simple, versatile, and an efficient technique for thin film fabrication. It is especially suitable for metal oxides because of its capability to transfer the stoichiometry of the multi-component target materials to the substrate in a non-equilibrium manner, not dictated by the vapor pressure of individual component element. However, splashing of macroscopic particles during laser-induced evaporation is a major concern as well as difficulty to deposit uniform films over areas larger than ~ 1 cm^2.

Using the PLD technique, composition spreads with precisely controlled composition along spreads are often fabricated using layer-by-layer deposition, where a series of unit-cell thick wedge-shaped layers are deposited alternately using a moving shutter (Fig. 1.5). Examples of experiments include mapping of magnetic

properties in $La_{1-x}Sr_xMnO_3$,[2] continuous bandgap change in $Zn_{1-x}Mg_xO$,[3] and dielectric properties in $Ba_{1-x}Sr_xTiO_3$.[4] One disadvantage of this technique is that in order to fabricate a ~100 nm thick sample for appropriate physical property characterization, a large number of repeated deposition steps (each less than 1 nm thick) are needed, requiring hours of deposition. In addition, due to the not-line-of-sight nature of PLD deposition, mechanical parts such as chains connected to the axes of motors to control the motion of the physical shadow masks can be coated, and hinder the precise mask motion control over time.

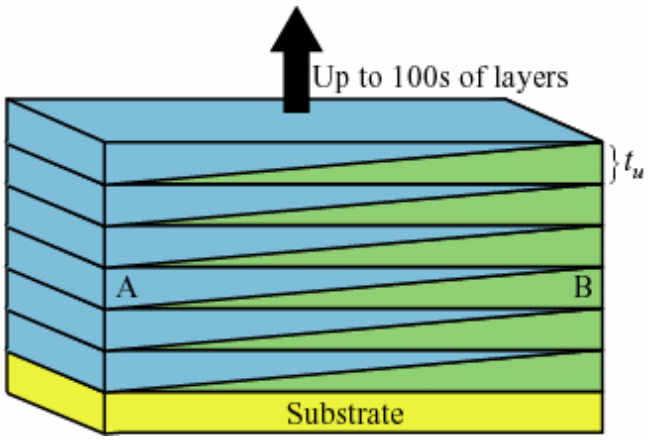

Fig. 1.5 Synthesis scheme of the spread. The total thickness of n x 100 nm can be obtained after repeating 100s of layers. In order to realize ideal inter-layer mixture, t_u, the thickness of each wedge, is typically less than 0.5 nm.

(5) Electron beam (e-beam) deposition is an evaporative technique, where atoms from a heated source are transferred to a substrate located a distance away. Resistive heating of sources for evaporation suffer from the limitation of relatively low input power levels. E-beam heating eliminates this problem and has, therefore, become the preferred vacuum evaporation technique for deposition of high melting-point materials.

In our studies discussed in this thesis, we chose the e-beam deposition for combinatorial synthesis because this technique has many advantages as discussed in the next section.

1.3 Combinatorial thin film library fabrication by electron-beam deposition

We have developed a new combinatorial electron beam (e-beam) deposition chamber (Fig. 1.6(a)). The advantages of this technique compared to sputtering and

PLD are that we can perform both layer-by-layer deposition and co-deposition. In addition, this technique is advantageous to: 1) sputtering because it can deposit uniform films across a large area, and there is no risk of degradation of the thin film quality due to the ion-bombardment; 2) PLD, because there is no splashing of macroscopic particles, uniform film deposition across large areas, and precise composition control due to its line-of-sight deposition nature.

The base pressure of our e-beam evaporation chamber is about 3×10^{-8} Torr. The inner dimensions of the chamber are 55 cm (length) x 55 cm (width) x 85 cm (height) (Fig. 1.6(b)). Its source-substrate distance is 75 cm. The sample stage allows us to heat the sample up to ≈ 650 ºC. The chamber has two e-beam guns with two movable copper crucibles, each of which contains 6 pockets to load metal targets, and two computer-controlled movable shadow masks. This allows us to deposit up to 36 different combinations of metallic layers without breaking the vacuum on one 1.5 cm x 1.5 cm substrate. The in-situ deposition rate of each source is measured using a crystal deposition rate monitor. By synchronizing the motion of the two shadow masks orthogonally placed over substrate holder (for x and y directions) with the deposition rates of the targets, we can fabricate thin films in precisely controlled areas, with controlled compositions, and with controlled thicknesses in each perpendicular directions.

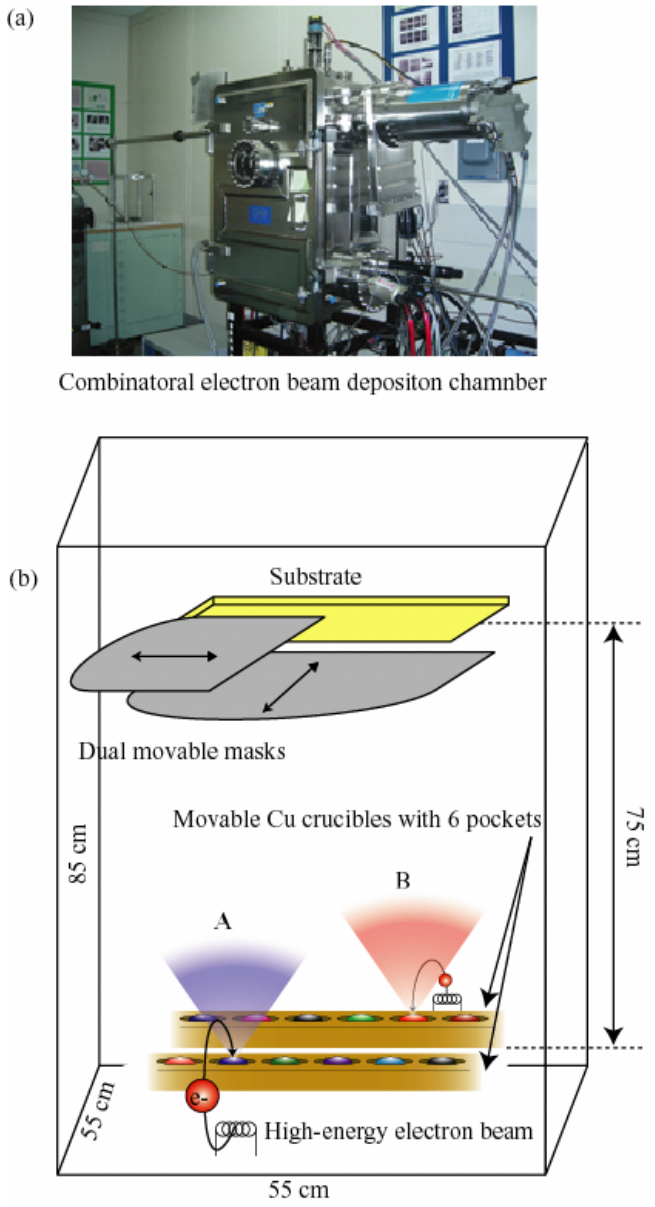

Fig. 1.6 Picture of the electron beam (e-beam) chamber (left) and schematically drawn inside of the chamber (right).

1.3.1. Epitaxial thin films

Unlike bulk materials, thin films must be grown on substrates, and the film properties are highly influenced by the properties of the interface between the film

and the substrate. Relevant properties include presence of microstructural defects, and strain induced by the substrate. If a film is grown in such a way so that its orientation directly reflects that of the substrate, the growth mode is called epitaxial. When a film is grown on the same material as the substrate (for instance, (100) MgO film on (100) MgO substrate), it is called a homoepitaxial growth. Otherwise, epitaxial growths are heteroepitaxial. When there is a lattice mismatch between the film and the substrate, elastic tensile or compressive stress will occur in the film for thickness less than the critical thickness (t_c). When the film thickness is thicker than t_c, dislocations will start to develop to reduce the stress, and the film gets relaxed.

The kinetics of the nucleation mechanism in thin film growth plays a dominant role in determining the phase formation and the microstructure of thin films. Fig. 1.7 shows three common growth modes observed in epitaxial thin films.

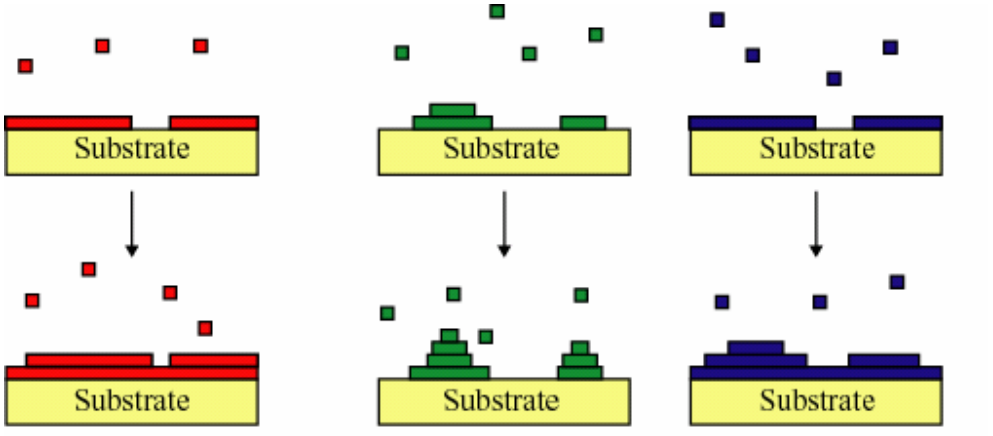

(a) Frank - van der Merwe (b) Volmer - Weber (c) Stranski - Krastanov

Fig. 1.7 The three modes of heteroepitaxial thin film growth (1) Frank - van der Merwe (2) Volmer - Weber (3) Stranski - Krastanov.

(1) Frank - van der Merwe mode is the two dimensional (2D) monolayer growth mode. This mechanism takes place when the surface mobility of atoms is high.

(2) Volmer - Weber mode is the three dimensional (3D) nucleation growth mode which takes place when there is a significant lattice mismatch between the substrate and the film.

(3) Stranski - Krastanov mode is the mode where the 2D monolayer (wetting layer) growth takes place followed by the growth of 3D nucleation islands. In this mode, the strain energy will continue to increase as the film thickness approaches the critical thickness (t_c). When the thickness reaches the critical thickness, the strained energy exceeds the activation energy, and dislocations start to form resulting in the 3D islands which in turn lower the elastic energy abruptly.

As discussed later, some of our CoPt magnetic thin films showed the Frank-van der Merwe mode growth, and others Stranski-Krastnov mode growth. This difference might be due to the run to run slight variation of growth temperature or the subsequent heat treatment we applied.

1.4 High-throughput measurement techniques

In any combinatorial investigation, having the correct characterization tool is critical. Without an appropriate high-speed screening technique, combinatorial libraries serve little purpose. In our research, the x-ray diffractometry and energy/wavelength x-ray dispersive spectroscopy equipped with a moving stage are used to study the crystallinity plus crystal orientations, and composition of the thin

films, respectively. For high-speed screening of magnetic exchange coupling between hard and soft magnetic layers, a magneto-optical Kerr effect (MOKE) measurement was employed. For rapid investigation of the hydrogen absorption/desorption of hydrogen storage materials, infrared (IR) imaging was employed.

1.4.1 X-ray diffraction

We used x-ray diffraction (XRD) to study the crystallinity and crystal orientation of the thin films. Diffraction from a set of periodic lattice planes of a crystal occurs when it satisfies the Bragg law:

$$2d \sin\theta = n\lambda \qquad (1.1)$$

where d is the space between the periodic lattice planes, θ the angle between the incident beam and the crystal plane, n the integer, and λ is the wavelength of the incident beam.[42] In our research, we used a Bruker D8 x-ray diffractometer with an area detector using CuK_α radiation (0.15418 nm). Combination of a typically 0.5 mm diameter x-ray beam and an automated x-y moving stage enables us to screen a large number of points on one sample quickly. In addition, since the area detector enables us to integrate intensity along the χ direction, more information can be obtained from the area detector than from a standard point detector.

1.4.2 Energy dispersive x-ray spectroscopy and wavelength dispersive x-ray spectroscopy

In order to measure the composition distributions of our thin film combinatorial samples, we used an energy dispersive x-ray spectroscopy (EDS) or wavelength dispersive x-ray spectroscopy (WDS). In these techniques, a high energy beam of electrons hit the specimen, and characteristic x-rays of each element of the specimen are emitted. The element is determined by the energy and wavelength of the characteristic x-ray in EDS and WDS, respectively. Quantitative analysis is performed for each element by analyzing the intensity of the characteristic x-rays. In our research, we used JSM-6390 for EDS and JXA-8900 for WDS. Both machines are equipped with the *xy* moving stages which enable us to rapidly map a large number of points on an individual wafer/substrate sample.

1.4.3 Magneto-optical Kerr effect

We have used the magneto-optical Kerr effect (MOKE) for soft/hard magnetic bilayer samples to study the exchange coupling between the magnetic layers. MOKE is a magneto-optical effect in which polarization of the light is rotated by the presence of magnetic field in the magnetic materials when the light is reflected.[27] The rotation angle of the polarization of the light is almost proportional to the averaged magnetization of the magnetic materials. Thus, one can map the magnetic hysteresis loop by sweeping an applied magnetic field. From this, one can obtain the saturation magnetization (through calibration) and coercive field values. Our MOKE set up (Fig. 1.8) uses a 635-nm laser (Blue Sky Research, CLAS-635-

025-WL00), whose beam diameter is focused down to a less than 0.5 mm diameter spot. The relatively small beam spot together with a scanning stage allows us to measure many points on each sample. The magnet for the MOKE set up can apply up to 2 T, which is large enough to magnetically saturate most of our hard layers. It is important to note that MOKE is a surface sensitive measurement.

Fig. 1.9(a) shows cross-sectional schematic of three soft/hard bilayer samples with different thickness of the soft layer. This illustrates that more and more reflection of the laser occurs in the soft layer with increasing thickness of the soft layer. Fig. 1.9(b) shows magnetization of Fe/CoPt soft/hard magnetic bilayer samples measured using MOKE as a function of the thickness of the Fe soft layer (t_{Fe}). The magnetization value increased with increasing t_{Fe} until it reached the penetration depth of the laser, at which point the laser beam is exclusively reflected by the soft layer. As the magnetization value saturats at around t_{Fe} = 10 nm, the penetration depth of the laser used here is empirically determined to be about 10 nm.

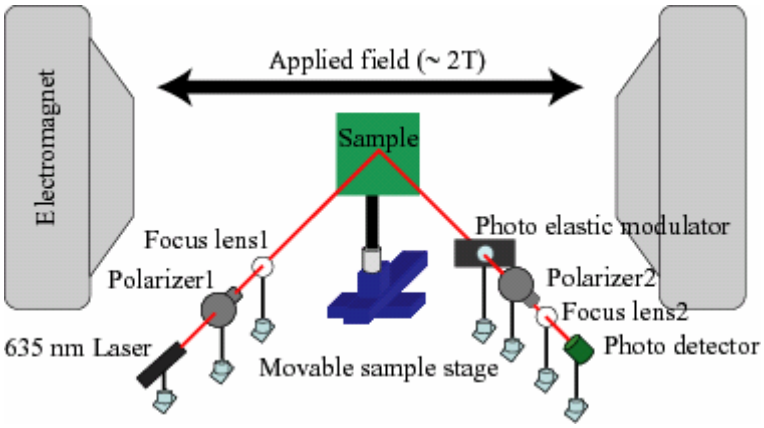

Fig. 1.8 Magneto-optical Kerr effect measurement set up.

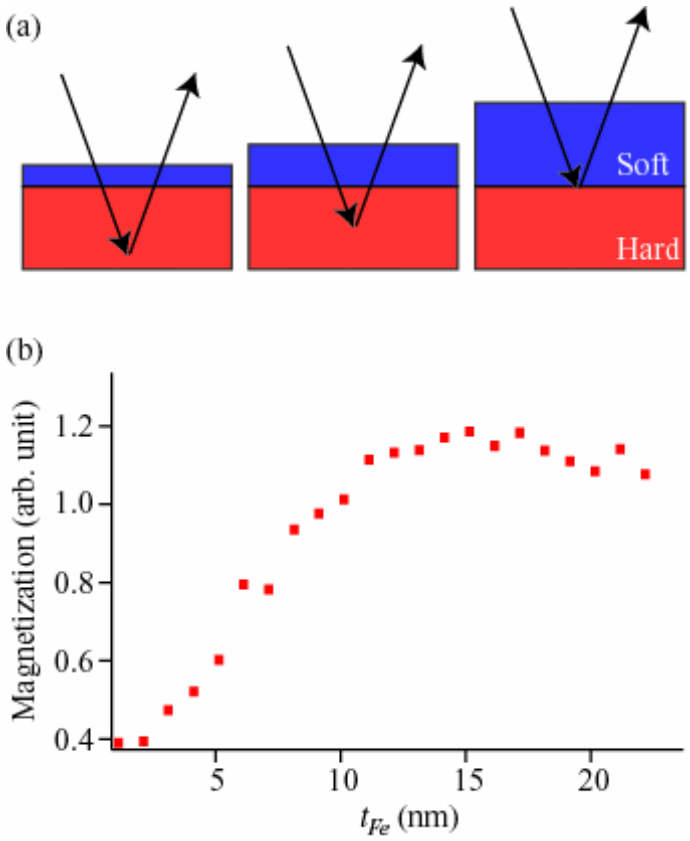

Fig. 1.9 (a) Cross-sectional schematic of three soft/hard magnetic bilayer samples with different thickness of the soft layer. Arrows indicate direction and penetration depth of the laser. (b) Magnetization of Fe/CoPt soft/hard magnetic bilayer vs thickness of the Fe soft layer (t_{Fe}) measured using MOKE.

1.4.4 Infrared emission imaging

We have used infrared (IR) imaging to study hydrogen absorption/desorption properties of composition spreads. IR emissivity of a solid is expected to change with hydrogen absorption/desorption as a result of changes in its electronic and vibrational energy states, as well as its crystallographic structure and surface morphology.[28] The application of IR emission imaging to hydrogen absorption/desorption studies was reported recently by General Electric and General Motors groups.[5,6] We have

developed a new in-house IR imaging set up (Fig. 1.10). The IR camera we employed here integrates IR emission within a wide range of wavelength (1.0 – 5.5 μm) from the sample to increase total intensity, and it has a two dimensional position sensitive detector with 256 x 256 pixels. Its spatial resolution in our typical use is about 100 μm, which makes it possible to study the hydrogen absorption/desorption of a large number of small points with various parameters on each sample. More details of the instrument will be discussed later in Chapter 7.

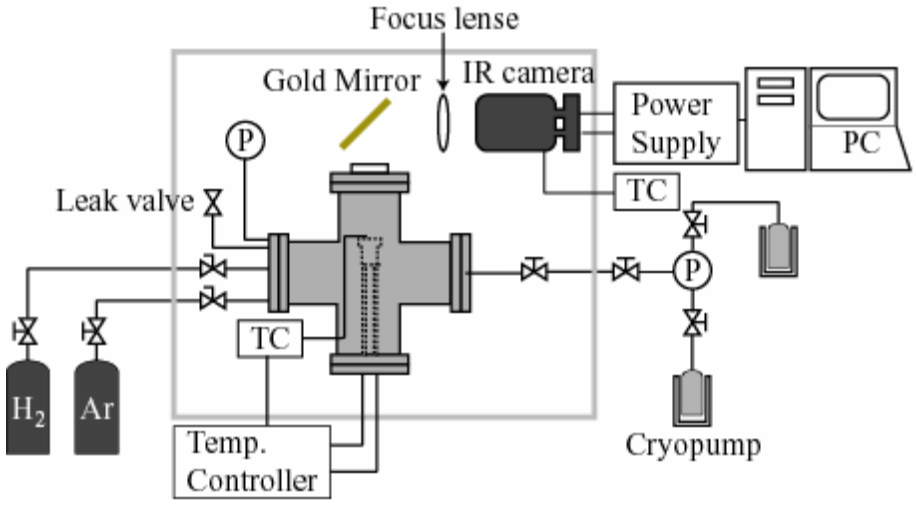

Fig. 1.10 In-home infrared (IR) imaging set up.

1.5 Two examples of rapid mapping of physical properties

Before going into the details of our investigations, I would like to illustrate the power of the combinatorial approach in rapidly delineating subtle changes in physical properties of materials systems as a continuous change of composition for two experiment examples we studied: the exchange-coupled soft/hard magnetic bilayer systems and the Mg-based composition spread hydrogen storage thin films.

The details will be discussed later in Chapter 3 - 5 for the exchange-coupled magnets and in Chapter 7 - 9 for the hydrogen storage materials.

1.5.1 Exchange coupled nano-composite magnet

The first example which exhibits the effectiveness of the combinatorial approach to rapidly map physical properties was the systematic investigation of exchange coupling of magnetic soft/hard bilayer systems as various parameters are continuously varied across combinatorial samples. For instance, on a square 1 cm x 1 cm sample chip, along one direction, the composition of the soft phase was varied, and along the perpendicular direction, the thickness of the soft layer was changed (Fig. 1.11). Each small point on one sample can have unique exchange coupling between the soft layer and the hard layer because it has unique thickness and/or unique composition of the soft layer. To study the subtle and systematic change in the exchange coupling, the magnetic *M-H* hysteresis loop of each point of the sample was measured using MOKE, and plotted together for the entire sample (Fig. 1.12). It is extremely difficult for traditional one-by-one experiments to obtain so many *M-H* hysteresis loops with systematically changed magnetic parameters under the same sample preparation conditions. Moreover, physical meaning of change in *M-H* hysteresis loops is hard to understand by simply comparing several *M-H* hystersis loops. However, a large number of *M-H* hysteresis plotted together as shown in Fig. 1.12 can be obtained using the combinatorial approach, and we can begin to deduce subtle yet important insight about relationships between physical parameters which play dominant roles in exchange coupling.

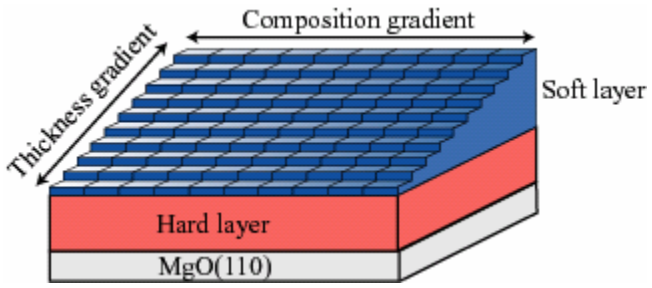

Fig. 1.11 Scehmatic of a typical design of a soft/hard magnetic layer combinatorial sample.

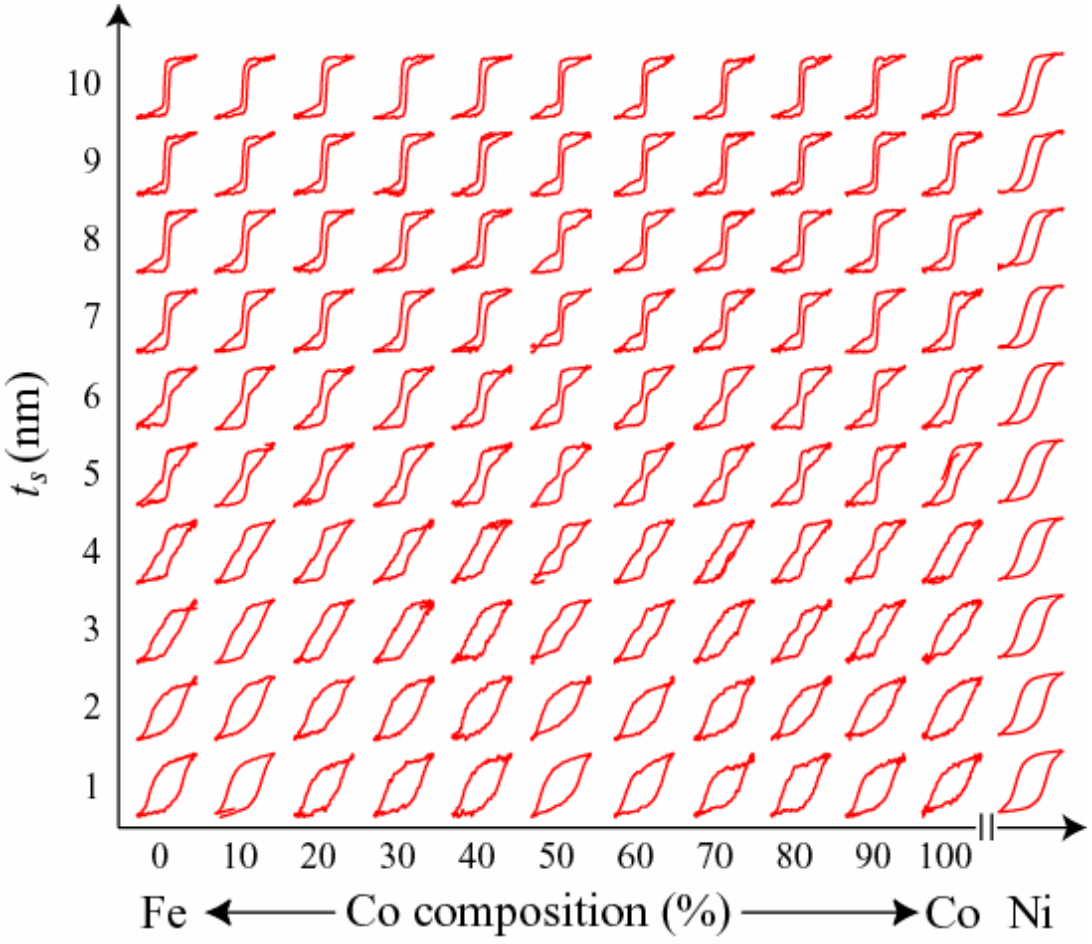

Fig. 1.12 A large number of MOKE M-H loops corresponds from all discrete points on one combinatorial sample with different magnetic parameters.

1.5.2 Hydrogen storage materials

The second example which exhibits the unique strength of the combinatorial approach to rapidly map physical properties is the systematic investigation of hydrogen absorption/desorption of Mg-(transition metal) (TM) in binary composition spreads where compositions are continuously varied along longer edge (about 1cm length) of the substrate (Fig 1. 13). Using a combinatorial sample of this type, we can study subtle and systematic change in hydrogen absorption/desorption properties with changing composition by collecting the IR images of the entire composition spread sample during a set of measurement (the schedule of the measurement is noted on top of Fig. 1.14). After collecting the IR images, the IR intensity of each point of the sample with unique composition is extracted from a large number of IR images collected during a set of measurement, and plotted together for the entire sample against the measurement time (Fig. 1.14). As in the case for the first example, it would be difficult for traditional one-by-one experiments to obtain so many IR intensity curves with systematically changed parameters under the same sample preparation conditions, and the physical meaning of change in the IR intensity curves is hard to obtain by simply observing several curves. However, as discussed in details in Chapter 8, a large number of IR intensity curves plotted together as in Fig. 1.14 can be obtained only if we use the combinatorial approach, and such a plot allows us to study important properties-composition relationships including kinetics and equilibrium hydrogen pressure/temperature of hydrogen absorption/desorption.

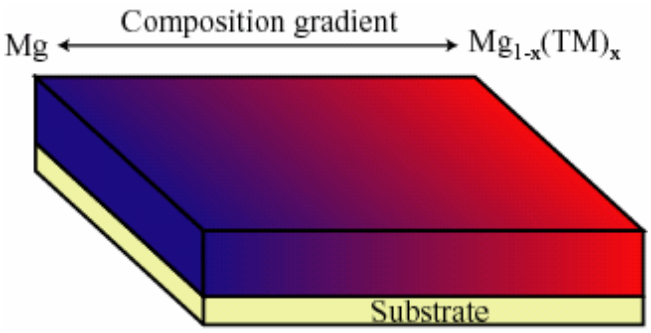

Fig. 1.13 Top view of Mg – (Transition metal) (TM) composition spread sample.

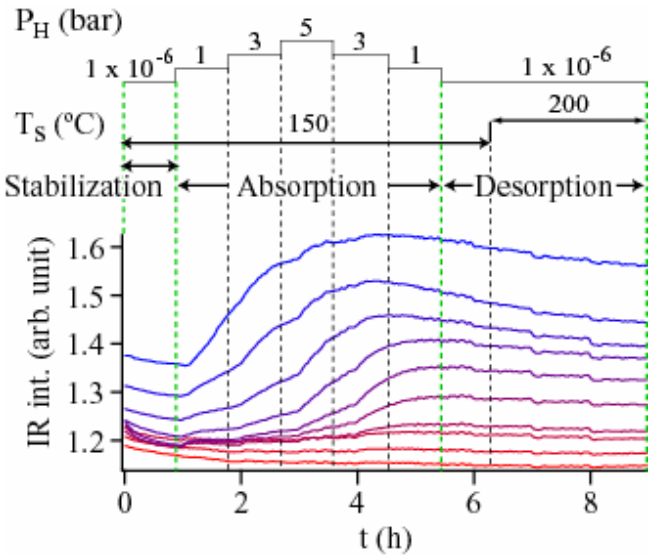

Fig. 1.14 Normalized infrared (IR) intensity curves from multiple points with various compositions. Curves are offset.

Chapter 2 Permanent magnets and the new strategy to enhance their energy products

We devote Chapter 2 to Chapter 4 for discussions of investigation of the exchange-coupled nano-composite permanent magnets. In Chapter 2, we will review the basic properties of soft magnets and hard magnets. A particular attention is paid on permanent magnets. After introducing some applications of permanent magnets, the maximum energy product $(BH)_{max}$, which is one of the most important physical properties of the permanent magnets, is introduced together with related physics behind it. The exchange-coupled nano-composite permanent magnets are introduced as one of the most promising ways to enhance $(BH)_{max}$ together with the magnetic parameters which play dominant roles in the exchange-coupling. Finally, a soft/hard magnetic bilayer system is introduced as an ideal model system to investigate the exchange coupling behavior.

2.1 Soft magnets and hard magnets

From the application point of view, ferromagnets can be broadly classified into soft and hard magnetic materials. Soft magnets have large permeability and small coercive field (H_c). For example, relative permeability ($\overline{\mu}$) and H_c of permalloy, which is a typical soft magnetic material, is 8000 and 0.05 Oe, respectively. On the other hand, hard magnets have small $\overline{\mu}$ and large H_c. For example, $\overline{\mu}$ of Alnico 5, which is a typical hard magnetic material, is too small to be defined, and H_c is 550 Oe.[29] As a result of over centuries of materials research, a variety of magnetic

materials have been discovered and developed. The characteristics of existing magnetic materials range from extremely soft to extremely hard. Fig. 2.1 shows the distribution of relative permeability and H_c for various magnetic materials. [29,30]

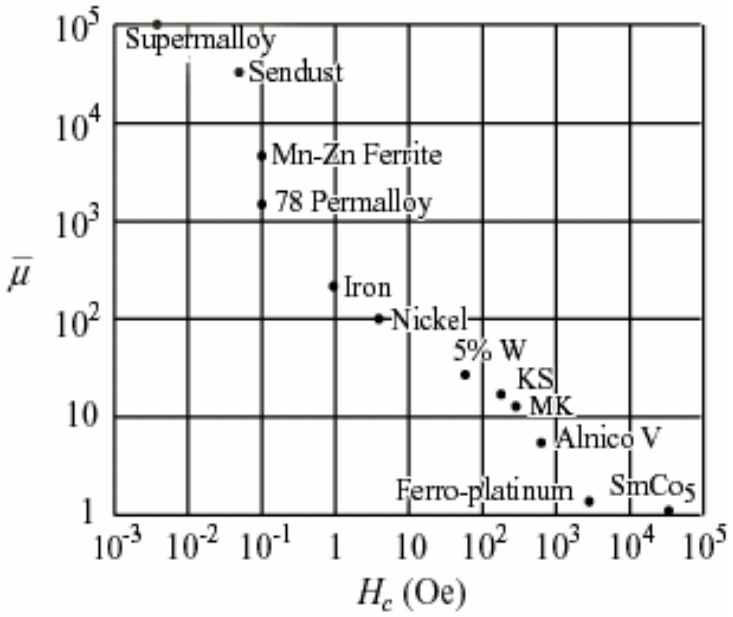

Fig. 2.1 Relative permeability and coercive field of various magnetic materials (after C. Kittel[30]). Permalloy is an alloy of Fe and Ni. Sendust is an alloy of Fe, Si, and Al. KS steel is an alloy of Fe with Co, W, Cr, and C. MK steel is an alloy of Fe, Ni, and Al.

2.2 Permanent magnets

An ideal permanent magnet is a ferromagnetic material which can maintain its high remanent magnetization while it is subjected to internal or external demagnetizing fields or to changes in temperature.

2.2.1 Applications

Permanent magnets are unique in their ability to deliver high magnetic flux into the air gap of a magnetic circuit without any continuous expenditure of energy. Because of their versatility and relatively low cost to manufacture them, permanent magnets are ubiquitous for a variety of applications.[31,32]

The most important application for permanent magnet materials is in direct current (dc) rotating motors. The high energy product of modern rare earth magnets is often used to produce a greater air gap flux density in a d.c. motor, which yields significant improvement in the motor's output torque.

The most notable application of these rare earth permanent magnets are in computer hard disk drives. The development trend in hard disk drives is ever towards greater miniaturization, which led to the early use of Sm_2Co_7 and then $Nd_2Fe_{14}B$ in brushless dc spindle motors, which carry the rigid disk platters.

The higher energies which can be stored in modern permanent magnets afford reduction in size and weight, which are attractive in a wide range of portable devices. It was the portable cassette player that provided the first significant market for $SmCo_5$ in the early 1980s. $Nd_2Fe_{14}B$ is increasingly used in automobile audio speakers, where the multiple speakers employed in a vehicle yield a worthwhile net saving in weight.

A specialized but an important application of permanent magnets is in sensors. While a sensor does not require a particularly large magnet to operate, the high energy densities of the rare earth materials are used to advantage to increase the sensitivity of the device.

2.2.2 Origin of coercive field

Magnetic anisotropy is the dependence of the internal energy on the direction of spontaneous magnetization. Generally, the magnetic anisotropy energy term carries information about the crystal symmetry of the material, and this is called magnetocrystalline anisotropy. The magnetocrystalline anisotropy is the origin of the large H_c in rare-earth magnets. Provided that the magnetic material has a cubic crystal lattice structure, such as iron, the magnetocrystalline anisotropy energy is commonly written as

$$E_k = \frac{K}{4}\sin^2 2\theta \tag{2.1}$$

where θ is the angle between the magnetic moment and its preferred crystallographic direction called the easy axis, and K is the first anisotropy constant. Applying the external field to the direction opposite to the saturation magnetization, the material has additional energy due to the external field written as

$$E_f = -\mu_0 M_s H \cos\theta \tag{2.2}$$

where H is the applied field. The total energy stored will be the sum of E_k and E_f:

$$E = \frac{K}{4}\sin^2\theta - \mu_0 M_s H \cos\theta \tag{2.3}$$

A permanent magnet can withstand an external field until it reaches the critical magnitude at which the magnetization will flip over into the opposite direction. This occurs when the rate of change of energy reverses, which can be determined from

$$\frac{d^2E}{d\theta^2} = 2K\cos 4\theta - \mu_0 M_s H\cos\theta = 0 \tag{2.4}$$

With $\theta = 0$, Equation (2.4) is zero when

$$H_c = \frac{2K}{\mu_0 M_s} \tag{2.5}$$

As indicated by Equation (2.5), this theoretical value of the coercive field is proportional to the first anisotropy constant K. In general, the permanent magnets possess large K, and thus H_c's of the permanent magnets are large.

2.2.3 Permanent magnet as energy source

Permanent magnets can be utilized as energy sources since they have ability to deliver magnetic flux into the air gap of a magnetic circuit without any continuous expenditure of energy. If we use the permanent magnets as energy sources, the magnetic filed (*H*) points opposite to the magnetic flux density (*B*) in the permanent magnets. This happens because there is a demagnetizing field generated by magnetization of the permanent magnets. Thus, point on the second quadrant *B*-*H* curve defines the condition of the permanent magnets in real applications.

2.2.4 Capacity of a permanent magnet as an energy source

Provided that magnetic flux is delivered into the airgap of the magnetic circuit shown in Fig. 2.2, where P stands for the soft magnet and S the hard magnet, the energy stored in this system is

$$U = \frac{1}{2}\iiint \boldsymbol{B} \cdot \boldsymbol{H} dv \tag{2.6}$$

We can restrict the integration range to the air gap G region and the soft magnet S in order to evaluate the capacity of the permanent magnet. Since the relevant volume consists of cross-sectional area *S* and the finite length along the circuit, Equation (2.6) can be rewritten as

$$U = \frac{1}{2}\int_{G\&S} BSH\, ds = \frac{1}{2}\Phi \int_{G\&S} H\, ds \tag{2.7}$$

Considering line integral of the magnetic field along the magnetic circuit is

$$\oint Hds = 0 \tag{2.8}$$

then we have

$$\oint_{G\&S} Hds = -\oint_{P} Hds \tag{2.9}$$

Therefore, Equation (2.7) becomes

$$U = -\frac{1}{2}\Phi\int_{P} Hds = -\frac{1}{2}\int_{P} \boldsymbol{B}\cdot\boldsymbol{H}dv \tag{2.10}$$

where the integration is taken over the volume of the permanent magnet. Equation (2.10) indicates that the capacity of the permanent magnet is higher if it has larger $-\boldsymbol{B}\cdot\boldsymbol{H}$ per unit volume and larger volume.

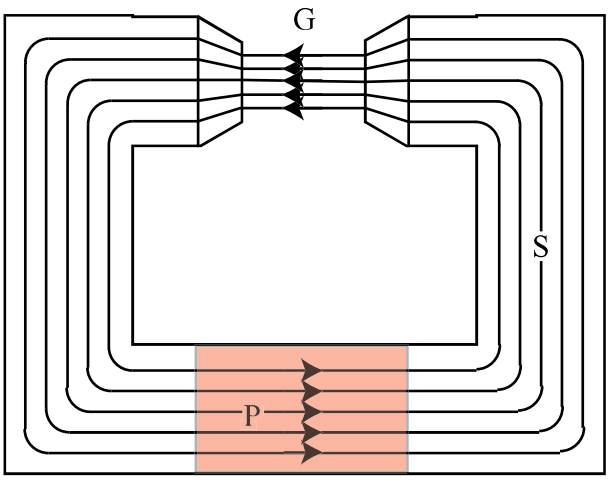

Fig. 2.2 Magnetic circuit containing a permanent magnet (after S. Chikazumi[29]).

2.3 Maximum energy product

Provided that the permanent magnet has demagnetization shown in Fig. 2.3, we can more effectively utilize the permanent magnet at point A, where $B\cdot H$ product is maximum, than at point A' or A''. The value of $B\cdot H$ product at A is called the maximum energy product ($(BH)_{max}$). The $(BH)_{max}$, which is twice the maximum magnetostatic energy available from a magnet of optimal shape, is the

most common figure of merit for permanent magnets.[33] The theoretical limit for the $(BH)_{max}$ can be expressed as

$$(BH)_{\max} = \mu_0 \left(\frac{M_s}{2} \right)^2 \tag{2.11}$$

This theoretical limit is obtained if $|H_c| > M_s/2$. In order to enhance $(BH)_{max}$, there are three ways: enhance the residual magnetization (M_r), enhance H_c, and making shape of the hysteresis loop as square as possible. In addition, it also works to make the ratio of the residual magnetization to the saturation magnetization (M_r/M_s) as close to 1 as possibly by means of magnetic anisotropy et. al. Since one can't control the value of M_r so much, what one can primarily do for the permanent magnet to enhance the $(BH)_{max}$ is increasing the H_c.

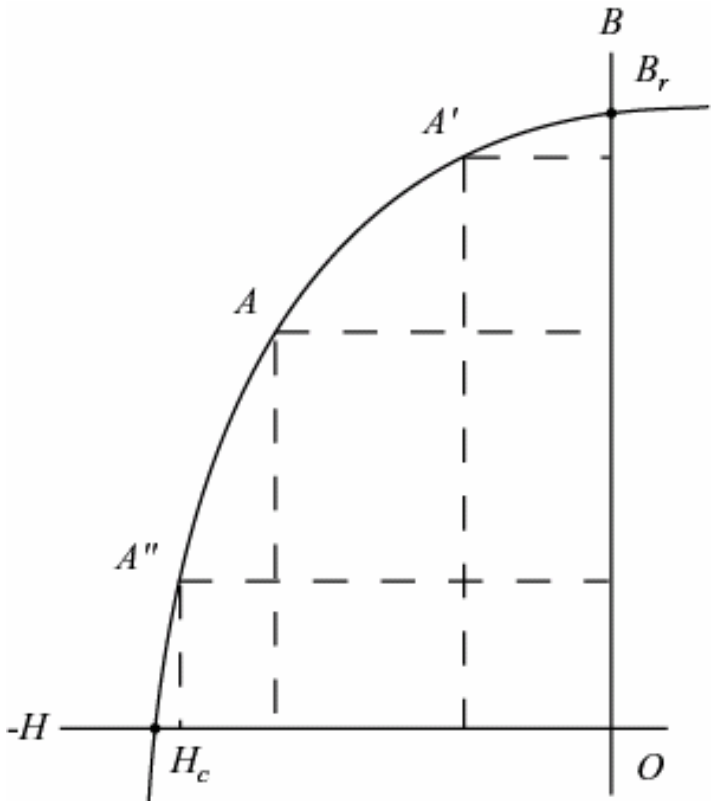

Fig. 2.3 Demagnetizing curve of a permanent magnet (after S. Chikazumi[29]).

2.3.1 History of the maximum energy product of permanent magnets

The history of development of permanent magnets can be monitored by the increase of $(BH)_{max}$ as a function of the year of discoveries. Fig. 2.4 is a semi-logarithmic plot of the highest $(BH)_{max}$ values versus time from 1880.[34] The first class of materials used was steel, which consisted mostly of iron with carbon, chromium, tungsten, or cobalt as the principal additives. Even though M_s is large, $(BH)_{max}$ is limited because of their small H_c. Alnicos are thermally treated aluminum-nickel-iron alloys and were the next class of materials to advance $(BH)_{max}$. The shape anisotropy of the particles is responsible for the H_c being more than a factor of two larger than those of the best steels. Over the past three decades, $(BH)_{max}$ has been

increased by rare-earth (R) – transition-metal (TM) materials in which the R component provides most of the magneto-crystalline anisotropy, while the magnetization arises principally from the TM sublattice. The $(BH)_{max}$ as large as 33 MGOe (263 kJ/m^3) has been obtained in Sm-Co based alloys, which are typically $SmCo_5$ and Sm_2Co_{17}.

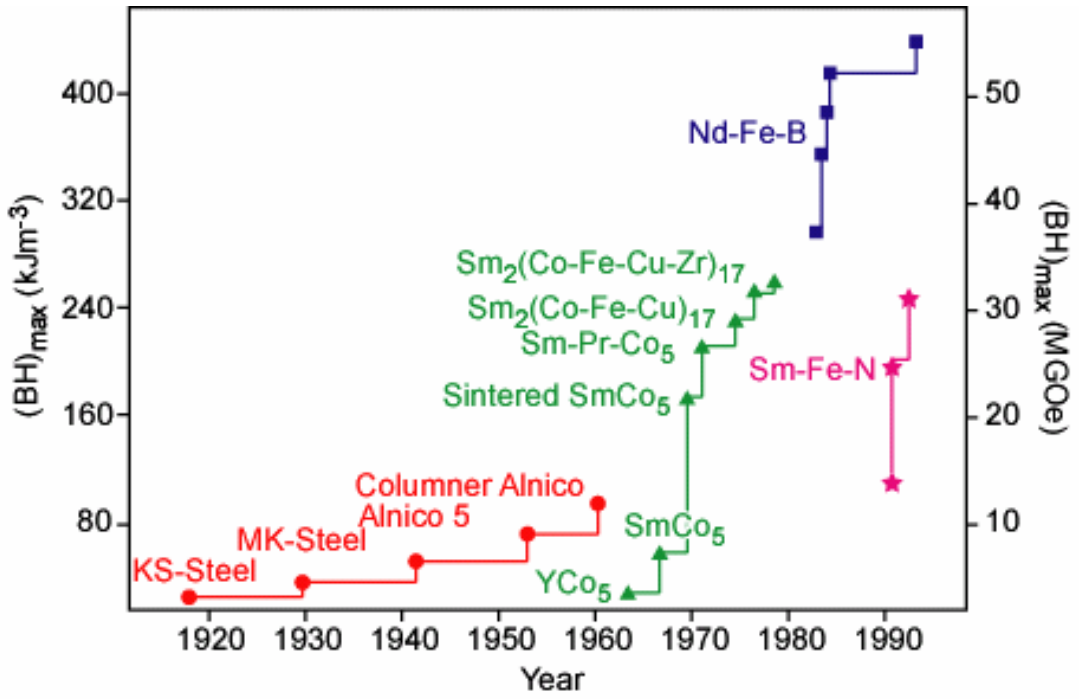

Fig. 2.4 Chronological trend of the maximum energy product $(BH)_{max}$ achieved in various permanent-magnet materials.

2.3.2 Current highest $(BH)_{max}$ Nd-Fe-B

Although a combination of R and TM is considered to be the best type of materials for the high-performance permanent magnets, one can inquire as to why R must be Sm and TM must be Co. Nd and Pr are very abundant in ordinary ores of the rare earths. Moreover, both elements have larger magnetic moments than Sm. Fe is

almost inexhaustible compared to Co, and, in most metallic substances, Fe possesses a larger magnetic moment than Co. However, none of the binary Nd-Fe or Pr-Fe compounds exhibited the magnetic properties required for obtaining a good permanent magnet. Following a vast amount of work, researchers gave up an R-Fe binary compounds, and have explored R-Fe-X ternary systems with various elements as X, and discovered a compound, $Nd_2Fe_{14}B$, which boosted the $(BH)_{max}$ up to 50 MGOe (400 kJ/m^3).[35-39]

2.4 Exchange-coupled nano-composite permanent magnets

As mentioned in 2.3.1, conventional single phase permanent magnets have little room to enhance $(BH)_{max}$ by means of enhancing M_r. However, the exchange-coupled nano-composite permanent magnets can enable us to drastically enhance the total B_r of the system since they consist of not only the hard phase but also the soft phase, which has large saturation magentization.

In such exchange-coupled magnets, the soft phases are pinned to the hard-magnet phases at the interfaces by the exchange interaction while the center of the soft magnets phases can rotate in a reversed magnetic field. Such magnets are characterized by enhanced remanent magnetization and reversible demagnetization curves since the soft phases will rotate back into alignment with the hard phases when the applied field is removed. It is for this specific and quite typical magnetic behavior, in a sense resembling a mechanical spring, that the exchange-coupled magnets have come to called the exchange-spring magnets.[40]

Analytical micromagnetic calculations theoretically predicted that $(BH)_{max}$ as high as 110 MGOe (880 kJ/m^3)[41] should be attainable by the exchange-coupled magnets which is more than twice the reported $(BH)_{max}$ in the present state of the art Nd-Fe-B magnets.

2.4.1 Gibbs free energy of exchange-coupled soft/hard magnetic bilayer system

The behavior of the exchange coupling between the soft phase and the hard phase is determined by the Gibbs free energy of the soft/hard magnetic systems.[42-44] In the soft/hard magnetic systems, each phase has three micromagnetic parameters: the anisotropy constant (K), the exchange stiffness (A), and the saturation magnetization (M_s). To simplify the theoretical study of the exchange coupling behavior, let's suppose we have the soft/hard magnetic bilayer system, the moments of hard layer and the soft layer are perpendicular to the x axis, and that two component layes have uniaxial anisotropy with the parallel easy axes both lying in the film plane along the z axis (as schematically depicted in Fig. 2.5).[45] In the case of an applied magnetic field H opposite to the z axis, the expression of the Gibbs free energy can be written as

$$G = \sum_{i=s,h} \int_0^{d^i} \left[A_i \left(\frac{d\theta}{dx} \right)^2 + K_i \sin^2 \theta - H \cdot M_s^i \right] dx \qquad (2.13)$$

where indexes s and h refer to the soft and the hard layer, respectively, and $x = 0$ denotes the surface plane of the soft layer. $x = d^s$ denotes the thickness of the soft layer, *and* $x = d^h$ denotes the thickness of the hard layer. The polar angle θ is defined as the angle enclosed by the polarization and the z-axis. Since the layers are assumed to spread homogeneously to infinity in the z- and y-direction, θ becomes a function of x alone. Though the task is nontrivial, by solving this nonlinear equation, we can theoretically calculate the distribution of the polar angle θ and study the behavior of the exchange coupling.

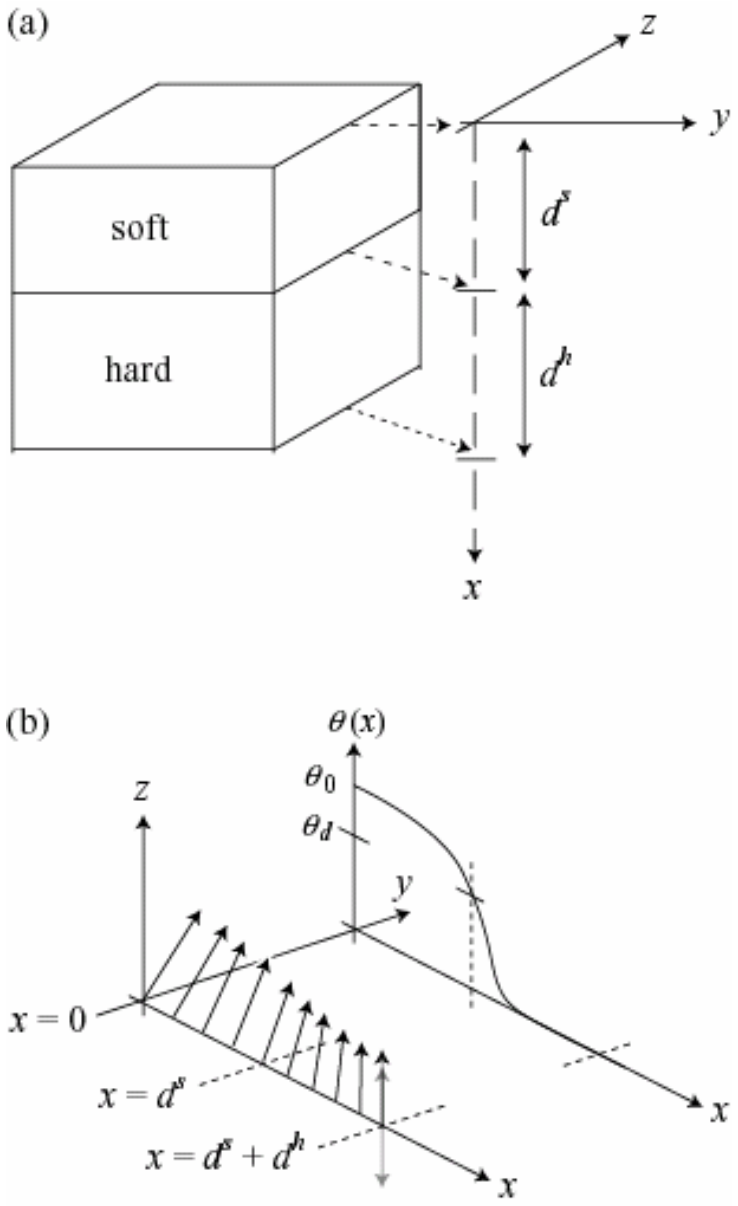

Fig. 2.5 (a) Model of magnetic soft/hard bilayer. The bilayer is assumed to spread to infinity in the *z*- and *y*-direction. (b) Typical distribution of the magnetization. In the foreground of the sketch, the orientation of the magnetic moment density is shown. $x = d^s$ and $x = d^h$ denote the thickness of the soft layer and the hard layer, respectively. θ_0 and θ_d are the polar angle defined as the angle enclosed by the polarization and the *z*-axis at $x = 0$ and $x = d^s$ The background shows the property to be calculated – the polar angle of the magnetization orientation (after T. Leineweber [45]).

2.4.2 Example of exchange-coupled magnets

The requirement of the exchange-coupled nanocomposite magnets that both the hard and the soft phases are controlled at the nanometer scale, to ensure efficient exchange coupling, has posed significant materials synthesis challenges. However, there have been some reports of successful synthesis.[46,47] For example, H. Zeng *et. al.* reported the fabrication of exchange-coupled nanocomposites using nanoparticle self-assembly.[48] In this approach, both FePt and Fe_3O_4 particles are incorporated as nanometer-scale building blocks into binary assemblies. Subsequent annealing converts the assembly into FePt-Fe_3Pt nanocomposites, where FePt is the magnetically hard phase and Fe_3Pt is the soft phase (Fig. 2.6).

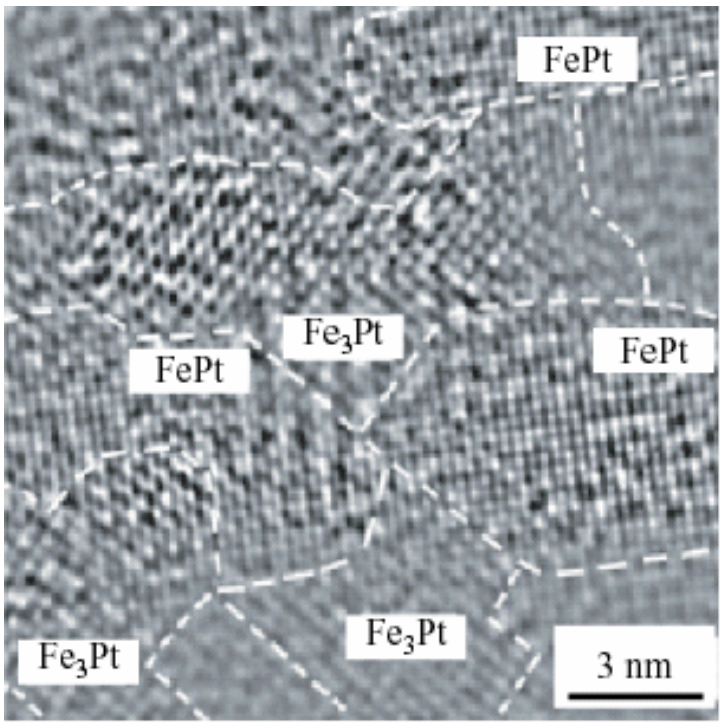

Fig. 2.6 A typical HRTEM image of an annealed FePt-Fe_3Pt composite. The FePt and Fe_3Pt phases are both present as different materials domains within the composite, with each component having a dimension of about 5 nm, showing a modulated FePt-Fe_3Pt spatial distribution. Here, the FePt (ordered f.c.t. structure) and Fe_3Pt (ordered f.c.c. structure) phases were identified by their different [001] projected image, owing to their different composition modulation periodicities.

2.4.3 Problem statement

Although large enhancement of $(BH)_{max}$ is theoretically predicted, currently reported experimental $(BH)_{max}$ values of nanocomposite magnets are far below the theoretically predicted ones. This suggests that the coupling behavior between the hard and the soft magnet needs to be improved. In order to achieve better coupling,

there have been some theoretical and empirical work carried out to elucidate how important factors such as interface conditions,[49] soft-hard volume fraction,[50] dependence on the microstructures,[43,51] can alter the coupling mechanism.[40,42,45,52,53] However, the lack of understanding of the detailed mechanism of the exchange coupling hinders the large enhancement of $(BH)_{max}$.

2.5 Soft/hard magnetic bilayer model

Experimentally, in order to obtain better understanding of the detail mechanism of the exchange coupling, it is necessary to study the exchange coupling behavior while systematically controlling the factors such as roughness of the interface, dimension, composition and/or crystallinity of the soft phase and the hard phase. However, in general, controlling such factors of the bulk nano-composite magnets is a formidable task. On the other hand, by modeling the interface of the bulk magnet by using the thin film soft/hard magnetic systems, we can control the interface properties relatively easily. This is the reason why we used the thin film soft/hard magnetic bilayer model system (Fig. 2.7). We implemented the combinatorial approaches to study the dependence of the exchange coupling behavior on: 1) the micromagnetic parameters (Chapter 3), 2) the grain-mixture of the CoPt hard layers (Chapter 4), and 3) the interface roughness and the grain-size of the CoPt hard layers (Chapter 5).

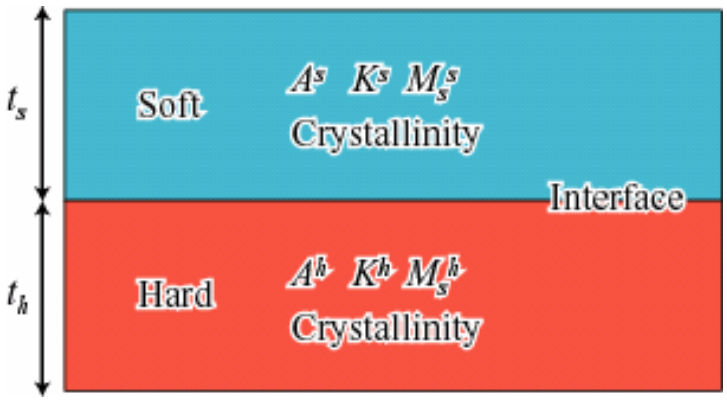

Fig. 2.7 A schematic of the soft/hard magnetic bilayer model system. Key parameters are noted on the schematic. *A*, *K*, *M*, and *t* are the exchange stiffness, the anisotropy constant, the saturation magnetization, and the thickness, respectively. The soft layer and the hard layer are denoted by superscript *s* and *h*.

Chapter 3 Effect of magnetic parameters on exchange coupling

3.1 Introduction

So far, there has been no report of successful experimental realization of theoretically predicted large enhancement of $(BH)_{max}$. The reason for this is mainly due to the lack of understanding of the detail mechanism of the exchange coupling. Therefore, in order to deepen our understanding of the mechanism, we first study dependence of the exchange coupling on various magnetic parameters.

There are some theoretical studies reported to date, but there is only limited experimental evidence to confirm the models. For instance, through a simple analysis, Kneller and Hawig[40] have given a rough estimate of the critical dimension of the soft layer which is ideally coupled to the hard layer and concluded that it is mainly determined by the domain-wall thickness of the hard layer. On the other hand, it has been shown that under specific limits, one can arrive at expressions for exchange field (H_{ex}) which depend only on soft layer parameters.[42,52] Other models, such as those by Skomski and Coey[54] and Leineweber and Kronmüller,[45] are more comprehensive and take into account the properties of both the hard and the soft layers. Because of the large number of variables involved in these ferromagnetic-bilayer systems, the ideal way to obtain an overall picture of their behavior, and compare the result to various models, is through analysis of a large number of samples where each variable is separately and continuously changed. First, by

keeping the hard layer parameters fixed, we mainly studied the effect of the soft phase parameters on the exchange coupling.

There are three magnetic parameters of the soft phase: the exchange stiffness A, the anisotropy constant K, and the saturation magnetization M_s (Equation (2.13)) which determine the micromagnetic Gibbs free energy, *i. e.* behavior of the exchange coupling. In order to study the effect of changing the soft phase parameters on the exchange coupling behavior, we independently and systematically varied the composition and the thickness of the soft layer on a single substrate.

3.2 Experiment

3.2.1 Fabrication of soft/hard combinatorial bilayer systems

Different combinations of soft/hard layer compositions and thicknesses consisting of (Fe_xCo_{1-x}) $(0 \leq x \leq 1)$ / CoPt(30 nm), Ni / CoPt(30 nm), Fe / CoPt(30 nm), (Fe, Co, and Ni) / Sm_2Co_7(96 nm), and Ni / Sm_2Co_7(96 nm) were generated on five thin-film samples. The bilayer systems were grown on 15 x 15 mm^2 or 7.5 x 15 mm^2 MgO (110) substrates by dual-gun electron-beam evaporation at a background pressure of approximately 3 $x10^{-8}$ Torr.

The CoPt hard magnetic layers were grown using a Pt (1 nm) buffer layer at 450 or 500 °C. For the latter case, the hard layer was post-annealed at 500 °C for 15 min. Following this, in both cases, the substrate temperature was decreased at a rate of 5 °C/min to 100 °C. The increase in the substrate deposition temperature resulted in an increase in the coercive field H_c from ≈ 0.64 to ≈ 1 T. Sm-Co films (96 nm) were grown on a Cr (20 nm) buffer layer at 320 °C. To complete the bilayers,

polycrystalline Fe and Co soft layers were deposited at 150 °C on the CoPt layer and at 70 °C on the Sm_2Co_7 layer. The different compositions of Fe_xCo_{1-x} ($0 \leq x \leq 1$) were achieved by controlling the deposition rates of the co-evaporated elemental Fe and Co sources. Typical soft layer deposition rates ranged from 0.01 to 0.04 nm/s. To prevent oxidization, the samples were capped by a 7.5 nm-thick Au layer deposited at room temperature.

Along one direction, the composition of the soft phase was varied, e.g., from pure Fe to pure Co, and along the perpendicular direction, the thickness of the soft layer was changed. For the (Fe_xCo_{1-x}) ($0 \leq x \leq 1$) / CoPt(30 nm) sample, the soft layer composition was varied in 11 steps and the thickness t_s was increased from 1 to 14 nm in 14 steps. In this manner, we can obtain up to 150 different combinations of soft layer composition and thickness on a single sample chip. For the other samples, only single compositions were deposited and t_s was smoothly increased from 0 to ≈ 7 nm. We now use "spot" to denote each small region of a sample in which the composition and thicknesses of the soft layer are nominally constant. A schematic of a typical bilayer sample is shown in Fig. 3.1.

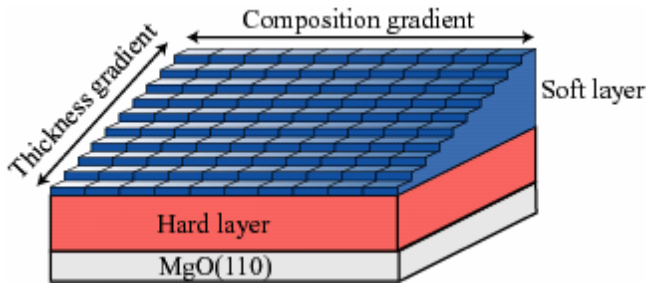

Fig. 3.1 Schematic of the libraries.

3.2.2 Characterization of crystallinity using x-ray diffraction

Crystallinity and the out-of-plane orientation of the epitaxially-grown CoPt and Sm_2Co_7 hard layers were studied by a Bruker D8 x-ray diffractometer (XRD) with an area detector using CuK_α radiation (0.15418 nm). Fig.3.2 shows the θ-2θ x-ray diffraction (XRD) patterns of the (a) CoPt hard layer and (b) Sm_2Co_7 hard layer. In Fig. 3.2 (a), the CoPt(110) peak appears at around 33.3º, the CoPt(220) peak at around 71º. We did not observe any other peaks of the CoPt thin film. In Fig. 3.2 (b), we observed only the $Sm_2Co_7(2\bar{2}00)$ peak at around 41.31º except the peaks from the MgO(110) substrate. Thus a (110) oriented CoPt layer and a $(2\bar{2}00)$ oriented Sm_2Co_7 layer were successfully grown on the MgO(110) substrate. We didn't observe any peaks of the soft layer. We believe this is due to the fact that the grains of the polycrystalline soft layer are too small.

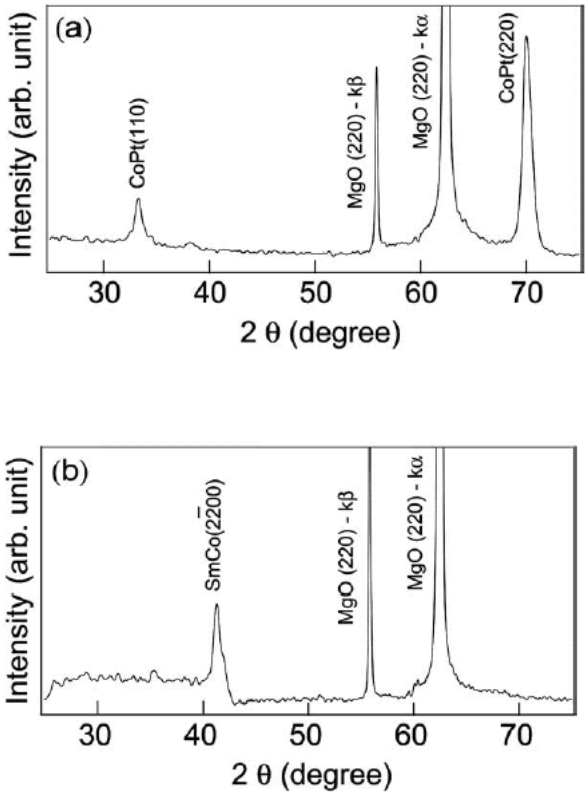

Fig. 3.2 X-ray diffraction (XRD) patterns of (a) CoPt and (b) nominal Sm_2Co_7. XRD using a K_α and K_β Cu source.

3.2.3 *M-H* hysteresis loops

The *M-H* hysteresis loops of each spot were measured using MOKE, which allow us to rapidly scan all the samples on a single library in one measurement session. (See 1.4.3)

3.3 Results and discussion

3.3.1 Exchange length and soft-magnetic parameters

We tracked the hysteresis loop collected using MOKE from each spot within the same sample to study its variation as a function of the soft-layer composition and

thickness. An ideally exchange coupled soft/hard magnet shows a one-phase-like *M-H* hysteresis loop. A partially exchange coupled magnet exhibits a two-phase-like *M-H* hysteresis loop. Within a row of spots on a library with a fixed soft layer composition, a "transition" between the one-phase-like and two-phase-like behaviors[40] appears as t_s increases. We define the composition-dependent thickness of the soft layer at which the first sign of two-phase-like behavior is observed in the plots to be the coupling length (λ_x), where the subscript x denotes the soft layer composition.

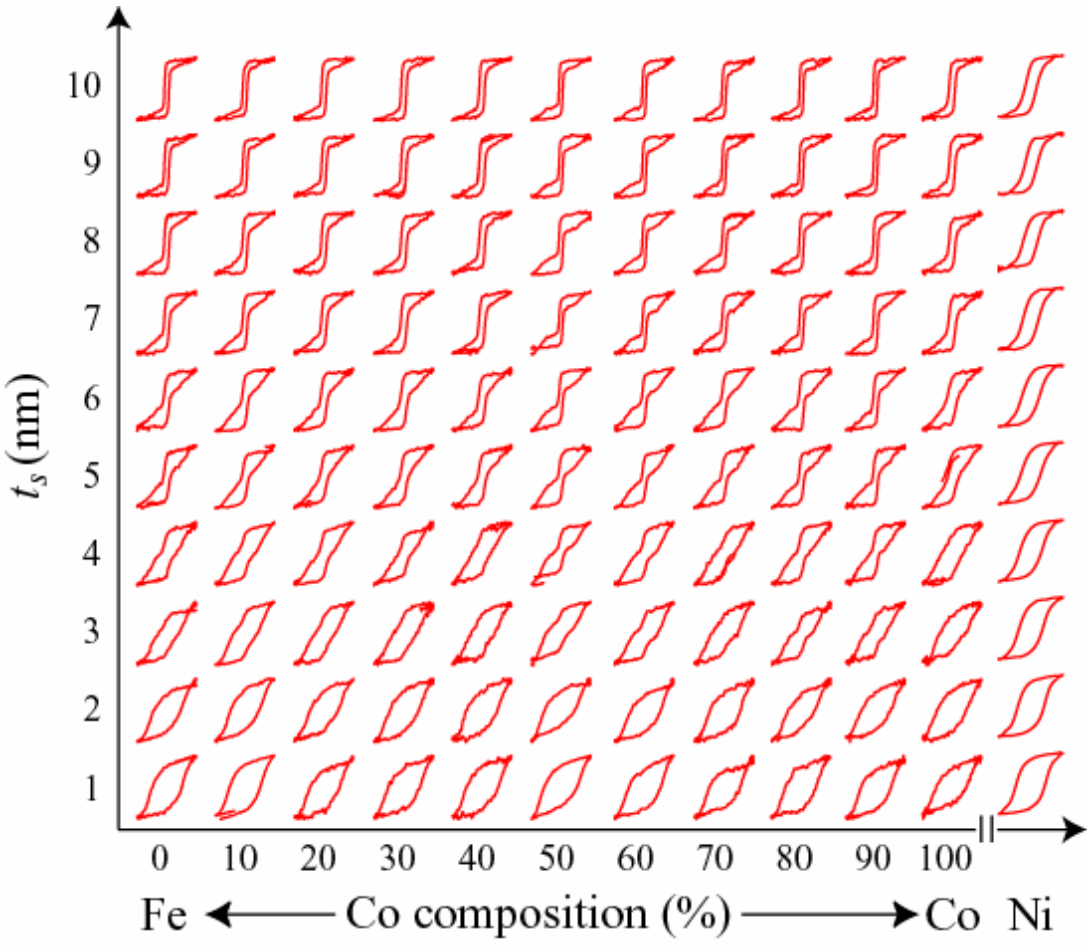

Fig. 3.3 Magnetic hysteresis loops (arb.unit) for different soft layer thicknesses (t_s) and compositions on a CoPt ($H_c \approx 0.64$ T) hard layer measured on a single library. The coupling length λ_x is experimentally determined from the soft layer thickness at which the transition between one-phase-like behavior and two-phase-like behavior takes place.

Fig. 3.3 shows hysteresis loops of Fe-Co and Ni on CoPt with $H_c \approx 0.64$ T. From such sets of loops, visual inspection along with analysis of the first derivative of the loops with respect to the applied field allow us to obtain λ_x for different soft layer compositions. The derivative of the curves shows a clear peak, where there is a

drastic change in the slope in the case of the two-phase-like behavior. The fixed finite increment of the thickness variation on each library creates a lower bound to the total uncertainty of each λ_x measurement to be ± 0.5 nm (i.e., half of the t_s increment). These uncertainties are associated with the difficulty in graphically determining the soft layer thickness at which the two-phase-like behavior first appears. The values of λ_x reflect the trend of the transition vs soft layer composition. The uncertainty of λ_{Ni} was not assigned, due to difficulty in determining the one-to-two-phase-like transition for this soft layer composition. The one-to-two-phase-like transition can occur over as much as a full thickness step. Because of the finite penetration depth of the laser, as t_s is increased, the MOKE signal obtains less information from the hard layer underneath the soft layer. For $t_s \geq 10$ nm, most of the signal comes from the soft layer, and if the soft layer is still strongly coupled to the hard layer, the one-to-two-phase-like transition will not appear within the samples. This was the case in the Ni magnetization loops displayed in Fig. 3.3, and we conclude that $\lambda_{Ni} \geq 10$ nm, however, given the data trend, we do not expect λ_{Ni} to be too much larger than 10 nm. Thus, on CoPt, while we assign λ_{Ni} to be 10 nm, it is understood to be a lower limit value. Figure 3.4 shows hysteresis loops of Fe, Co, and Ni on Sm_2Co_7 with $H_c \approx 0.68$ T. In this case, we consider the total uncertainty of λ_x to be approximately half of the average of the t_s increment, or ± 0.35 nm. The values of λ_x vs composition obtained from Figs. 3.3 and 3.4 are displayed in Fig. 3.5. The data indicate that λ_x is substantially lower for Sm_2Co_7 ($H_c \approx 0.68$ T) than for CoPt ($H_c \approx 0.64$ T) even though these two hard layers have similar coercive field values. This underscores the significance of hard layer properties other than H_c in determining the exchange

interaction. For CoPt ($H_c \approx 0.64$ T), λ_x increases going from pure Fe to pure Co, with Ni yielding the highest value. For Sm_2Co_7 ($H_c \approx 0.68$ T), λ_x is similar for Fe and Co, but Ni has a higher value. This shows the presence of exchange coupling dependence on the soft layer elements: Ni couples more than Co to either hard layer and, in general, these two couple more than Fe.

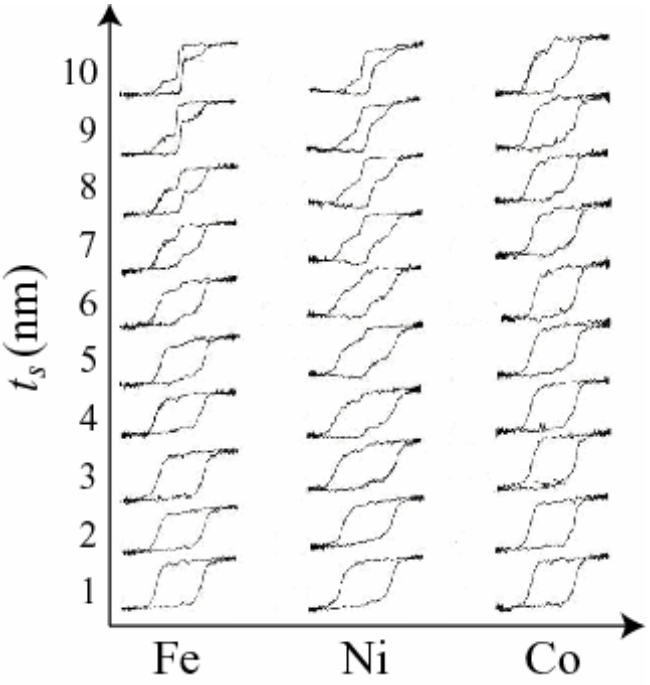

Fig. 3.4 Magnetic hysteresis loops (arb.unit) for different soft layer thicknesses (t_s) for three elemental soft layers on a Sm_2Co_7 hard layer with coercive field ≈ 0.68 T. The data curves are a representative subset of those obtained.

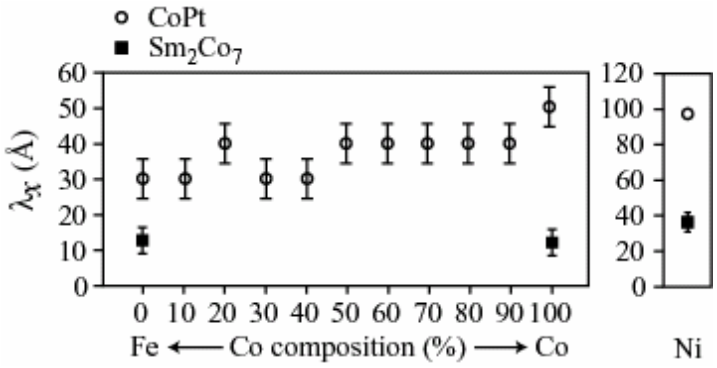

Fig. 3.5 Coupling length (λ_x) as a function of soft layer composition on CoPt (coercive field: $H_c \approx 0.64$ T) and Sm_2Co7 ($H_c \approx 0.68$ T) hard layers. λ_{Ni} value is its lower limit. Composition uncertainties are not included in the graph.

We look at experimentally determined λ_x vs $1/M_s^s$, K^s, and $1/A^s$. s denotes the soft layer. These plots are shown in Fig. 3.6. There appears to be a linear correlation between λ_x vs $1/M_s^s$ (Fig. 3.6(a)), while the correlations are less clear for λ_x vs K^s (Fig. 3.6(b)), and λ_x vs $1/A^s$ (Fig. 3.6(c)).

Apparently, Ni is the material with the longest λ_x. However, $(BH)_{max}$ depends not only on λ_x, but also on M_s^s (Fig. 3.7(a)). In order to find the best composition of the soft magnetic material, we calculated $(BH)_{max}$ of soft/hard(CoPt) magnetic bilayer system using Equation (2.11). In the calculation, the thickness of the soft layer and the hard layer are λ_x of each composition and 30 nm, respectively. Saturation magnetization (M_s) of the soft/hard magnetic bilayer system is defined as

$$M_s = t_s M_s^s + t_h M_s^h$$

where t_s, t_h are volume fraction of the soft layer and the hard layer, respectively. M_s^h is the saturation magnetization of the the hard layer. The calculated $(BH)_{max}$ is plotted as a function of the composition of the soft layer (Fig. 3.7(b)). By changing the

composition of the soft layer, $(BH)_{max}$ becomes maximum with the composition of the soft layer ≈ $Fe_{0.4}Co_{06}$, which corresponds to the composition with maximum saturation magnetization, and decreases with decreasing M_s^s. This is indicating that even though the coupling length increases proportional to the inverse of the M_s^s, naturally, one cannot simply use the material with the smallest M_s. These values are still much lower compared to the maximum attainable $(BH)_{max}$ predicted by theories, but this is mainly due to the fact that the hard layer parameters (namely the thickness) used here are not the optimized ones.

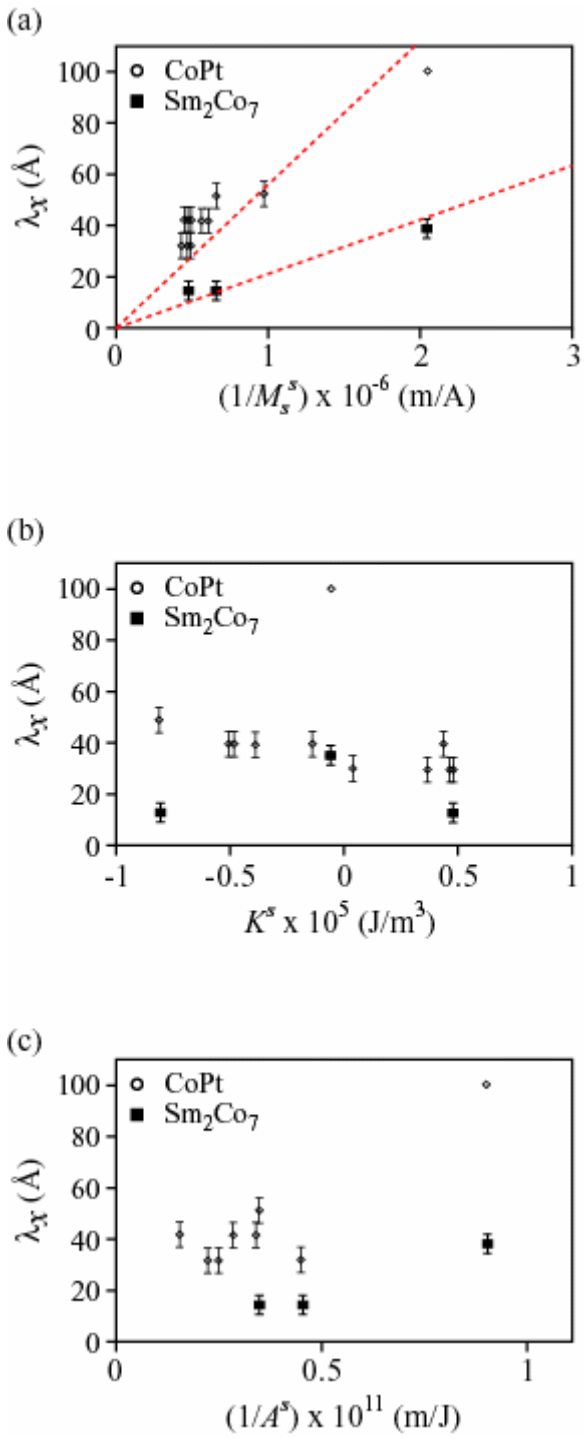

Fig. 3.6 Coupling length λ_x vs (a) $1/M_s^s$ (saturation magnetization), (b) $1/K^s$ (anisotropy constant), and (c) $1/A^s$ (exchange stiffness) of the soft layer for CoPt ($H_c \approx 0.64$ T) and Sm_2Co_7 ($H_c \approx 0.68$ T) hard layers. Dashed line on (a) is a guide to the

eye to show linear correlation between λ_x and $1/M_s^s$. Data are not shown as a function of anisotropy (A^s) for compositions $Fe_{90}Co_{10}$, $Fe_{80}Co_{20}$, $Fe_{40}Co_{60}$, and $Fe_{20}Co_{80}$ due to the absence of anistropy values for these alloys in the literature.

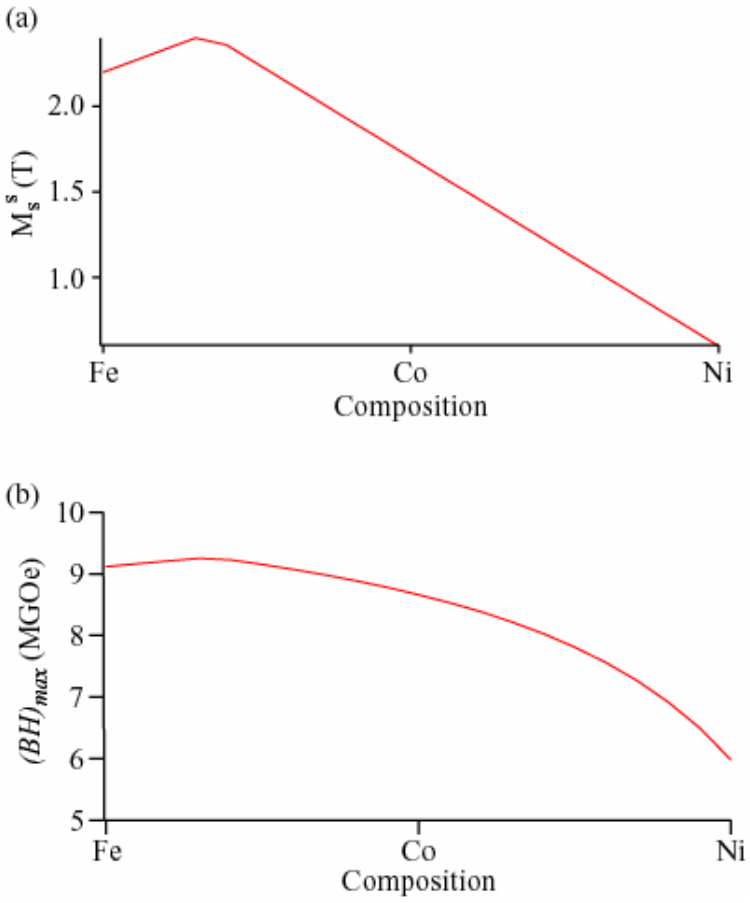

Fig. 3.7 (a) Saturation magnetization of the soft layer (M_s^s) vs composition of the soft layer. (b) Maximum energy product ($(BH)_{max}$) vs composition of the soft layer for a fixed hard layer thickess of 30 nm (CoPt).

3.3.2 Nucleation field and hard-magnetic parameters

We also observed a dependence of λ_x on the hard layer coercive field. Fig. 3.7(a) shows the hysteresis loops of Fe/CoPt samples for two different coercive field

values of CoPt. From these loops, we determined that $\lambda_{Fe} \approx 3$ nm and $\lambda_{Fe} \approx 2$ nm for $H_c \approx 0.64$ T and $H_c \approx 1$ T, respectively. This represents a reduction of ≈ 30 % in λ_{Fe} for ≈ 56 % increase in H_c. Similarly, Fig. 3.7(b) shows the hysteresis loops of Ni/Sm_2Co_7 for two different H_c of Sm_2Co_7. From these loops, we determined that λ_{Ni} ≈ 3.7 nm and $\lambda_{Ni} \approx 1.5$ nm for $H_c \approx 0.68$ T and $H_c \approx 1.32$ T, respectively. This represents a reduction of ≈ 60 % in λ_{Ni} for ≈ 100 % increase in H_c. If the other hard layer properties did, in fact, not change, these results would indicate that increasing the hard-layer coercive field decreases the coupling length.

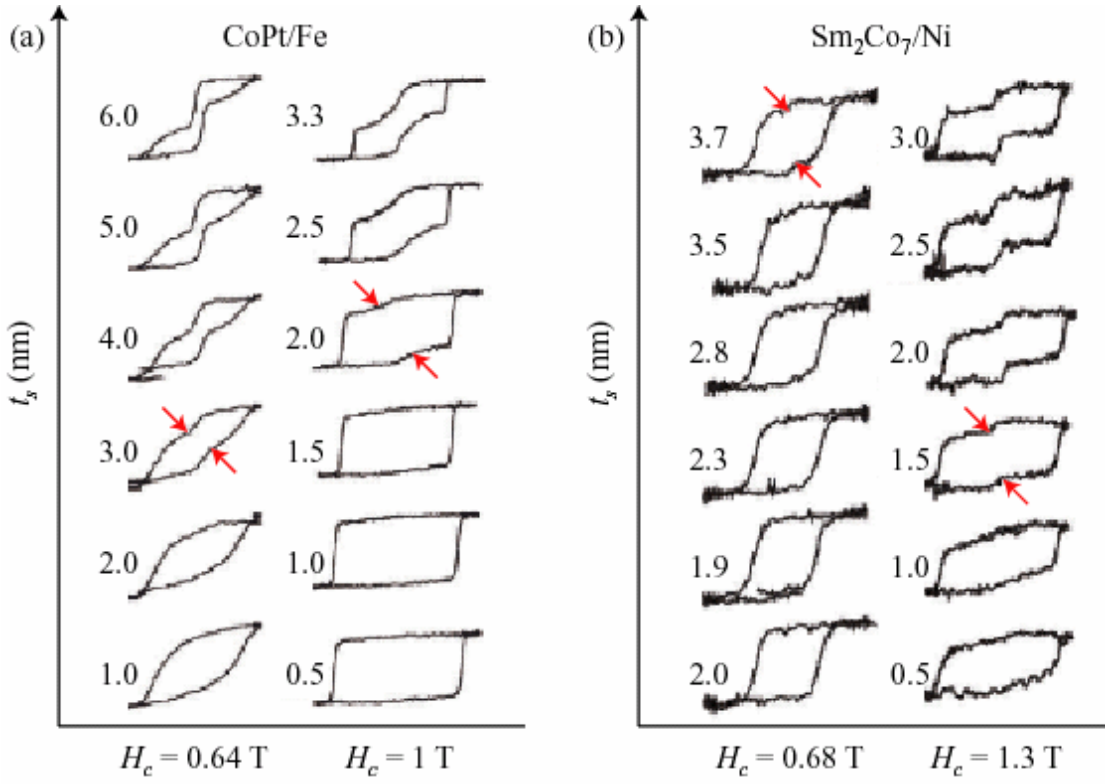

Fig. 3.8 Magnetic hysteresis loops (arb.unit) for a range of soft layer thicknesses t_s on (a) CoPt and (b) Sm_2Co_7 hard layers possessing two different coercive fields (H_c).

The arrows indicate the locations on the hysteresis loops where two-phase-like behavior is first observed with increasing t_s.

In Figs. 3.3 and 3.4 one can clearly discern a continuous shape change of the hysteresis loops together with a change of the coercive field along the y axis. We graphically determine the nucleation field H_N for each hysteresis loop to be the field at which the slope of the curve during the demagnetization process starts to change substantially. This value is equated to the value of H, where the tangent to the loop at the point with maximum magnetization intercepts the tangent to the loop at the point of minimum slope (see Fig. 3.8 inset, points marked "A"). As seen in Fig.3.3 and 3.4, the nucleation field thus determined shifts substantially when the behavior transitions from one-phase-like to two-phase-like in addition to the significant systematic variation across the full range of t_s values.

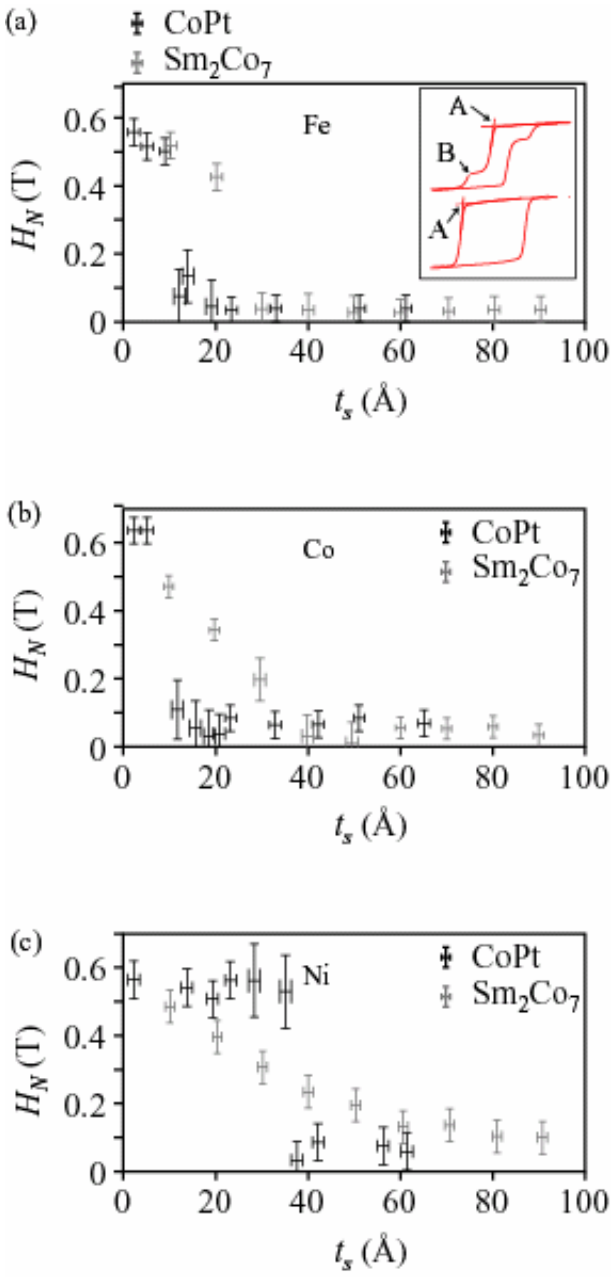

Fig. 3.9 The nucleation field (H_N) as a function of the soft layer thickness t_s for soft layers (a) Fe, (b) Co, and (c) Ni. The symbols are experimental data. Results are shown for both Sm_2Co_7 ($H_c \approx 0.68$ T) and CoPt ($H_c \approx 0.64$ T) hard layers. Inset: graphical determination of H_N, marked A, and the ideal irreversible field H_{irr}, marked B.

3.3.3 Numerical calculation of the irreversible field

Figure 3.8 displays the experimental values of H_N vs t_s, for Fe, Co, and Ni on Sm_2Co_7 ($H_c \approx 0.68$ T) and CoPt ($H_c \approx 0.64$ T). The data follow the same general trend, with H_N decreasing from approximately H_c toward an asymptotic minimum value as t_s increases from 0. The thickness range where H_N decreases most rapidly corresponds to the appearance of the two-phase-like behavior in the magnetization loops. One might expect that the nucleation field decreases most rapidly when the soft layer thickness t_s approximately equals the coupling length λ_x. The behavior depends on both the hard layer and the soft layer. Broadly speaking, the nucleation fields are higher with the CoPt hard layer than the Sm_2Co_7 hard layer for a given thickness of soft Fe, Ni, or Co, the exception being thin Ni. Also, the nucleation field H_N decreases more smoothly with increasing thickness of the Co and Ni soft layers for the CoPt hard layer versus the Sm_2Co_7 hard layer. The results, along with the behavior observed for λ_x, indicate that soft layers with lower saturation magnetization are exchange-coupled more to a given hard layer, while the exchange coupling interaction is impacted by the hard layer characteristics as one might expect.

To obtain more insight about the effect of the micromagnetic constants on the exchange coupling, we utilized the model of Leineweber and Kronmüller.[45] This model gives the irreversibility field (H_{irr}), which ideally corresponds to the field at point *B* in the inset of Fig. 3.8 (a), as a function of t_s. From H_{irr} vs t_s for the different material systems, we can obtain the dependence of the coupling length λ_x on the magnetic constants. In the following, superscripts *h* and *s* on the magnetic constants explicit the hard layer and the soft layer, respectively. To find the general

trend in the H_{irr} vs t_s curve with independently changed magnetic constants, we analyzed a particular Fe/SmCo bilayer (Fig. 3.9). In the model, the Gibbs free energy of the system is minimized, and the resulting Euler-Lagrange equations are solved to obtain the rotation of the in-plane polarization $\theta(x, H, t_s)$ as a function of the position x. Using the model and following the same stability analysis technique described in Refs. 45 and 55, H_{irr} vs t_s was numerically calculated for t_s over the full range from 0 to 10 nm. Below the thickness $t_s = t_o$, H_{irr} was considered to be equal to the ideal irreversible field of the hard layer.[45,56] The model assumes that for $t < t_o$, the coupling between the soft/hard layers is maximized, which in an ideal case represents complete coupling. Thus, t_o is equivalent to our experimentally obtained λ_x values. The magnetic constants used for these calculations are shown in the caption of Fig. 3.9.

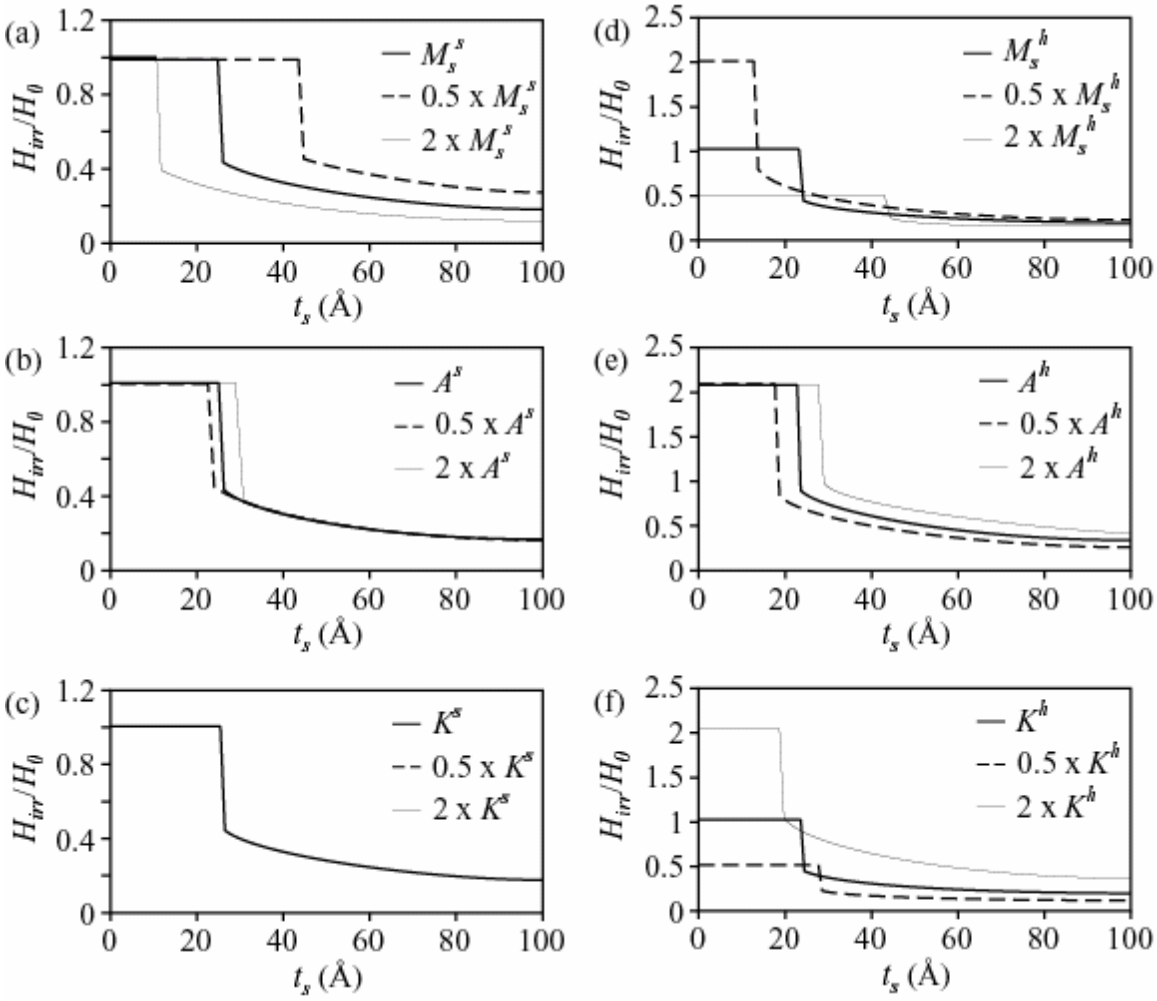

Fig. 3.10 Numerical calculations of the irreversible field (H_{irr}) of SmCo / Fe(t_s) as functions of the soft layer thickness t_s obtained from the model by Leineweber and co-workers (Refs. 2 and 22). λ_x is the coupling length and $H_o = 2K^h / M^h$. Magnetic constants used are $K^s \approx 0.48 \times 10^5$ J/m^3, $M_s^s \approx 1.7 \times 10^6$ A/m, $A^s \approx 2.7 \times 10^{-11}$ J/m, $K^h \approx 5 \times 10^6$ J/m^3, $M^h \approx 5.5 \times 10^5$ A/m, and $A^h \approx 1.2 \times 10^{-11}$ J/m.

The overall trends predicted by the model for variation of the properties of the soft magnetic material are as follows: λ_x increases with decreasing M_s^s, while it is barely affected by changes in A^s and not affected by changes in K^s in the range of

values used, which roughly correspond to those of the soft material studied here. For variation of the hard magnetic material properties, it is found that λ_x increases as M_s^h or A^h increases and decreases as K^h increases. The dependence of λ_x, obtained from the model of Leineweber and co-workers, on independently changed soft layer magnetic constants agrees with the experimental observations. This indicates that the soft materials that most effectively increase the coupling length are those with lower M_s.

The experimental results when the hard layer is changed are also interpreted using the calculation results. The magnetic constants of bulk hard materials [CoPt and Sm_2Co_7] are such that $K_{CoPt} \leq K_{SmCo}$, $M_{CoPt} \geq M_{SmCo}$, and $A_{CoPt} \geq A_{SmCo}$. If the magnetic characteristics of the thin-film hard layers are similar to those of bulk materials, the model by Leineweber and Kronmüller indicates that $\lambda_{x\text{-CoPt}} \geq \lambda_{x\text{-SmCo}}$ would be expected for a soft-hard stack with a generally soft material x. This is consistent with what is experimentally observed. Specifically, for M_s^h and A^h unchanged, higher H_c corresponds to higher K^h and thus prediction of a reduced λ_x in agreement with the decrease of the experimental λ_x with increasing coercive field observed experimentally in Fig. 3.7.

3.4 Conclusions

In conclusion, the high-throughput soft/hard magnetic layer experiments show a trend indicating that the hard layer magnetic parameters and the saturation magnetization of the soft layer play the most important roles in determining the nucleation field and the coupling length. Hard materials with higher coercive field do

not necessarily always benefit the soft/hard phase interaction. There is an inverse relation between the width of the domain wall of the hard layer and the exchange coupling interaction. In the range of exchange stiffness K and anisotropy constant A values used in this experiments, the saturation magnetization M_s is the principal parameter of the soft layer that governs the exchange interaction: the higher the M_s, the stronger the exchange interaction. A tradeoff between coercive field and exchange interaction is observed: hard phases with higher coercive field do not necessarily result in an enhancement of energy product. Similarly, because of the trade-off between saturation magnetization and exchange length, soft materials with the longer coupling length do not always result in an enhancement of the energy product.

Chapter 4: Effect of grain-mixture of hard layer on exchange coupling

4.1 Introduction

Most theoretical studies are based on the assumption that the hard phase is composed of one type of crystallized grain with a crystallograpycally oriented uniaxial easy axis. In the real hard phases, however, we can find various crystallinities and grain-texturings which result in easy axes pointing in various directions. Thus the effect of the crystallinity and the grain-texturing on the exchange coupling should be studied carefully.

In our experiment, the crystallinity of the hard layer is controlled by the deposition temperature and the post-annealing process. Alignment of the easy axis of the CoPt hard layer is controlled by epitaxial growth on MgO (110) substrate. The thickness of the Fe soft layer of Fe/CoPt soft/hard bilayer library is continuously changed on the CoPt hard layer to systematically delineate subtle changes in the exchange coupling behavior.

4.2 Experiment

4.2.1 Fabrication of Fe/CoPt soft/hard magnetic combinatorial bilayers

Fe was used as the soft layer which has a large saturation magnetization and low H_c, and CoPt was used as the hard layer which has a high H_c and low saturation magnetization. Fe/CoPt soft/hard magnetic bilyer thin films were deposited in a high-

vacuum combinatorial electron-beam (e-beam) deposition chamber (with the base pressure ≈ 3 x 10^{-8} Torr). The chamber has two e-beam guns with two movable copper crucibles, each of which contains 6 pockets for metal targets, and two computer-controlled movable shadow masks. This allows us to deposit up to 36 different combinations of metallic layers without breaking the vacuum on 1.5 cm x 1.5 cm substrate. By synchronizing the motion of the shadow masks with the evaporation rates of the targets, we can fabricate thin films in precisely controlled areas, with controlled compositions, and a gradient thickness in two perpendicular directions. The advantage of this technique is that we can grow multiple samples on an individual chip under the same set of conditions, which reduce subtle run-to-run variations in the conditions, and we can perform systematic and high-throughput studies. In this experiment, simple bilayer samples with gradient thickness in one direction were fabricated.

Fig. 4.1 shows the schematic of a typical design of the Fe/CoPt soft/hard bilayer gradient sample. The top Fe layer has a gradient thickness. In this work, we studied three gradient Samples, A, B, and C, whose differences are in their CoPt crystallinity. CoPt films were grown epitaxially on MgO (110) substrates, after deposition of a 1 nm-thick Pt buffer layer at 500 ºC (not shown). Then a 30 nm-thick CoPt hard layer was deposited at 450 ºC on Sample A and at 500 ºC on Samples B and C. Sample C was then annealed at 500 ºC for 15 minutes in vacuum, while Sample B was not. All three samples were cooled down to room temperature before the deposition of the Fe soft layer. The Fe soft layer was deposited with a thickness gradient from 0 to approximately 10 nm over 10 mm, which is the length of each

sample chip. To prevent oxidization, the gradient samples were capped with a 5 - 8 nm-thick Au layer (not shown). The continuous Fe thickness (t_{Fe}) gradient allows us to systematically determine the critical Fe thickness to obtain an ideal hard-soft layer exchange coupling. In Chapter 3, we have used this technique to delineate the dependence of the exchange length on the soft magnetic parameters.[53]

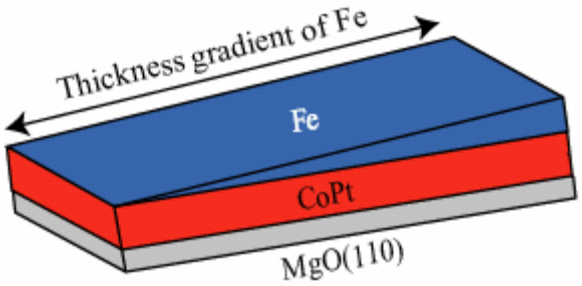

Fig. 4.1 Schematic of a typical sample design.

4.2.2 Two possible types of orientations of epitaxially grown CoPt hard layer

Given the lattice match between the MgO substrate and the CoPt hard layer, two different types of CoPt $L1_0$ structure orientations can be epitaxially grown on MgO (110): one with its *c*-axis inclined at ~ 45° with respect to the substrate plane (type-I orientation) and another with its *c*-axis in the substrate plane (type-II orientation).[57,58] Fig. 4.2(a) and 4.2(b) show the typical crystal structures of fcc MgO and fct CoPt, respectively. In Fig. 4.2(c), the MgO (110) plane is rotated 45 ° along the c-axis of the MgO substrate so as to facilitate the visualization of the film growth configuration in the MgO [110] direction. This also helps to visualize, in the actual system, the magnetic easy axis (*c*-axis) of the type-I orientation, whose in-

substrate-plane projection is parallel to MgO [1 $\bar{1}$ 0] and that of the type-II orientation, which is parallel to MgO [001].

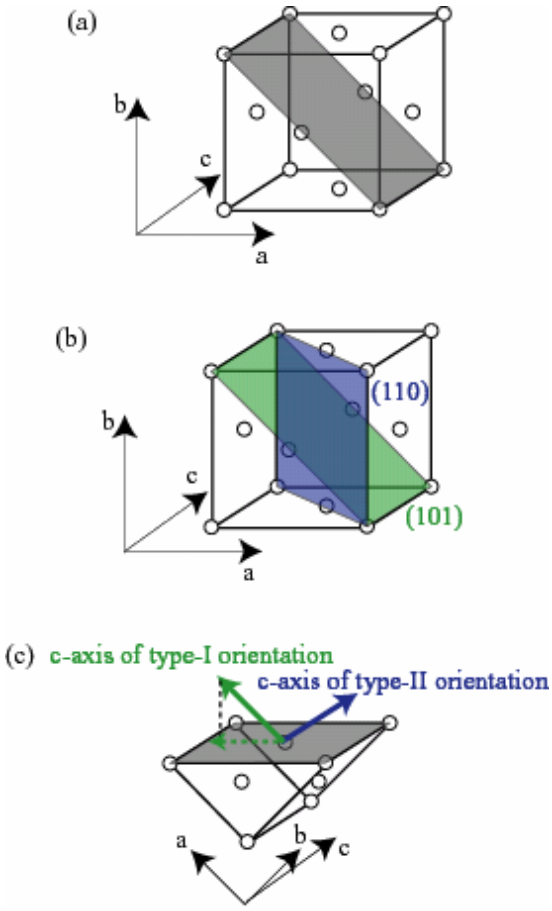

Fig. 4.2 Typical crystal structures of (a) fcc MgO and (b) fct CoPt. (c) The MgO (110) plane is rotated 45 ° along c-axis of MgO. Green and blue arrows are easy axes (c-axis) of the type-I orientation and the type-II orientation.

4.3 Results and discussion

4.3.1 Crystallinity of CoPt hard layer

Fig. 4.3 shows the θ-2θ x-ray diffraction (XRD) patterns of the CoPt hard layer in the three samples. Patterns of Samples A, B, and C are indicated by colors red, blue

and green, respectively. At around 33.3º, Sample B and Sample C show the CoPt (110) peak with a higher intensity than the same peak in Sample A. The CoPt (110) peak comes from the type-II orientation only. This clearly shows the difference in the CoPt structure in each sample, indicating that Sample B and Sample C have a larger amount of type-II grains than Sample A does. At around 71º, a high-intensity broad peak is observed for all three samples. This is the overlapping of the CoPt (220) peak, which is associated with grains with the type-II orientation, and the CoPt (202) peak, which is associated with grains with the type-I orientation. Inset shows the peak at around 71º more clearly. The change in the peak shape and their peak position shift is attributed to changes in the structure and the relative volume fraction in the mixture of grains with the two orientations.

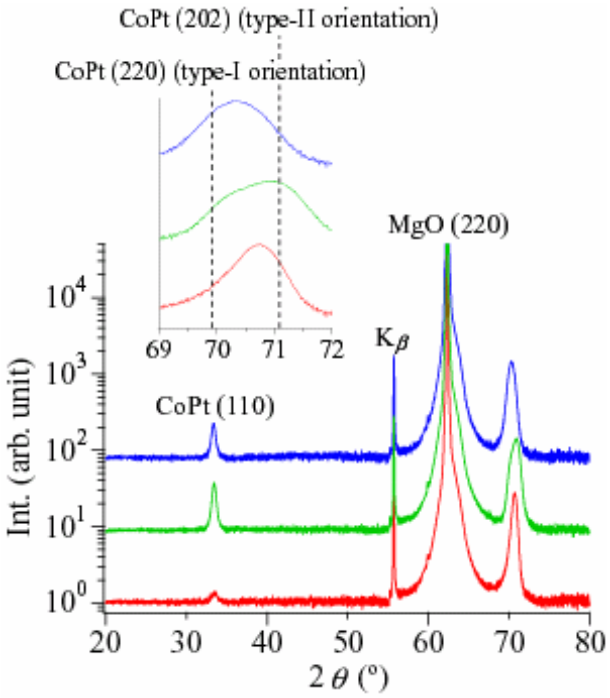

Fig, 4.3 XRD patterns of Samples A (red), B (green), and C (blue). Inset: magnification of the mixed peak region.

4.3.2 In-plane orientation of epitaxially grown CoPt hard layer

A pole figure XRD analysis was performed to investigate the in-plane epitaxial relationship between the MgO substrate and the CoPt thin film (Fig. 4.4). The CoPt (201) planes of the type-I orientation and type-II orientaition, and the MgO (200) plane were observed at χ angles of 16.3º, 49.8º, and 43.5º, respectively. A two-fold symmetry is seen for MgO (200) (gray spots) at the same φ angles for CoPt (201) of the type-I orientation (green spots). CoPt (201) of the type-II orientation (blue spots) appears symmetrically on either side of the MgO (200) peaks. The φ angle between the type-I and type-II of CoPt (201) planes is ≈ 36.7º as measured from the pole figure. This value agrees well with the expected interplaner angle of 36.0º, which can be estimated using the literature values of the lattice parameters, namely, a = 0.380300 nm and c = 0.370100 nm (JCPDF 43-1358). Because the type-I and the type-II reflections are observed as well-defined peaks rather than a ring at the expected φ angle, an epitaxial relationship between the MgO (110) substrate and the CoPt thin film is confirmed.

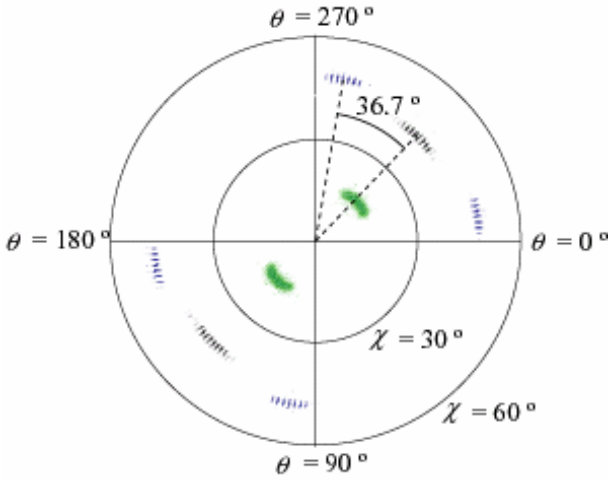

Fig. 4.4 Pole figure of the CoPt (201) of the type-I orientation (green) and the type-II orientation (blue) on the MgO (110) substrate, together with the MgO (200) (gray).

4.3.3 Volume fraction of grains

To estimate the volume fraction of each type of orientation, we looked at θ-2θ XRD scans. The idea is to find a set of planes that allows us to see peaks coming from the two types of grain orientations separately: the same indexed peak would appear separately in the reciprocal space coming from different grain orientations and located at different φ values. As shown in Fig. 4.5, for each sample, we have used the CoPt (201) peaks for the two grain orientations. The volume fraction V for each orientation, *I* or *II*, was calculated as:

$$V_{I,II} = \frac{\text{Peak Area}_{I,II}}{(\text{PeakArea}_{I}) + (\text{Peak Area}_{II})}$$

Here, peak area is the integrated peak area in the spectrum. The peak intensity of the CoPt (201) coming from the type-II orientation is very weak for Sample A It is slightly stronger for Sample B, and well pronounced for Sample C (See Fig. 4.5(a),

4.5(b), and 4.5(c) for Samples A, B, and C, respectively). This results in a decrease of V_I and an increase of V_{II} as seen in Tab. 4.1 This indicates that the CoPt hard layer goes from mostly consisting of type-I grains in Sample A to being a more balanced mixture in Sample C.

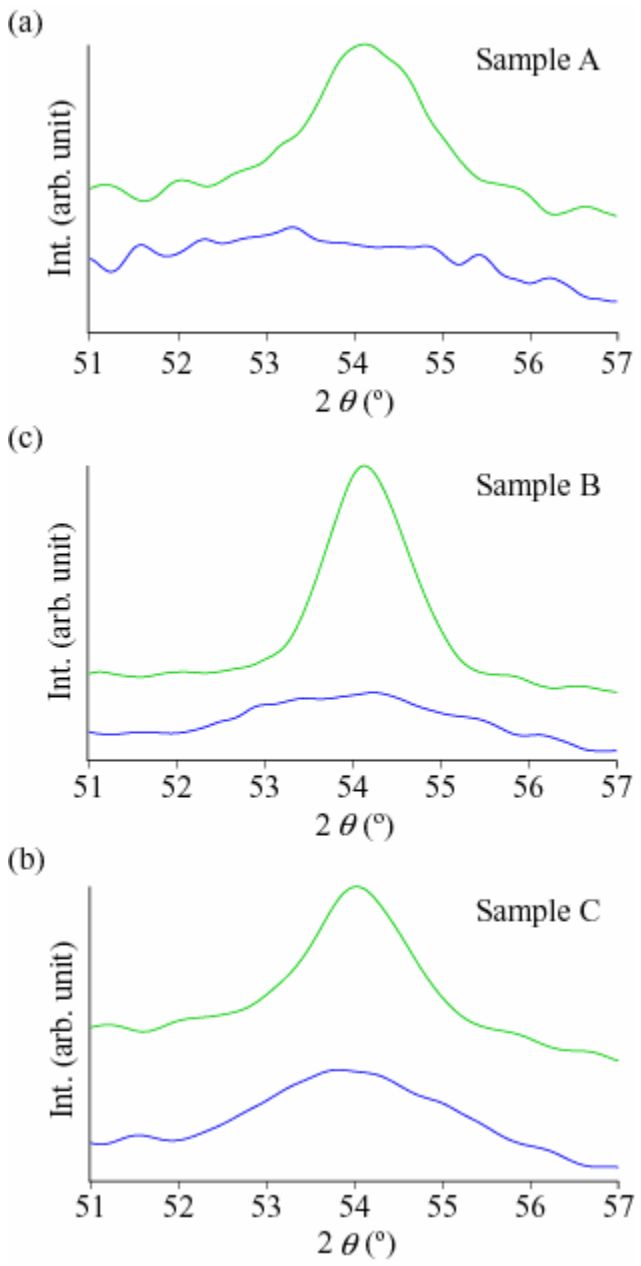

Fig. 4.5 θ-2θ XRD patterns of the CoPt (201) peaks of the type-I orientation and the type-II orientation for each sample.

	Sample A	*Sample B*	*Sample C*
V_I	≈ 1	0.84	0.54
$\mathbf{V_{II}}$	≈ 0	0.16	0.45

Tab. 4.1 Volume fraction of the type-I orientation grains (V_I) and the type-II orientation grains (V_{II}) in each sample.

4.3.4 Direct observation of microstructure of the CoPt hard layer

Fig. 4.6 shows typical TEM cross sectional images taken along [001] of the MgO substrate. The images are from Sample B, but the main features seen in the images are representative of all three samples. The dark field image in Fig. 4.6(a) shows a Fe/CoPt system with a low interface roughness. This reduces uncertainties coming from the orange peel effect and simplifies the one-dimensional analysis. In Fig. 4.6(b), a high-resolution image shows the MgO (200) and MgO (020) lattice planes, as well as the CoPt (002) and/or the CoPt (200) lattice plane of the type-I and/or type-II grains, respectively. The spacing of the CoPt (002) planes in type-I grains and the CoPt (200) planes in type-II grains are 0.1848 nm and 0.1908 nm, respectively. This similarity in value makes it difficult to distinguish the orientations by simply studying the images. There is a clear MgO/CoPt interface, and there is no sign of discontinuity of the lattice planes. This confirms the epitaxial growth of the CoPt hard layer.

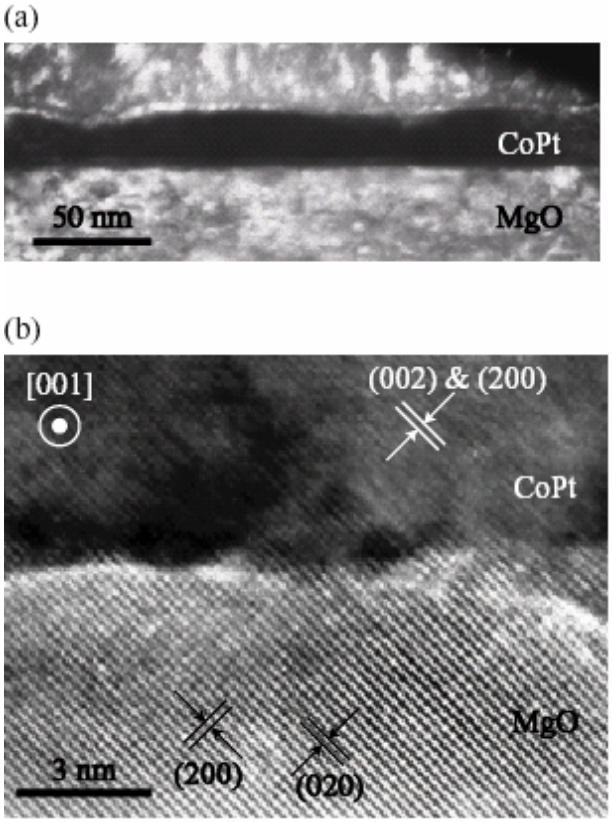

Fig. 4.6 (a) A cross-sectional dark field image and (b) cross-sectional high-resolution image of Sample B.

4.3.5 Magnetic easy axis of grain-textured CoPt hard layer

The two CoPt grain orientations have different magnetic easy axes relative to the substrate, whose combination leads to the effective easy axis of each sample. Our CoPt hard layers have larger fractions of the type-I orientation grain than the type-II orientation grain fraction (see Tab. 1). To empirically determine the effective easy axis, we measured the *M-H* loops for external field applied along two MgO directions: $[1\,\bar{1}\,0]$ and [001] (see Fig. 4.7). The type-I orientation has a substrate in-plane projection parallel to MgO $[1\,\bar{1}\,0]$, and that of the type-II orientation is parallel to MgO [001]. The *M-H* loop obtained with the applied external field along the [001]

direction has a smaller H_c and increasing magnetization even after the loop is closed, indicating that this direction is the hard axis. On the other hand, the *M-H* loop obtained with the applied external field along the $[1\,\bar{1}\,0]$ direction has a larger H_c and saturated magnetization when the loop is closed, indicating that this direction is the easy axis. All *M-H* loops shown in the rest of this were obtained by applying the magnetic field along the $[1\,\bar{1}\,0]$ direction of the MgO substrate.

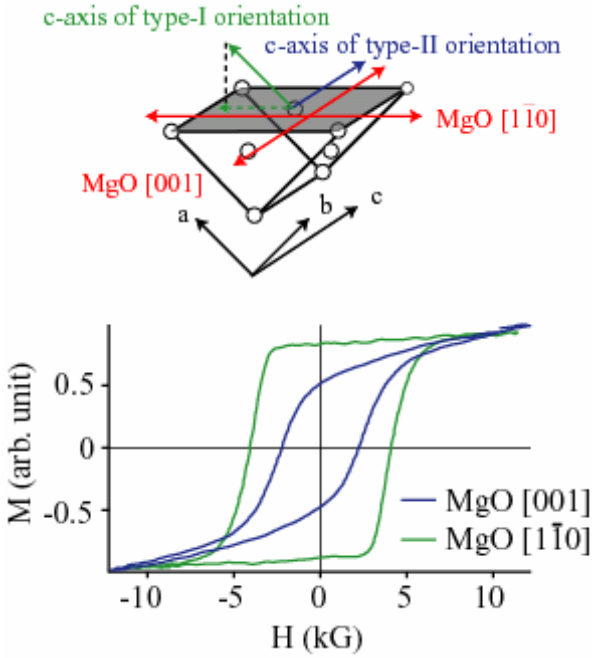

Fig. 4.7 Normalized *M-H* hysteresis loops measured with applied field along the MgO [001] (blue) and the MgO $[1\,\bar{1}\,0]$ (green). Inset: easy axis of the type-I orientation grains (green) and the type-II orientation grains (blue)

4.3.6 Effect of grain-texturing on exchange coupling

An ideally exchange-coupled hard/soft magnet shows a one-phase-like square *M-H* loop. We use this as a qualitative measure of good coupling interaction.

In contrast, a non-ideal exchange-coupled magnet exhibits a non-square one-phase-like or two-phase-like *M-H* loop with a step and/or deflection in the shape of the loop. We use occurrence of such features as indication of non-ideal coupling interaction (even if the system has a high coercive field). This could be due to non-uniform coupling interaction, where the local strength of the coupling behavior might depend on the structure of the hard layer.

To study the exchange coupling behavior in each sample, *M-H* loops of samples with different Fe thickness t_{Fe} were obtained and plotted together in Fig. 4.8(a), 4.8(b), and 4.8(c) for Samples A, B, and C, respectively. Because the penetration depth of the laser beam used in our MOKE system is ≈ 10 nm, in general, the thinner t_{Fe} is, the weaker the magnetic contribution of the Fe soft layer to the shape of the *M-H* loops is. For very thin layer of Fe t_{Fe} ≈ 1 nm, most of the signal in the MOKE measurement comes from the hard layer. The *M-H* loops from the thinnest Fe layer (t_{Fe} ≈1 nm) region gives information about magnetic behavior of the CoPt hard layer. Fig. 4.8 shows variation of the coercive field of the CoPt hard layer of each sample. The coercive field of the CoPt layer is 5 kG, 11 kG, and 13 kG for Samples A, B, and C, respectively. This increase in the coercive field of the CoPt layer is directly correlated with increase in V_{II} and increase in the mixture of two types of orientations (Tab.1). The increase in V_{II} and the mixture of the two orientations also enhances the two-phase-like behavior of the CoPt layer (see Fig. 4.8). Namely, an extra small first step seen in the magnetization curves during magnetic reversal gets more pronounced as the grain orientation mixture increases. As seen in Fig. 4.8, Sample A shows a one-phase-like CoPt *M-H* loop behavior, but Sample C

shows a clear two-phase-like CoPt *M-H* loop behavior.

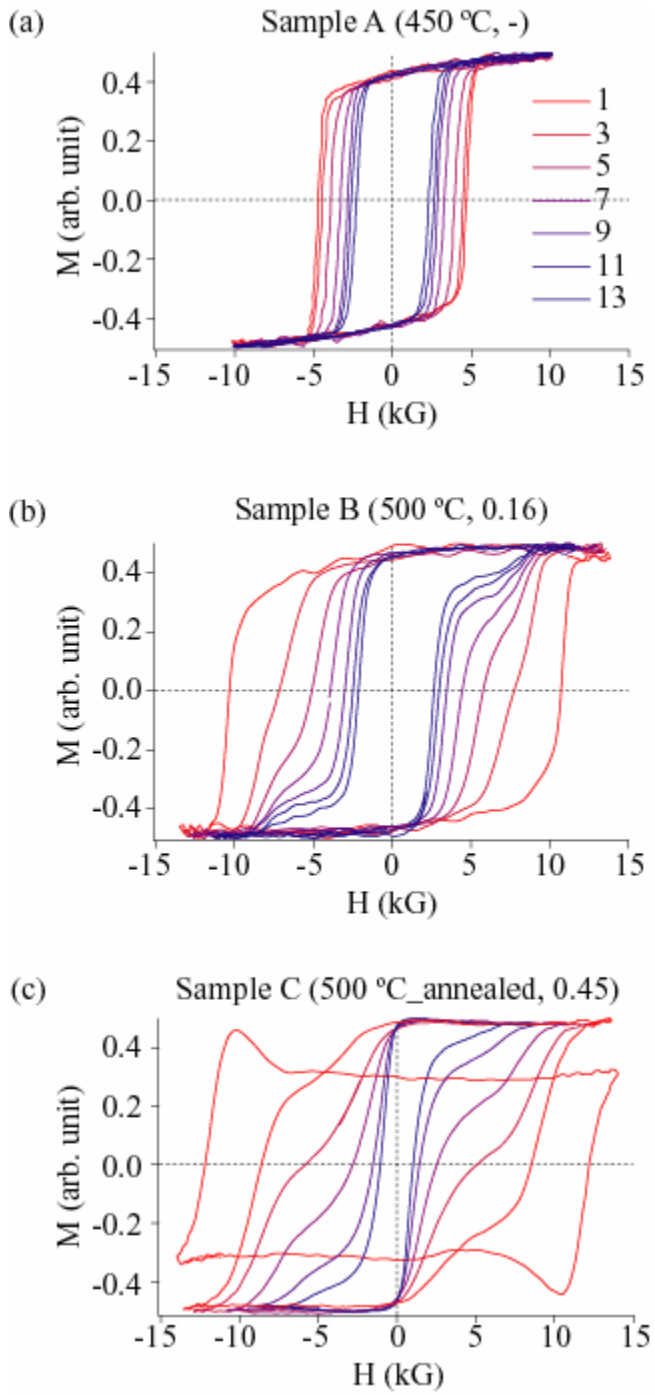

Fig. 4.8 Normalized *M-H* hysteresis loops of various Fe soft layer thickness t_{Fe} on the CoPt hard layer. The thickness of the Fe soft layer t_{Fe} (nm) is indicated by color legend added on (a). In parenthesis: Growth condition of the CoPt hard layer and volume fraction of the type-II orientation grains.

As t_{Fe} increases, all three samples show decrease in their coercive field attributed to the softening of the CoPt hard layer. To further understand the magnetic behavior of the entire system, we define two quantities. H_{c_small}, which is the smaller applied external field at which first maximum slope of the *M-H* loops appears, and H_{c_large}, which is the largest applied external field at which second maximum slope of the *M-H* loops appears (see Fig. 4.8). Because of the increasing degree of demagnetization as a function of increasing t_{Fe}, it is evident that the first demagnetization region of the two-phase-like *M-H* loops corresponds to the Fe contribution to the total magnetization and that H_{c_small} represents the coercive field of the Fe soft layer. Thus, monitoring the position of the H_{c_small} provides a means to characterize the behavior of the soft layer. H_{c_large} is associated with the behavior of the CoPt hard phase.

Fig. 4.9 shows H_{c_small} and H_{c_large} vs. t_{Fe} for each sample. In general, H_{c_large} decreases with increasing t_{Fe} due to the softening of the CoPt hard layer. This variation is more pronounced in Sample B and Sample C, whose CoPt hard layers are mixture of grains with the two types of orientations. Sample A has $H_{c\_small} = H_{c\_large}$, which is a sign of strong coupling interaction. This sample has only one grain orientation. As already mentioned, an increase in the mixture of the two CoPt orientations is also correlated with the appearance of the two-phase-like behavior in Samples B and C. In Sample B, despite showing a decrease in H_{c_small} with increasing t_{Fe} , H_{c_small} values are high and changece considerably as t_{Fe} increases. These are signs of a relatively weak coupling. For Sample C, H_{c_small}s do not decrease with

increasing t_{Fe}. The Fe layer seems to have a non-uniform interaction and follows the behavior of the part of the CoPt layer associated with the first demagnetization only. In addition, H_{c_small} values are the lowest. These observations indicate that Sample C has the weakest coupling among the three samples. It is clear that the overall exchange coupling behavior of a system strongly depends on the CoPt structure, and in particular, on the degree of mixture of its grain orientations.

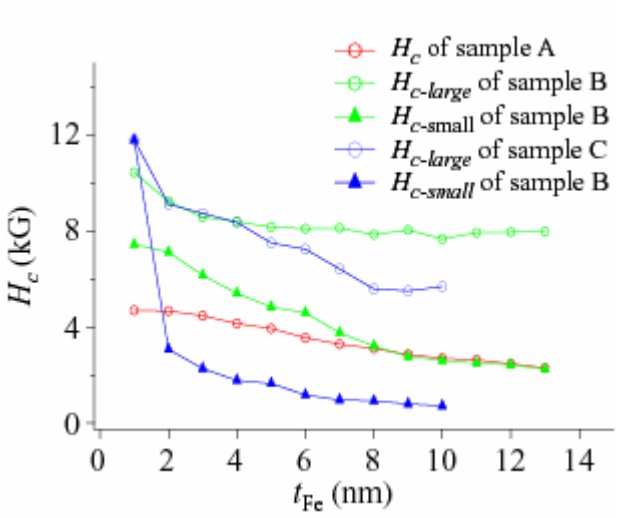

Fig. 4.9 Coercive field of the first and second demagnetization of the magnetization loops (Fig. 4.8) as a function of thickness of the Fe soft layer t_{Fe}. Samples A (red), B (green), and C (blue).

4.4 Conclusions

In summary, Fe/CoPt soft/hard magnetic bilayers were grown on MgO (110) substrates. Epitaxial growth of CoPt hard layers studied in this work consisted of two directional $L1_0$ orientations; type-I (101), with its easy axis along MgO [100] and type-II (110), with its easy axis along MgO [001]. The volume fraction of each grain

orientation was varied by changing the deposition temperature and the heat treatment after the hard layer deposition. An increase in the squareness of the CoPt hard layer magnetic loop is observed when only type-I orientation grains are present. The presence of the single phase grain orientation resulted in the strongest coupling between the CoPt hard layer and the Fe soft layer giving rise to the one-phase-like magnetization loops. When the fraction of the type-II orientation grain (or equivalently the mixture of grain orientations) is increased, magnetization loops of the CoPt hard layer exhibit a two-phase-like behavior. The latter is accentuated when the Fe layer is present, indicating that interlayer coupling is non-uniform. The coupling behavior might depend on the local coercive field of the hard layer. Thus, suppressing the mixture of the two types of grain orientations is beneficial to the enhancement of ideal exchange coupling interaction. In order to increase the maximum energy product $(BH)_{max}$, it is crucial to have one-phase-like magnetic loops with high coercive fields. Therefore, one should not only focus on increasing the coercive field of the hard phase but also on monitoring the squareness of its magnetization loop. One can attain this by tuning the crystalline characteristics of the hard phase to maximize the coupling efficiency.

Chapter 5: Effect of interface roughness and grain-size of hard layer on exchange coupling

5.1 Introduction

Because of the way the exchange-coupled magnets are synthesized, e.g. mechanical alloying, melt spinning etc., they are typically three-dimensional (3d) structures. In constructing such systems, one important goal is to reduce the antiferromagnetic (*AFM*) coupling induced by the dipolar interaction between the soft and the hard phase. When the dipolar interaction is negligible, nanocomposite can be considered ideal exchanged-coupled magnets, where there is only ferromagnetic (*FM*) interaction between the soft and hard phase.[59,53]

C. Rong *et al.* have used 3d micromagnetic simulations to show that the dipolar interaction can play an important role during the demagnetization process, but they also showed that it can be adjusted by controlling the grain size of the constituent phases.[60]

In order to study the effect of dipolar interaction between the soft and the hard phase on the exchange coupling systematically, we used CoPt/Cu/Fe hard-magnetic/non-magnetic/soft-magnetic trilayers with continuously varied Cu layer thickness.

We use the nucleation field (H_N) from magnetic thin film trilayer systems to probe the nature of the inter-phase interaction, the effect of non-magnetic interface impurities on soft-hard phase coupling, and the role played by the soft-hard dipolar interaction in one dimensional (1d) systems. We created wedge samples by inserting

a non-magnetic layer with a varying thickness between soft and hard magnetic thin film layers. We use the term "spot" to denote each small region of one substrate in which the thicknesses of the non-magnetic layer is approximately constant.

5.2 Experiment

5.2.1 Fabrication of Fe/Cu/CoPt soft/non/hard magnetic combinatorial trilayers

Six wedge samples were made on 5 × 15 mm^2 MgO(110) substrates, where CoPt/Cu/Fe hard-magnetic/non-magnetic/soft-magnetic trilayers were grown by electron-beam (e-beam) evaporation. The 30 nm CoPt hard magnetic layer was epitaxially grown using a 1 nm Pt buffer layer at a temperature between 422 and 426 ºC (Tab. 5.1). The hard layers were post-annealed at 400 ^{o}C for 45 to 90 minutes typically. Then, the temperature was gradually reduced, and by 320 ^{o}C the heater was turned off. We utilized the temperature gradients in the substrate holder to vary the crystallinity and the coercive field (H_c) of the hard phases (Tab. 5.1). At less than 100^{o} C, a wedged layer of Cu was deposited with thickness t_{Cu} varying between 0 nm and 2.3 nm, except for Sample 1, where 0 nm ≤ t_{Cu} ≤ 4.9 nm. Subsequently, the Fe soft layers were directly grown on the Cu layers with thicknesses t_{Fe} of 1.5 nm, 3.0 nm, or 4.0 nm. To prevent oxidization, the multilayers were capped by a 7.5 nm thick Au layer deposited at 70 ^{o}C. Per wedge sample, there were 28 spots of measurement with a center-to-center separation of approximately 0.53 mm (see Fig. 5.1).

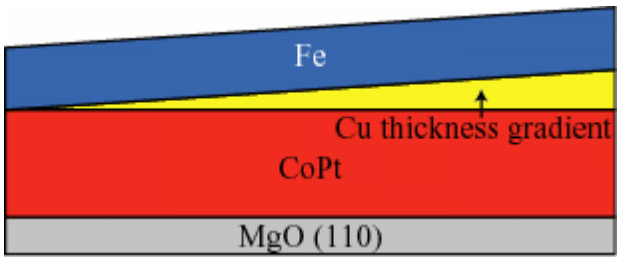

Fig. 5.1 Cross sectional schematic of a wedge sample. The arrows indicate 28 spots per wedge sample.

5.3 Results and discussion

5.3.1 Crystallinity of CoPt hard layer

Fig. 5.2 shows a typical XRD pattern. The deposition of CoPt on MgO (110) by e-beam evaporation typically results in a long-range chemical ordering of the epitaxially grown $L1_0$ phase. The substrate deposition temperature determines which of the three different $L1_0$ phase orientations, one with the tetragonal *c* axis parallel to the substrate surface orientation (*hh*0) or two with the tetragonal *c* axis inclined at approximately 45^o respect to the substrate normal, orientations (0*hh*) and (*h*0*h*), will be predominant.[10] As expected, the analysis of the XRD data displays the presence of the (110) and (220) peaks corresponding to the $L1_0$ phase with in-plane c-axis, the (111) peak coming from a polycrystalline phase and the (202) peak corresponding to the other two epitaxial orientations. The (110) peak has a negligible contribution from the polycrystalline phase. Two extra peaks can also be observed, the Au (111) coming from the cap layer and the MgO (220) coming from the substrate.

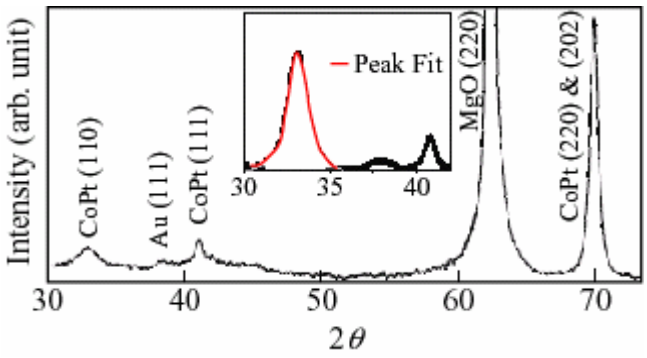

Fig. 5.2 Typical XRD pattern. Sample: MgO (110) / CoPt (30 nm) / Cu (t_{Cu}) /Fe (3 nm) / Au (7.5 nm).

5.3.2 Effective grain size of the CoPt hard layer

We characterize the CoPt hard with the effective grain size *D* of the $L1_0$ *c*-axis in-plane phase (Tab. 5.1). This is the orientation with its magnetic easy axis along the substrate plane.

Sample	***CoPt Dep. T (^oC)***	***t_{Fe} (nm)***	***H_C (T)***	***I***	***D (nm)***	***H_d (T)***	***t_d (nm)***
1	422	3.0	0.13 ± 0.01	AFM	7.4 ±0. 3	0.023 ± 0.01	3.3 ± 1.5
2	422	3.5	0.50 ± 0.04	AFM	7.9 ± 0.1	0.058 ± 0.01	7.0 ± 2.5
3	422	1.5	0.70 ± 0.05	AFM	13.5 ± 0.22	0.220 ± 0.03	15.3 ± 10.0
4	426	3.5	0.80 ± 0.06	AFM	10.1 ± 0.2	0.105 ± 0.009	103. ± 6.0
5	426	4.0	0.95 ± 0.07	AFM	7.7 ± 0.7	0.074 ± 0.008	3.8 ± 2.0
6	422	3.5	1.40 ± 0.10	FM	14.8 ± 0.5		

Tab. 5.1 CoPt *Dep. T* is deposition temperatures, H_C is the CoPt coercive field, *I* is the type of interaction, *D* is the effective grain size of $L1_0$ *c*-axis in plane phase, H_d is the dipolar field, and t_d is the dipolar field decay length.

D was calculated from the Sherrer's formula:[61]

$$D = \frac{\lambda_{\alpha 1}}{W \cos\theta} \tag{5.1}$$

where *W* is the full width at half maximum intensity of the (110) peak corresponding to the wavelength ($\lambda_{\alpha 1}$) of the $CuK_{\alpha 1}$ source diffactometer, and 2θ is the peak's centroid. To separate the superposition of the $K_{\alpha 1}$ and $K_{\alpha 2}$ peaks, two Lorentzian functions were combined to fit the (110) peaks (inset Fig. 5.2). The uncertainties in *D* were estimated as half of the difference between the values of *D* obtained with the two XRD machines.

5.3.3. Direct observation of microstructure of CoPt hard layer

Fig. 5.3 displays the cross-sectional TEM images of three wedge samples. The CoPt hard layers of Sample 4 (Fig. 5.3(a)) and Sample 2 (Fig. 5.3(b)) show Stranski-Krastanov-like island-type growth mode. On the other hand, the CoPt hard layer of Sample 6 shows Frank-Van der Merwe layer by layer growth mode, which is observed in the TEM image of the CoPt layer discussed in the previous chapter. Since Stranski-Krastanov mode takes place when the surface mobility of atoms are lower than that of Frank-Van der Merwe mode, we believe that the actual temperature of CoPt of Sample 4 and Sample 2 during CoPt layer growth might have been lower than the CoPt layer of sample 6 and CoPt layers discussed in the last chapter.

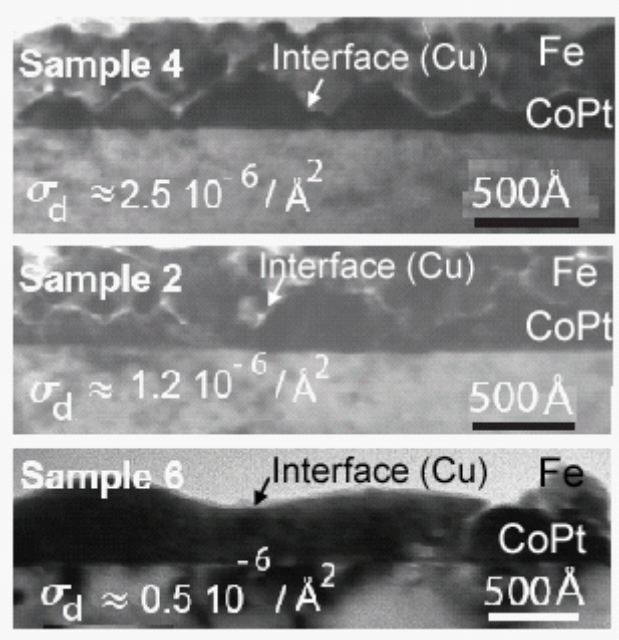

Fig. 5.3 TEM cross-sectional bright images. Roughness $\sigma_d \approx$ (# of hills / length)^2.

We determined the square normalized linear island-peak densities from the TEM images to characterize the hard-phase roughness (σ_d).

5.3.4. Nucleation field dependence on thickness of copper non-magnetic layer

From each magnetization loop, the nucleation field (H_N) was experimentally determined by the point on the curve where the drastic change in the slope takes place. This value was equated to the value of H where the tangent to the loop at the point with maximum magnetization intercepts the tangent to the loop at the point of maximum slope (inset of Fig. 5.4(a)).

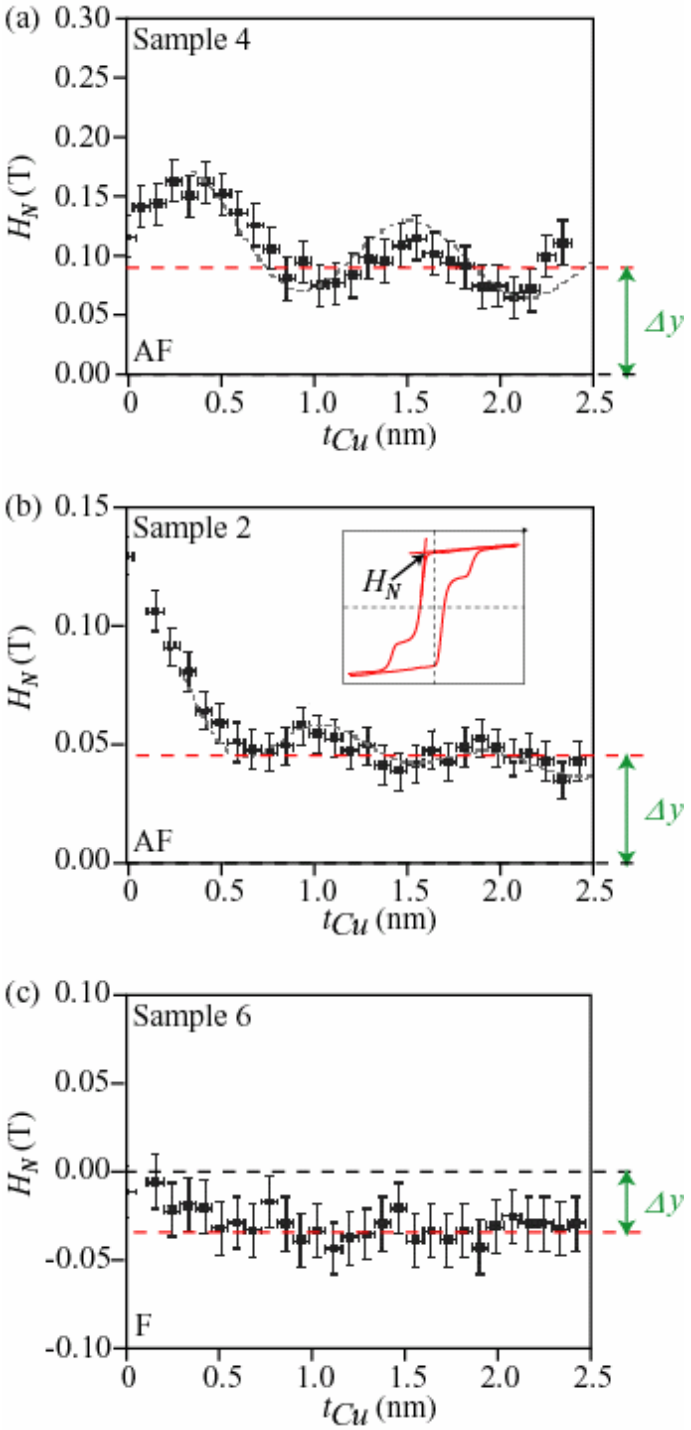

Fig 5.4. Nucleation Field (H_N) vs. Cu spacer thickness (t_{Cu}). Dashed gray line is the fit to Equation (2). Inset: normalized magnetization hysteresis loop and graphical definition of H_N. (a) $D \approx 7.9$ nm, (b) $D \approx 10.1$ nm, and (c) $D \approx 14.8$ nm.

Fig. 5.4 displays typical examples of H_N vs. t_{Cu} data points. There is a characteristic oscillatory behavior of the CoPt and Fe layer coupling on t_{Cu}. The oscillatory behavior of H_N can be interpreted from the Ruderman-Kittel-Kasuya-Yoshida (RKKY) model,[62,63] which explains the nature of oscillatory exchange coupling of ferromagnet/non-magnetic spacer/ferromagnet systems with a varying non-magnetic interface spacer thickness. Figure 5.4(b) also shows that only 0.5 nm of Cu can change H_N by 60 %. This indicates that a small amount of non-magnetic impurity at the interface of soft-hard magnet systems can significantly alter H_N.

The data shown in Fig. 5.4 exhibits displacement along the y-axis (Δy). This cannot be directly explained by exchange coupling interaction (Fig. 5.5(a)). To understand this effect we refer to the description of the mulilayer system given by Marguelies *et al*.[64] Their interpretation is that the RKKY model can explain the oscillations, while the offset is the result of an exponential effect arising from the presence of a large dipolar field (Fig. 5.5(b)). This field comes from a columnar granular structure with nonmagnetic grain boundaries in both layers.

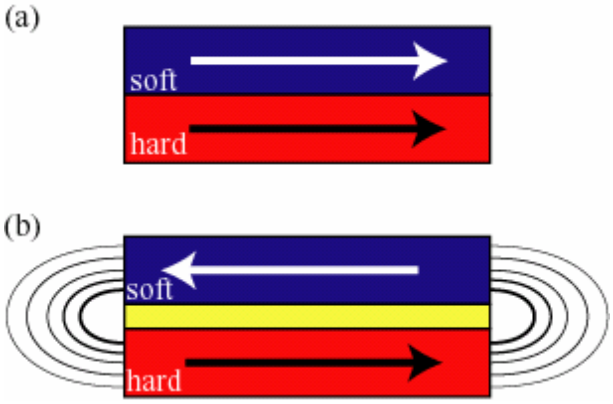

Fig. 5.5 (s) Cross-sectional schematic of soft/hard magnetic bilayer. Arrows denote the magnetization of the each layer. The magnetizations are ferromagnetically aligned due to the exchange coupling. (b) Cross-sectional schematic of soft-magnetic/non-magnetic/hard-magnetic trilayer. The magnetizations are antiferromagnetically aligned due to the dipolar interaction.

To fit the data in Figure 5.4 (dashed curves), we consider that H_N consists of two terms: RKKY-like and an exponential decay offset term, which represents the dipolar contribution.

$$H_N(t_{Cu}) = H_o \frac{T_e t_{Cu}/\alpha}{\sinh(T_e t_{Cu}/\alpha)} \frac{\sin(\phi + 2\pi t_{Cu}/\lambda)}{(2\pi t_{Cu}/\lambda)^p} + H_d e^{-t_{Cu}/t_d} \qquad (5.2)$$

where T_e = 300 K, the constants H_o, ϕ, p, λ, and α = 480 nm K characterize the RKKY-like interaction.[64,65] H_d is the dipolar field for t_{Cu} = 0 and t_d is the characteristic decay length of the dipolar field. The exact functional form used for the oscillating RKKY term has little bearing on the parameters for the dipolar term,

although fits are done only for t_{Cu} > 1 Cu monolayer (*ML* ~ 0.36 nm), in order to avoid sensitivity to the actual form of the RKKY term. Tab. 5.1 and Tab. 5.2 list the fitting parameters.

Sample	***H_o (T)***	***λ (nm)***	***Φ***	***P***
1	0.03	0.80 (2.2 ML)	0.0	0.75
2	0.06	0.87 (2.4 ML)	0.0	0.95
3	0.60	1.08 (3.0 ML)	$\pi/2$	1.80
4	0.17	1.05 (2.9 ML)	$\pi/2$	0.85
5	0.03	0.90 (2.5 ML)	$\pi/2$	0.80

Tab. 5.2 H_o, ϕ, λ, and p are RKKY model parameters. H_o is representative of the intensity of the exchange interaction, ϕ is related to the topology of the Fermi energy, λ is the period of the oscilations (associated to the Fermni wavelenght), and p is associated with the planarity of the geometry (p = 2 for planar geometry).[63]

For positive values of H_N, the strong dipolar interaction favors the antiparalell alignment of the hard-soft phases (*AFM* coupling) [Fig. 5.4(a) and (b)] . For neagtive H_N, a much weaker dipolar interaction favors the parallel alignment of the magnetic moments between the hard-soft phases (*FM* coupling) [Fig. 5.4(c)]. When $H_N \leq 0$ there is a strong *F* interaction arising from the hard-phase pinning effect and the hard layer controls the reversal in this instance and the sytems cannot be modeled by the regular RKKY theory.

5.3.5 Nucleation field dependence on interface roughness and grain-size of CoPt hard layer

The combination of TEM data and the resulting fits show, maybe say is one sometimes along we expect this, that H_d scales with σ_d (Fig. 5.6). Fig. 5.7 suggests there might also exist a correspondence between H_d and D. The dipolar interaction increases for increasing D up to a certain maximum and then it reduces to ≈ 0. These experimental observations are in agreement with a simple classic electromagnetic picture, in which the dipolar field generated by an individual grain depends on the grain size due to the relative orientation of the magnetic poles located on the grain boundary. The fact that D << typical island size ≈ 100 nm (which determines σ_d) would indicate that the magnetic poles localized in the grain boundaries could also be a source of dipolar field. This grain boundary effect would add up to the σ_d effect to produce the total H_d.

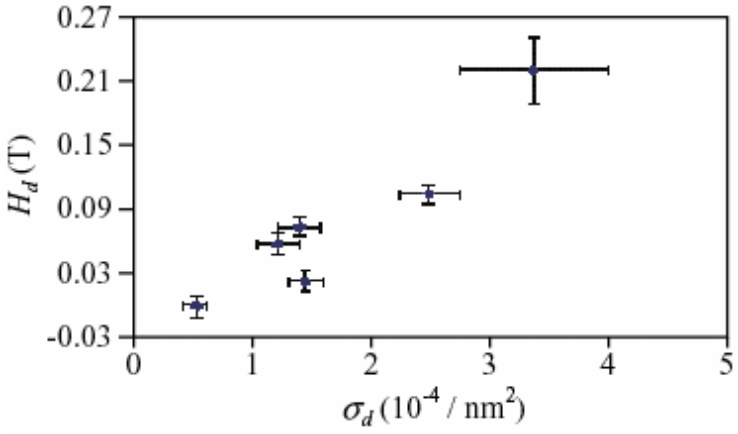

Fig 5.6 Dipolar Field (H_d) vs. Roughness (σ_d).

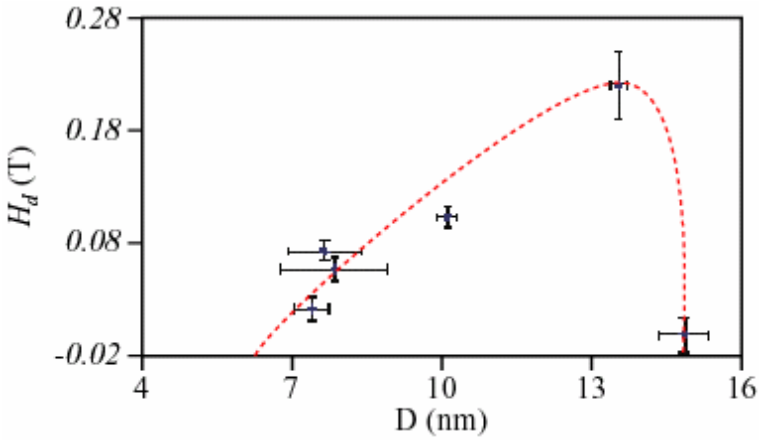

Fig 5.7 Experimental data: dipolar field (H_d) vs. effective grain size of $L1_0$ phase with *c*-axis in plane (D).

High-resolution TEM images (not shown) have verified that the Fe layers were polycrystalline, suggesting that the hard phase was the main source of possible dipolar field. The polycrystalline soft phase does not contribute to the dipolar field because of its random magnetic easy-axis orientation (magnetic poles average out). On the contrary, it could contribute to separate grains as the nonmagnetic boundaries do.[64]

Experimentally and theoretically, it is generally assumed that the effect of the dipolar field is negligible in 1d systems.[53,59,66] In addition, traditional 1d models assume that the interlayer interaction only depends on the dimensions of the soft phase. But our system is 2d or quasi 2d. Contrary to traditional 1d models, the present work shows that dipolar interaction can not only be present in 1d systems but can also strongly depend on the hard layer features.

In 3d nanocomposite magnets, especially in those systems made by compressed nanoparticles, we could expect to find polycrystalline regions or

nonmagnetic grain boundaries, e.g. impurities. This would give rise to a large dipolar field favoring the antiparallel alignment of the hard-soft phases. Independently of the hard phase material, the way to reduce this effect is by increasing the hard phase effective grain size and reducing the non magnetic grain boundary and non magnetic regions between hard and soft phases.

5.4 Conclusion

In summary, we have systematically investigated thickness gradient effects of a Cu interface layer on the interaction between a CoPt hard magnetic layer, grown at 422 ^{o}C and 426 ^{o}C, and a Fe soft layer. We have observed a RKKY-oscillatory behavior of H_N vs. t_{Cu} with decreasing amplitude in addition to an exponential decay. The latter is a consequence of the presence of the dipolar interaction in nanocomposite magnets. We also found that a small amount of non-magnetic impurity (~ 0.5 nm in thickness), at the interface of soft-hard magnet systems, can significantly alter H_N (by as much as 60 %). A correlation between the effective grain size of the CoPt $L1_0$ phase with the tetragonal *c*-axis lying in the in plane direction and the dipolar interaction is observed. This suggests that besides the interface roughness, another factor that might determine the dipolar interaction is the effective grain size and non-magnetic or polycrystalline grain boundary of the hard phase. (Only for hard phases with large or very small grain sizes, dipolar interaction is negligible.) Therefore, to reduce dipolar effects in nanocomposite magnets, the hard phase effective grain size must be increased, and the roughness as well as the volume of the non-magnetic regions between hard and soft phases must be minimized.

Chapter 6 Introduction to combinatorial investigation of hydrogen storage materials

Due to rapid increase of social needs to find an alternative fuel, especially for transportation, it is essential to discover new lightweight hydrogen storage materials as soon as possible.[67,68] So far, most of exploration is carried out through the conventional one-by-one approach. The combinatorial approach, which enables one to study a large number of compositionally varying samples, has not been widely applied to the problem of multi-component metal hydride discovery to date. A few groups are using the combinatorial approach for systematic and comprehensive study of hydrogen storage materials.[25,69-71] In order to further add benefits of the combinatorial approach to this field, we have developed a new high-throughput combinatorial methodology with an emphasis on novel characterizing technique.

In this chapter, social background prompting the application of hydrogen as a new energy carrier is briefly discussed. Then, basic information on hydrogen storage intermetallics is introduced to aid the understandings of the topic.

6.1 Hydrogen as a new energy source for transportation

The demand for an efficient and clean fuel alternative has increased in recent years[72] and is expected to become more pronounced in the future,[73,74] since many automotive companies have announced the potential introduction of commercially available hydrogen vehicles as early as 2010. A hydrogen vehicle is a

vehicle that uses hydrogen as its on-board fuel for motive power. The power sources of such vehicles convert the chemical energy of hydrogen to mechanical energy in one of two methods: combustion, or electrochemical conversion in a fuel cell: in combustion, the hydrogen is burned in engines in fundamentally the same method as traditional gasoline cars. In fuel cell conversion, the hydrogen reacts with oxygen to produce water and electricity, the latter of which is used to power an electric traction motor (Fig. 6.1).

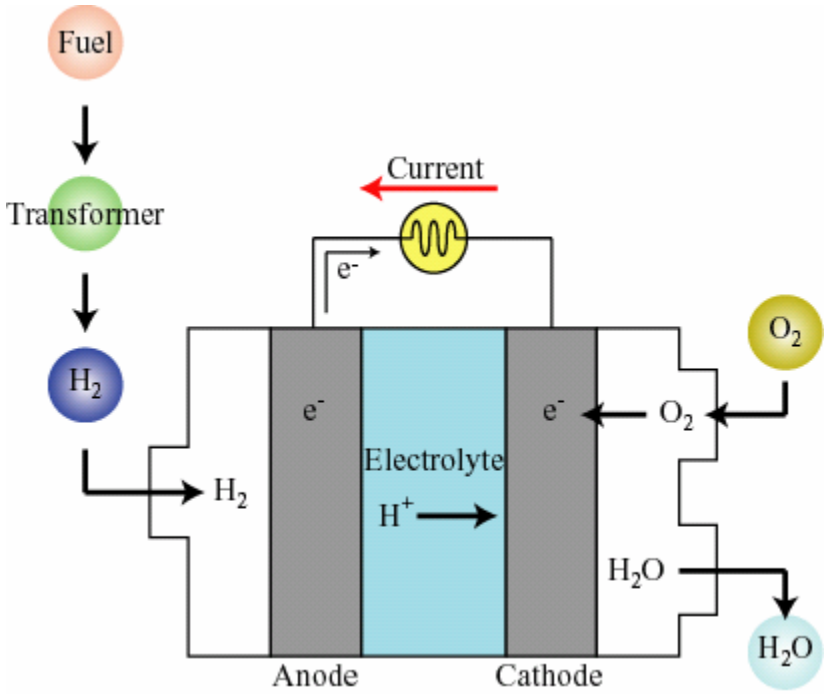

Fig. 6.1 Working principle of the fuel cell (after T. Honma[75]).

6.1.1 Advantages and challenges of hydrogen vehicles

Hydrogen is considered one of the best alternative fuels[76-78] due to its abundance, easy synthesis, and non-polluting nature when used in fuel cells.[79,80] If the hydrogen economy is established, the largest impact can be on transportation such

as automobiles. For example, converting all on-road vehicles to hydrogen vehicles (Fig. 6.2) may improve air quality, health, and the climate significantly, whether the hydrogen is produced by steam reforming of natural gas, wind electrolysis, or coal gasification.[81] In addition, it could reduce reliance on diminishing oil supplies. However, the introduction of hydrogen as a fuel for on-board applications presents several problems in developing the required technologies: production,[82] transportation,[83] and storage. In our research, we are interested in the storage aspect. For the discovery of new hydrogen storage materials, the combinatorial approach which enables rapid and systematic investigation is a powerful tool.

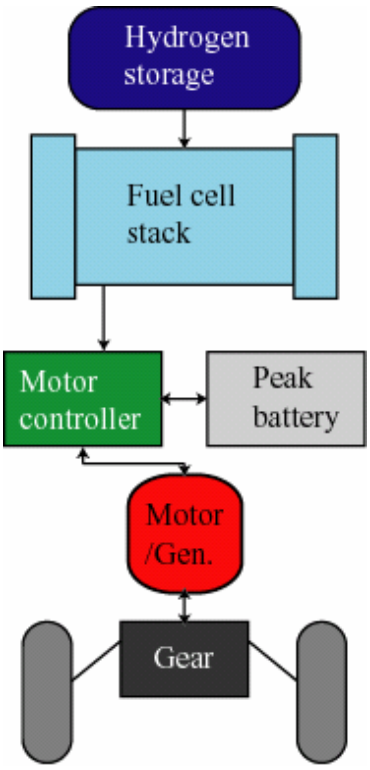

Fig. 6.2 Hydrogen storage fuel cell vehicle (after J. M. Pgden[84]). The fuel cell stack generates electrical current from hydrogen. Generated current is used to operate mechanical parts of the vehicle. The peak battery is used to assist the fuel cell in meeting peak demand, such as high speed running.

6.2 Hydrogen storage

The expected hazards involved in storing and using gaseous or liquid hydrogen in high-pressure vessels have triggered research on more safe and efficient ways for hydrogen storage for different applications.[68] Especially for on-board applications, extremely efficient hydrogen storage methods from both gravimetric and volumetric standpoints are essential.[85] The main challenges in the field of hydrogen storage are to devise new materials or combinations of materials which exhibit 1)

high volumetric/gravimetric capacity,[86] 2) fast sorption kinetics at near-ambient temperatures, and 3) high tolerance to recycling.

6.2.1 The Department of Energy target

The year 2010 Technical Targets of the U. S. Department of Energy (DOE) for on-board hydrogen storage systems are; 6 wt% reversible capacity, -40 to 80 ℃ hydrogen desorption temperature, and 5 min for charging a 5 kg system (Tab.6.1).[87] However, the current state of the art materials exhibit properties that fall far short of these targets. For example, $Mg(BH_4)_2$ was developed in 2007, and showed 9 – 12 wt% hydrogen storage capacity, but its hydrogen storage capability is not reversible, and the desorption temperature is too high (~ 350 ℃).[88]

Targeted Factor	2005	2006	2007
Specific energy (MJ/kg)	5.4	7.2	10.8
Hydrogen (wt%)	4.5	6.0	9.0
Energy density (MJ/L)	4.3	5.4	9.72
System cost ($/kg/system)	9	6	3
Operating temperature (ºC)	-20/50	-20/50	-20/50
Cycle life-time (absorption/desorption cycles)	500	1,000	1,500
Flow rate (g/s)	3	4	5
Delivery pressure (bar)	2.5	2.5	2.5
Transient response (s)	0.5	0.5	0.5
Refueling rate (kg H_2/min)	0.5	1.5	2.0

Tab. 1 DOE hydronge storage targets.

6.2.2 Various ways of on-board hydrogen storage

On-board hydrogen storage approaches currently under investigation include high capacity metal hydrides,[89] high surface area sorbents,[90] chemical hydrogen storage carriers, low-cost and conformable tanks, compressed/cryogenic hydrogen tanks, and nanostructured materials.[91]

6.2.3 Hydrogen storage intermetallics

Metal hydrides are a promising means of effectively storing hydrogen due to their high storage capacities at low pressures, whil they also maintain volumetric densities comparable to that of liquid hydrogen.[68] The highest volumetric densities of hydrogen in any material are found in metal hydrides (Fig. 6.3), which are defined as a concentrated single-phase compounds involving the host metal and hydrogen.[92] Metal hydrides containing only one metal have limited practical applications in hydrogen storage because of the high thermodynamic stability of these

compounds. For this reason, a wide range of intermetallics with two or more metals have been investigated over the past several decades in order to find a material that meets the practical requirements.

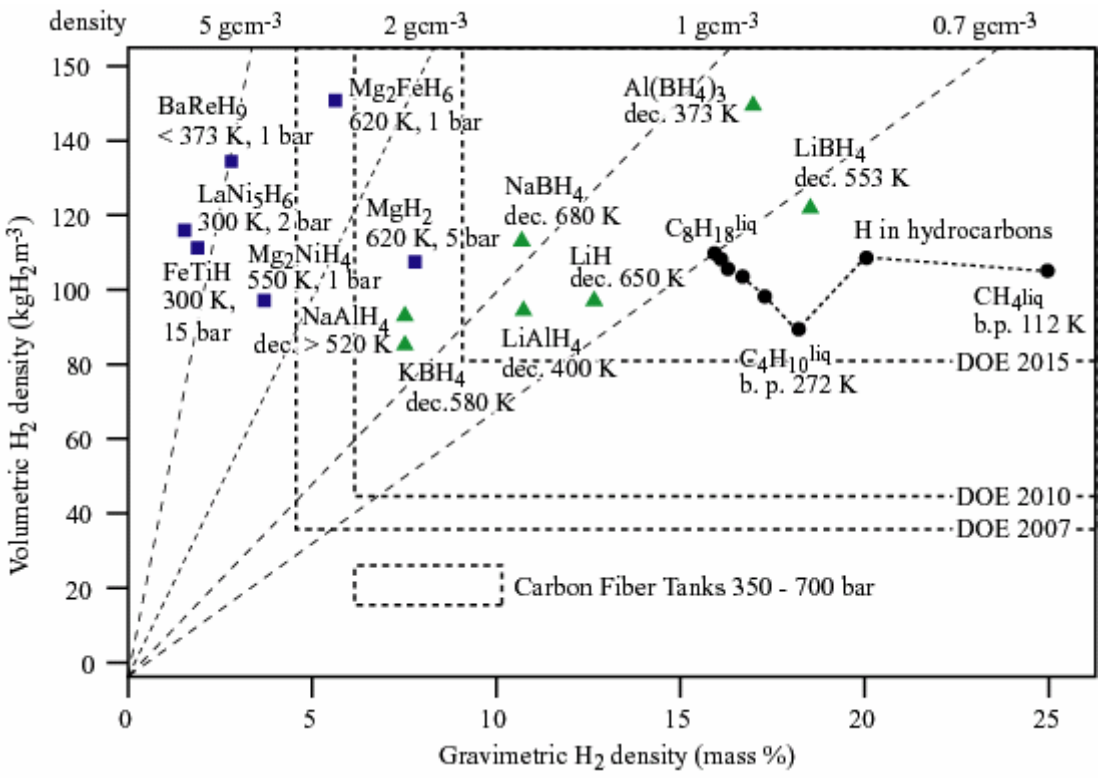

Fig. 6.3 Gravimetric and columetric densities, and corresponding specific energies and energy densities, of a variety of hydrogen storage media. The U.S. DOE targets for 2005, 2010, and 2015 are indicated within the shaded regions. The values reported for the metal hydrides, complex hydrides, and other hydrogen-storage materials are based on the absolute (theoretical) amount of hydrogen (after A. M. Seayad[92]).

Chapter 7 Infrared imaging; new methodology of hydrogen absorption/desorption

As discussed in Chapter 1, in any type of combinatorial investigation, having the correct characterization tool is critical. For the investigation of hydrogen storage materials, high-throughput screening techniques to identify high capacity hydrogen storage materials with fast absorption and desorption are needed. Following a previous work by a General Motors' group,[70] we chose infrared imaging as a high-throughput screening technique. This method relies on dramatic changes in optical transparency and IR emissivity of films as a response to hydrogen absorption and desorption. IR emissivity of a solid is expected to change with hydrogen adsorption and desorption as a result of changes in its electronic and vibrational energy states, as well as its crystallographic structure. Compared with General Motors previous work, our novel way to use infrared imaging as high-throughput measurement technique enabled us to study dynamics of hydride formation, in addition to hydrogen absorption and desorption.

In this chapter, we describe the design of our in-house IR imaging set up. We demonstrate how we analyze the obtained images to extract useful information from them by looking at data from an experiment where we studied the Pd thickness effect on IR imaging.

7.1 In-house infrared imaging set up

We developed a new infrared (IR) imaging set up. This allows one to study in-situ hydrogen absorption and desorption properties of the entire combinatorial thin films by collecting IR images. Figure 7.1(a) shows a schematic diagram of the in-house IR imaging set up. A reaction chamber is made of stainless steel with ≈ 1.0 in. wall thickness. To allow easy access to inside of the chamber, it has six 4-1/2 in. flanges. One of them has open hole on it to pass IR emission of sample. The gas pressure of the reaction chamber is measured by a pressure gauge (Swagelok PGI-100B-PG100-L AQ X-ABH J). Ultra high-purity hydrogen gas (99.999 %) is used to hydrogenate the samples. Normal purity (99.9 %) Ar gas is used to purge the reaction chamber before each measurement. Both types of gases are injected into the reaction chamber by manually opening a valve (Swagelok SS-62TS4). For safety, the extra pressure is released from a back pressure regulator (Swagelok 6342A). An end connection (Swagelok SS-67TSW24T) connects the reaction chamber to dual cryogenic sorption vacuum pumps (MDC Vacuum Products, 500004). These liquid-nitrogen-cooled cryo-pumps can pump the reaction chamber down to 1 x 10^{-3} Torr (≈ 1 x 10^{-6} bar). A sapphire window (φ = 1-3/4 in., 1/4 in.-thick) is put on a 1-1/2 in. diameter opening centered on a 4-1/2 in. flange. Rubber o-rings are placed at contact surfaces of the sapphire window and the flange to ensure the sealing. A heating sample stage (HeatWave Labs, Inc. 101303-23) is mounted on two copper rods electronically connected with a temperature controller (HeatWave Labs, Inc. 101303-23). Figure 7.1(b) shows the schematic top view of the heating stage. The figure also shows a Mg thin film sample and a k-type thermocouple clamped on the top of the

stage by stainless steel plates screwed on by 1/16 in. stainless steel screws. The heating stage mainly consists of an inner frame (φ = 1.10 in.) and an outer frame (φ = 1.35 in.). A resistive wire is embedded in the inner frame near the surface, and a gap between the inner and outer frames isolates the inner frame and increases the heat efficiency. It can stand temperature up to around 1200 ºC in ultra-high vacuum. The temperature of the heating stage monitored by a k-type thermocouple is controlled within 1 ºC accuracy. The stainless steel plates clamping the thin film sample on the middle of the heater are symmetrically placed in order to apply force homogeneously across the substrate, which maintains constant temperature across the sample.

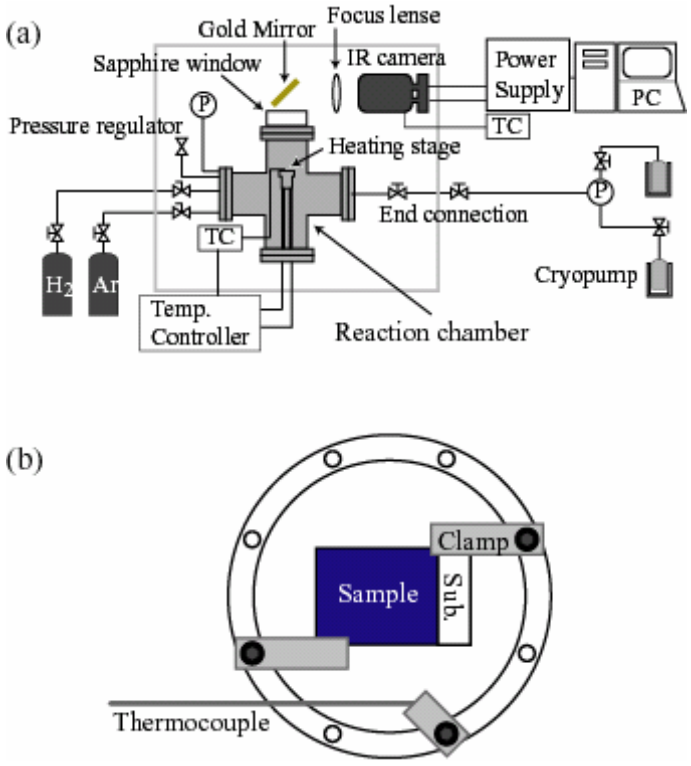

Fig. 7.1 (a) Schematic diagram of the IR imaging set up. TC, P, PC denote the k-type thermocouple, the pressure gauge, and the personal computer, respectively. (b) Top view schematic of the heating stage.

The IR light with a shorter wavelength than ≈ 5.5 μm emitted from the heating stage including sample on it can travel trough the sapphire window facing the heating stage. Then the IR light is reflected by the gold mirror and focused on the InSb IR detector of an IR camera (Talktronics Inc. FPAHB-1). A micrometer attached to the base of the IR camera allows us fine tuning of distance between the focus lens and the InSb detector in order to optimize the focus of the light. The InSb detector consists of 256 x 256 pixels. Both-side-polished Si wafers, placed between the reflection mirror and the focus lens, attenuate the IR intensity in order not to saturate the InSb detector. To increase the signal to noise ratio by avoiding unfavorable IR emission from surroundings, the vessel of the IR detector is kept cooled by liquid nitrogen at 77.4 ºC. Its temperature is monitored by means of a second K-type thermocouple inserted into the vessel of the detector. The IR camera is internally triggered at 25 Hz to permit "snap-shot" imaging with 10 microsecond or longer integration times. By setting right timing on the PC, the custom made software (Talktronics DTSpec 4.0 Imaging Spectrometer R 2.22 F) periodically collects integrated IR emission signals, which is amplified by an amplifier attached to the camera, and converts signals to the IR image consists of 256 x 256 IR intensity data matrix at any rate less than 25 Hz. Simultaneously, the 256 x 256 data matrix is stored in PC as a binary file. The camera has its peak sensitivity at a wavelength of 5 micrometers, but it is able to detect over an integrated range of 1.0 to 5.5 microns to increase total intensity. In the reference mode, which we exclusively use in our study because this mode is sensitive to slight changes, an IR image collected at room

temperature is used as a reference. The IR intensity of each pixel is defined as (IR intensity at measurement temperature) – (IR intensity at room temperature). On the obtained IR image of a Mg thin film on a Si (100) substrate (Fig. 7.2), the Si substrate is bright, but the Mg thin film is dark. This is because, in general, metallic materials such as Mg have low IR emissivity, but insulating materials such as Si have high IR emissivity. The reaction chamber, the reflection mirror, the focus lens, and the IR camera are set on a 30 in. length x 26.5 in. width x 1/4 in. thickness breadboard. For safety, these are contained in the protection container (29-3/4 in. length x 33.5 in. width x 40 in. height) with two doors which allow us to access the inside of it.

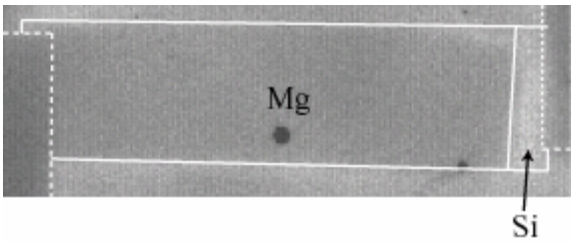

Fig. 7.2 IR image of a Mg thin film on a Si substrate clamped on the heating stage.

7.2 Demonstration of infrared image analysis using study and the effect of a Pd capping layer on infrared imaging

Pd is commonly used in our experiments as a capping layer of hydrogen storage thin films to prevent oxidization and to facilitate splitting of hydrogen molecules at the Pd surface. Thus, before studying hydrogen absorption and desorption of the hydrogen storage materials, we studied how the thickness of the Pd capping layer affects IR imaging. For this purpose, we deposited a Pd(0 – 50 nm) / C

(carbon)(300 nm) bilayer gradient sample on an Al_2O_3 (0001) substrate at room temperature (Fig. 7.3(a)). C was chosen as a good IR emitter (high IR emissivity).[28]

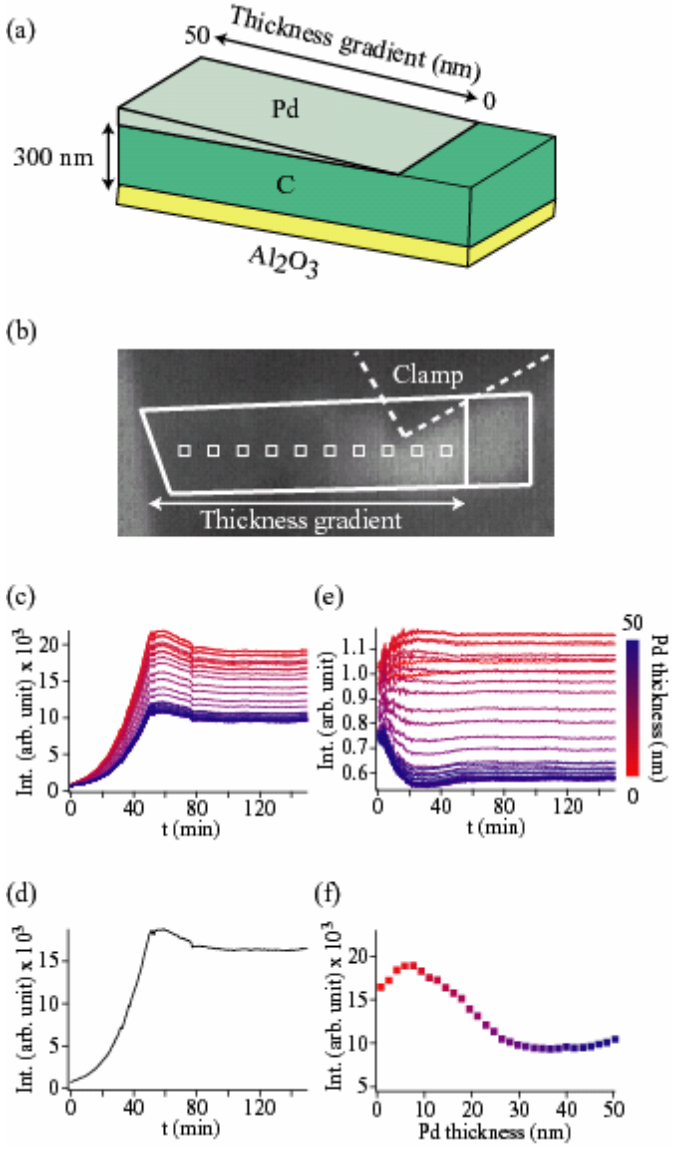

Fig. 7.3 (a) Schematic and (b) IR image of Pd/C bilayer gradient sample. (c) Averaged IR intensity curves of 30 measurement spots along the Pd thickness gradient on region A plotted as a function of time (t). Each curve shows time evolution of IR intensity of each measurement spot. (d) An Averaged IR intensity curve of one measurement spot on region B plotted as a function of time. (e) Offset normalized IR intensity curves of 30 measurement spots along the Pd thickness

gradient on region A plotted as a function of time (t). (f) IR intensity from (c) at t = 120 min vs Pd thickness of the measurement spots.

In order to study the effect of the thickness of the Pd capping layer on the IR imaging, the sample was promptly transferred after deposition to the IR imaging chamber, and then clamped down on the heating stage. The chamber was argon-purged twice and then pumped down to 1 x 10^{-3} Torr or less using the cryo-pump. The IR image of the sample was periodically recorded (every 30 sec) throughout the measurement. The sample temperature (T_s) was automatically increased at 5 ºC/min from room temperature up to 150 ºC, and then T_s was fixed. In order to avoid any effect from gases, pressure of the chamber was kept at its base pressure (1.0 x 10^{-3} Torr). The IR images were analyzed post acquisition using a data analysis software (Igor Pro Version 6.0.3). Figure 7.3(b) is the top view IR image of the sample recorded at 150 ºC. The sample is outlined by the white line, and divided into two regions: region A where the Pd film has its thickness increasing from right to left and region B where the C layer is exposed. The clamp is outlined by the white dashed line. In order to extract the temporal evolution of the measurement spots on the thin film sample with the systematically changed thickness of the Pd layer, 30 square area spots were selected (10 representative square area are shown as the white square boxes in Fig. 7.3(b)). Averaged intensities of each square area, which corresponds to each measurement spot, were collected throughout a set of measurement, and plotted together as a function of time (t) (Figure 7.3(c)). In the same manner, the IR intensity curve of the region B was obtained (Fig. 7.3(d)). This curve was used as a reference.

The Pd thickness of each spot is presented by the curve color according to a color bar on right-hand side of Fig. 7.3(e). The intensity of the each curve increased exponentially with increasing T_s. This behavior agrees with the Planck's law,[28,93] which describes the spectral distribution of the radiation from a blackbody as

$$W_\lambda = \frac{c_1}{\lambda^5} \frac{1}{e^{c_2/\lambda T} - 1}$$

where W_λ ($Wcm^{-2}\mu^{-1}$) is the spectral radiant emittance, λ (μ) is wavelength, T (K) is the absolute temperature, c_1 ($Wcm^{-2}\mu^4$) is the first radiation constant, and c_2 (μK) is the second radiation constant. The set temperature controlled by the temperature controller reached the maximum (150 ºC) at ≈ 50 min and was kept fixed throughout the measurement, but the intensity reached its maximum at ≈ 50 min, and then its value fell until it finally stabilized at ≈ 90 min. This could be because of the overshooting of the heater temperature.

The theoretical prediction of the intensity behavior dependence on the thickness of the Pd top layer is not available, and the dependence can be understood only empirically. In order to pick out how the increasing thickness of the Pd capping layer affects the IR images, the IR intensity of 30 spots on the region A (Fig. 7.3(c)) was normalized using the IR intensity of the region B (Fig. 7.3(d)) as (IR intensity of a selected spot with the Pd capping layer / IR intensity of the reference without the Pd capping layer) and plotted together as a function of time (t) (Fig. 7.3(e)). In Fig. 7.3(e), time evolution of each curve strongly depends on the thickness of the Pd top layer. Only when the thickness of the Pd layer was very thin (less than 2 nm), the

curve stayed at ≈ 1.0 throughout the measurement, which means the effect of the Pd layer was negligible. With up to ≈ 150 nm thick Pd, the intensity initially increased, that is, with temperature, and stayed at more than 1.0. With ≈ 167 nm thick Pd, the curve again stayed at ≈ 1.0 throughout the measurement. With more than ≈ 167 nm thick Pd, the intensity initially decreased with time, and stayed at less than 1.0. Clearly, even very thin Pd top layer affected the intensity behavior.

In order to find the critical thickness (t_c) at which the information from the C bottom layer was completely blocked by the Pd top layer, the raw intensity at t = 120 min was plotted as a function of the Pd thickness for each curve (Fig. 7.3(f)). With up to 30 nm, the intensity first increased, and then it decreased. But the intensity did not change with more than 30 nm thick Pd. This indicated that t_c ≈ 30 nm, and if the thickness of the Pd top layer is more than 30 nm, IR emission from C bottom layer is completely blocked and we can not collect information about the bottom layer. Thus when we want to study a hydrogen storage thin film capped by a Pd layer, the thinner the thickness of the Pd layer is, the better for the IR imaging, and its thickness must be less than t_c.

Chapter 8 Hydrogen absorption/desorption of Mg-based binary composition spread thin films with a Pd capping layer

As discussed in Chapter 6, discovering new lightweight hydrogen storage materials is essential for the practical use of hydrogen as an alternative fuel for transportation.[67,68]

Of the candidate materials, Mg-based alloys show the greatest promise for hydrogen storage materials due to the high gravimetric density of hydrogen in MgH_2. Recently, the optical properties of Mg_xNi_{1-x}[94, 95] and Mg_xTi_{1-x}[96] films, during hydrogen absorption and desorption, were studied for a potential application as switchable mirrors. These studies showed that hydrogenation of the films occurs at temperatures and pressures much lower than needed for bulk alloys and exhibits improved kinetics. We have chosen to study the hydrogen storage properties of the Mg_xNi_{1-x} and Mg_xTi_{1-x} systems more systematically using the combinatorial approach, and demonstrate the utility of our IR imaging technique.

8.1 Experiment

8.1.1 Fabrication of Mg-(transition metal) composition spread thin films

In order to study the composition dependence of hydrogen absorption and desorption behavior of Mg-(transition-metal) (TM) binary systems, we deposited two types of 100 nm-thick $Mg_x(TM)_{1-x}$ thin films (TM = Ni and Ti) with continuous

compositional gradient across Si substrates (Fig. 8.1(a)) at room temperature using the multilayer-deposition technique in a combinatorial e-beam deposition chamber. In the multilayer-deposition technique, after one cycle of shadow mask motion, an atomically thin unit layer, which is composed of wedge-like sub-layers, with the average composition continuously varying along a substrate is deposited (Fig. 8.1(b)). The cycles are repeated hundreds of times, until a film of thickness suitably for characterization has been deposited. The thickness of the wedge-like sub-layer is a key factor in realizing complete mixing of the layers. It was determined via cross-sectional transmission electron microscopy (TEM) that for Mg-TM systems atomic-scale mixing can not be achieved with 2 nm-thick unit layer (Fig. 8.2(c)), but can be achieved with 0.5 nm-thick unit layers (Fig. 8.2(d)). The surface of both samples were covered by 5 nm-thick Pd capping layers to prevent oxidization and to facilitate splitting of hydrogen molecules at the surface.

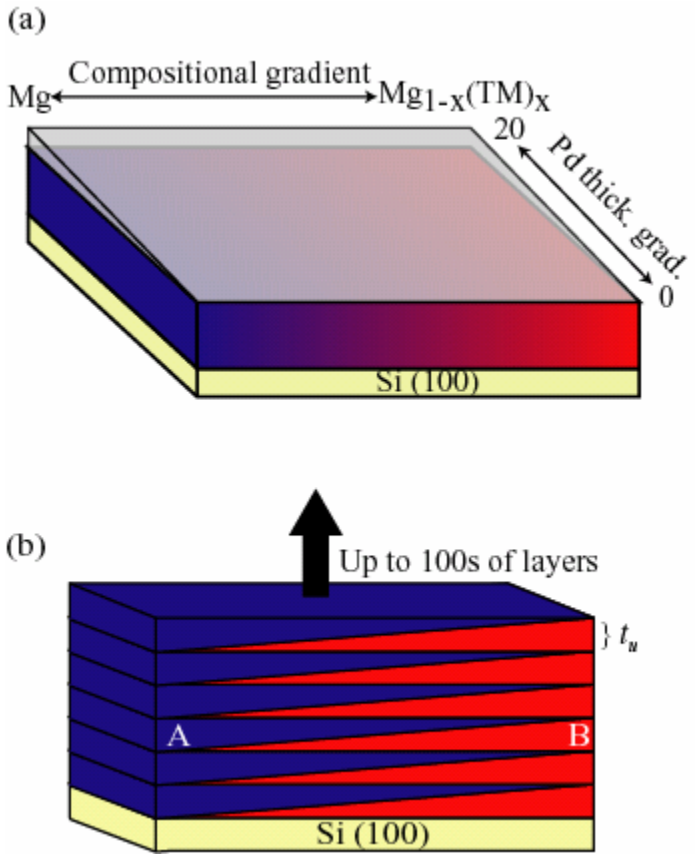

Fig. 8.1 (a) Schematic of $Mg_x(TM)_{1-x}$ composition spread on Si (100) substrate. (b) Synthesis scheme of the multilayer-deposition. The total thickness is obtained after repeating 100s of layers. In order to realize ideal interlayer mixture, the thickness of each unit layer (t_u) is ≈ 0.5 nm.

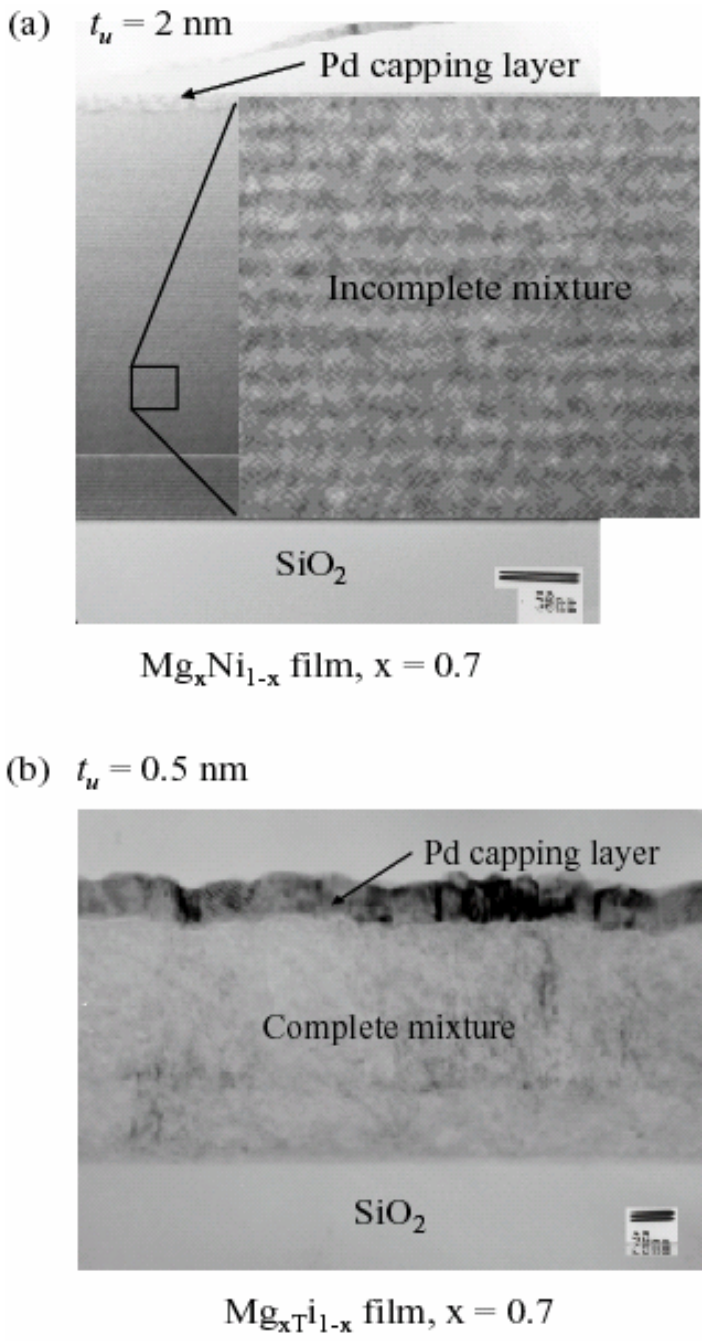

Fig. 8.2 Cross-sectional TEM image of $Mg_x(TM)_{1-x}$ samples with (a) 2 nm unit layer thickness (t_u) and (b) 0.5 nm unit layer thickness. Blow up of the TEM image in (a) shows periodic contrast due to imcomplete mixture of multilayers.

8.1.2 Measurement of composition using energy dispersive spectroscopy

Composition variations of Mg_xNi_{1-x} and Mg_xTi_{1-x} composition spread measured by using energy-dispersive x-ray spectroscopy (EDS) are shown in Fig. 8.3. The measurements are taken every 0.1 cm across the entire spread along the composition gradient. All samples show near-linear variation of composition ($0.4 < x < 0.95$ for Mg_xNi_{1-x} and $0.5 < x < 0.9$ for Mg_xTi_{1-x}). Good run-to-run reproducibility was tested by measuring same kind of more than 10 composition spread samples.

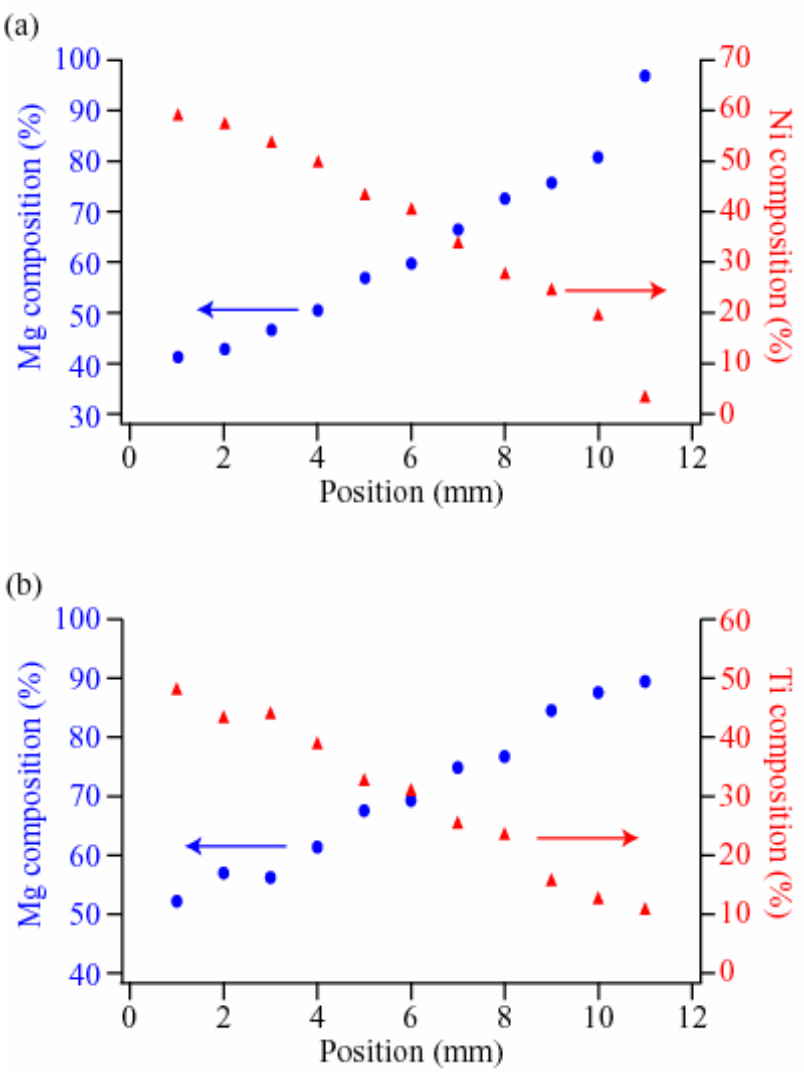

Fig. 8.3 Composition variation of Mg_xNi_{1-x} (red and green squares) and Mg_xTi_{1-x} (blue triangles) films measured by EDS along the composition spread direction every 0.1 cm.

8.1.3 Characterization of crystallinity using x-ray diffraction

Crystallinity of the two types of $Mg_x(TM)_{1-x}$ films was studied using scanning x-ray diffraction (XRD). For each sample, 10 equally spaced measurement spots encompassing the entire composition gradient were chosen. Obtained θ-2θ XRD

scans of Mg_xNi_{1-x} and MgxTi1-x are shown in Fig. 8.4(a) and (b), respectively. Each figure consists of 10 scans taken from the 10 measurement spots with different compositions, which are represented by the curve color according to the color bar on right-hand side. The scans are offset to show results for multiple compositions, with upper scans having the highest Mg composition. The Si (400) peak from the substrate and the Pd (111) peak are seen at 69.1 ° and 40.1 °, respectively, for all the samples.

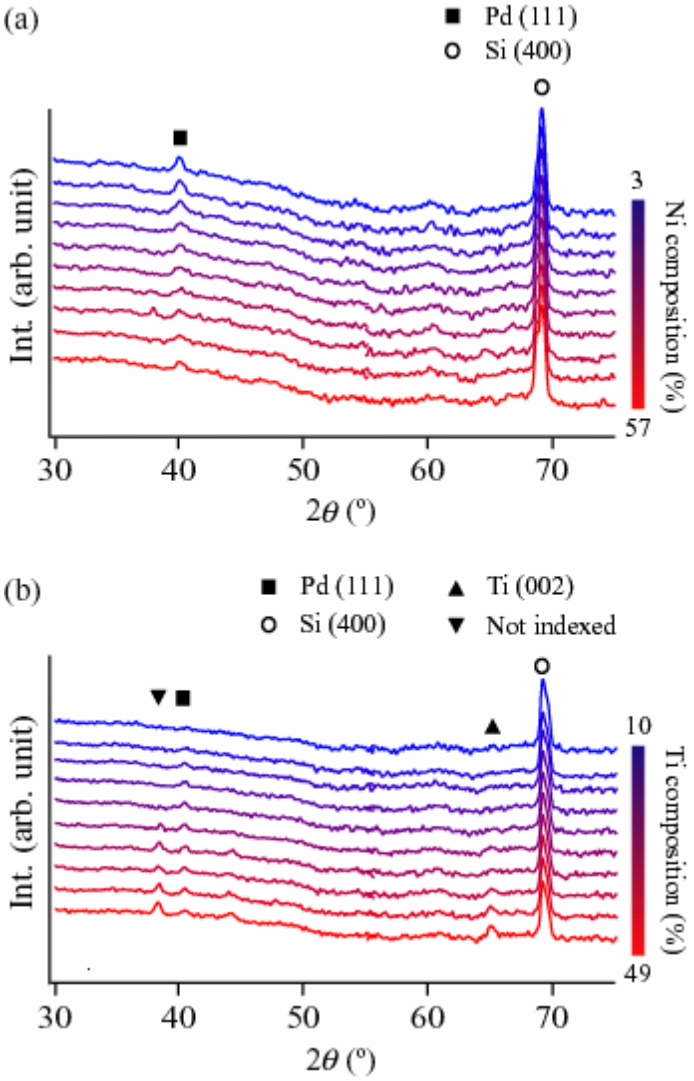

Fig. 8.4 XRD patterns of Mg_xNi_{1-x} (a), and Mg_xTi_{1-x} (c) thin films on composition spreads. Each figure consists of 10 scans, which correspond to 10 measurement spots with different compositions. The scans are vertically offset, with the highest Mg composition cure placed at the top.

The XRD scans of the Mg_xNi_{1-x} thin film (Fig. 8.4(a)) don't show any peaks from the Mg or Ni phases, thus suggesting the entire composition spread is either

amorphous or nano-crystalline. As the time of this writing, TEM studies are in progress to resolve the details of the microstructures. According to recent publications on Mg_xNi_{1-x} films, for different deposition methods, conditions, and substrates, the Mg_xNi_{1-x} films can be either crystalline[97] or x-ray amorphous.[28]

Fig. 8.4(b) shows XRD scans from the Mg_xTi_{1-x} composition spread thin film. No peaks (with the exception of Si and Pd) are detected for the composition range ($0.9 > x > 0.7$). Ti (002), Ti (201), and Ti (004) peaks are observed at around 38.2 º, 77.1 º, and 81.4 º, respectively, for the lower Mg composition range of $0.7 > x > 0.5$. In addition, two unidentified peaks are observed at around 44.2 º and 64.9 º for the same composition range. Since the intensity of these peaks monotonously decreases with decreasing Ti composition, we suspect that this is a presence of an unknown MgTi compound. Note that there are no equilibrium MgTi intermetallic compounds according to the phase diagram.[98] Therefore the unknown phase is either metastable MgTi or a product of an interfacial reaction. The XRD results for Mg_xTi_{1-x} are different from those reported in literature where for higher Mg compositions, the peaks of Mg(Ti) solid-solution phase were seen.[94,95] The discrepancies are probably reflecting the differences in deposition processes and/or the substrate used.

8.1.4 Investigation of hydrogen absorption/desorption using infrared imaging

In order to study composition dependence of hydrogen absorption and desorption behavior of Mg_xNi_{1-x} and Mg_xTi_{1-x} composition spreads, the IR image of

the sample was periodically recorded(every 30 sec) throughout the measurement. Figure 8.5 shows the typical schedule of the measurement. Initially, the sample temperature (T_s) was set to 150 ºC. For about one hour, the IR images were collected without hydrogen gas in order to stabilize the sample temperature and to collect the background intensity. Then the pressure of hydrogen gas (P_H) was changed in a step-wise manner every about one hour until it was pumped out again at around after 7 h. For the first 1 – 4 h, P_H was increased, and we expected to observe change in the IR image due to hydrogen absorption. On the other hand, for 4 – 7 hours, P_H was decreased, and we expected to observe change in the IR image due to hydrogen desorption. But the formed hydride was too stable to be released at T_s = 150 ºC. Thus, in order to ensure hydrogen desorption, T_s was increased to 200 ºC and fixed until the measurement was finished.

8.2 Results and discussion

The evolution of normalized IR intensities with time during hydrogenation experiments are shown for Mg_xNi_{1-x} and Mg_xTi_{1-x} composition spread films in Fig. 8.6(a) and (b), respectively. In these experiments, the films were initially equilibrated at 150 ˚C prior to exposing the samples to hydrogen, thus the change in the film's IR emissivity during hydrogenation could be attributed only to the changes in the amount of hydrogen in a film. Equally spaced 30 measurement spots along composition spreads are selected in the acquired IR images. The offset normalized curves in Fig. 8.6 show evolution of the IR intensity with time for these selected compositions, which are presented by the curve color according to the color bar on right-hand side.

At the top of each figure shows conditions of the hydrogenation experiments: hydrogen pressure P_H (bar) and the film temperature T_s (ºC).

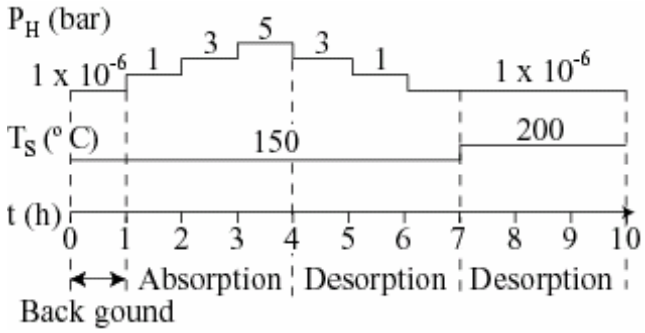

Fig. 8.5 Typical schedule of the measurement to detect hydrogen absorption and hydrogen desorption.

For the Mg_xNi_{1-x} composition spread (Fig. 8.6(a)), the IR intensity for the compositions $x > 0.5$ was increasing immediately after pressurizing the sample with 1 bar hydrogen gas at 150 ºC (1 - 2 h). However, the change was small for the compositions $x < 0.5$. The rate of intensity increase is higher for the higher Mg compositions. Intensities of 3 topmost curves (0.85 – 0.95 atom % Mg) are saturated at $P_H = 1$ bar. However, IR intensities for the x = 0.44 – 0.70 composition range show a secondary increase at $P_H = 5$ bar. This indicates that addition of Ni increases equilibrium hydrogen pressure of absorption. Those curves which have the secondary increase of intensity also showed intensity drop (hydrogen desorption) at $P_H = 1 \times 10^{-3}$ Torr and at $T_s = 150$ ºC (6 – 7 h). At $T_s = 200$ ºC (7 – 10 h), the intensity drops for all compositions. These measurements indicate that for higher Ni concentrations, dehydrogenation occurs at the lower temperature of 150 ˚C, whereas for higher Mg concentrations, it occurs at 200 ˚C. At 200 ˚C, the slope of the intensity decrease is

higher for higher Mg concentrations, probably because hydrogen was not released for these concentrations at 150 ˚C.

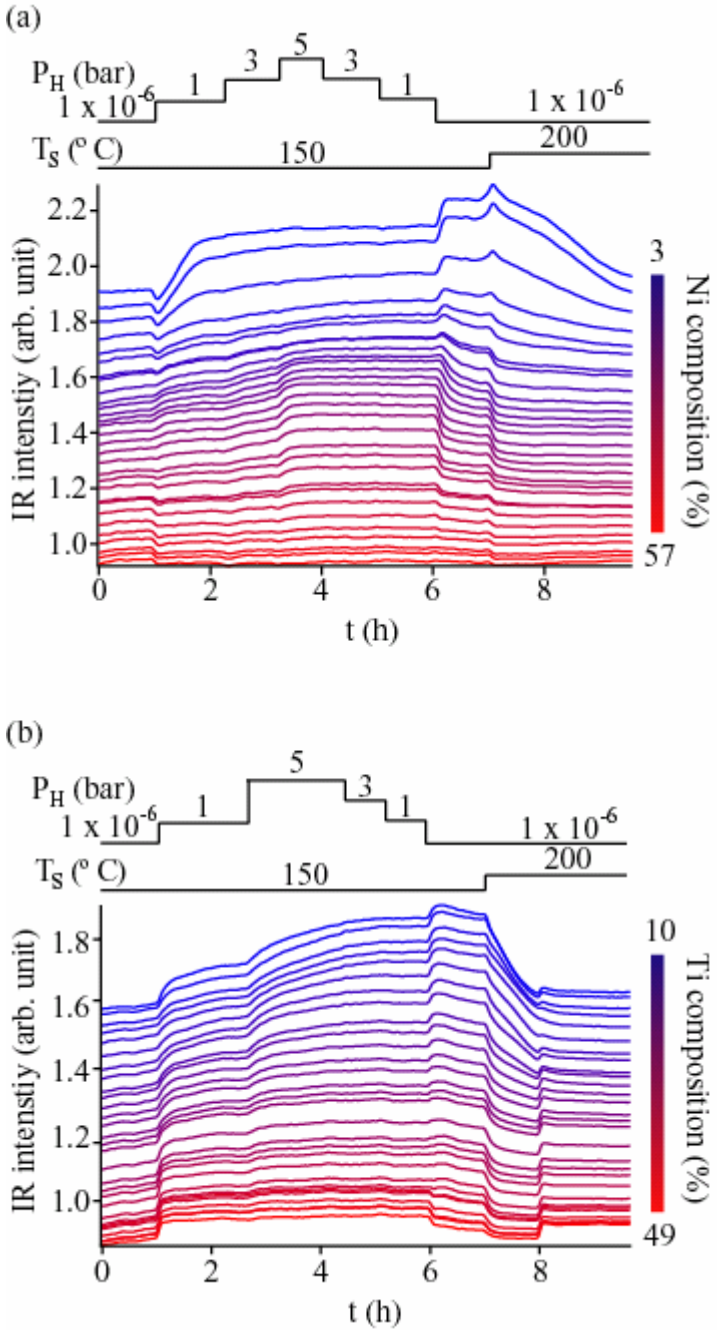

Fig. 8.6 Normalized IR intensity of Mg_xNi_{1-x} (a), and Mg_xTi_{1-x} (c). Equally spaced 30 measurement spots along composition spread are chosen from one edge to another edge for each sample. 30 normalized IR intensity curves as a function of measurement time are vertically displaced for clarity. Lines and numbers on top of

each figure are P_H (bar) and T_S (ºC) samples experienced during the measurement. The sudden intensity change at ≈ 8 h for Mg_xT_{1-x} comes from electronics.

The normalized IR intensity of Mg_xTi_{1-x} is shown in Fig. 8.6(b). For all the composition, the intensity continued to increase both at P_H = 1 bar and 5 bar (1 – 4 h). The decrease in intensity occurred in two-steps with removing of hydrogen pressure, at 150 ºC and at 200 ºC (6 – 10 h). As in the case of Mg_xNi_{1-x} samples, faster hydrogen absorption was observed for the higher Mg compositions. Compared with Mg_xNi_{1-x} samples, the slope of intensity change suggests slower hydrogen absorption rate for Mg_xTi_{1-x}, but faster hydrogen desorption. Intensity changes were not saturated at P_H = 5 bar, which indicates higher equilibrium pressure of absorption.

8.3 Conclusion

The IR imaging experiments with hydrogenation of $Mg_x(TM)_{1-x}$ composition spread films have convincingly demonstrated that the method is able to capture reaction of the films with hydrogen gas – increase of the intensity with adsorption and decrease with desorption. The method resolves different kinetics of hydrogenation for different compositions along a continuous compositional gradient of the films. Judging from the degree of IR intensity increase, the highest hydrogenation at 1 atm/150 ˚C occurs for higher Mg compositions (0.9>x>0.75), with desorption at 200˚C. This was observed for both MgNi and MgTi films and corresponds to the behavior of the Mg phase.

Chapter 9 Systematic investigation of dynamics of hydride formation in MgTi thin films by infrared imaging

The storage of energy represents an important and a challenging element of the overall energy strategy, and hydrogen is one of the principal ways to realize it. The Department of Energy goal for the efficient storage of hydrogen includes a number of difficult requirements for storage materials.[99] One of the most important requirement is hydrogen sorption and desorption. Many researchers have worked as improving the sorption kinetics by investigating new materials and compounds,[100-102] doping materials with catalysts,[103-105] and controlling crystallinity and grain size.[106-111] In general, kinetics of the hydrogen storage materials are estimated from the amount of hydrogen added (or removed) to the material, e.g., pressure-composition-isotherm (PCI) volumetric measurements.[112-118] However, these methods do not allow measurement of the speed of hydride formation. In order to further improve the kinetic properties, better understanding of the mechanisms of hydride formation and growth is desired. In this study, we aimed to develop a novel use of the IR imaging technique which enables us to directly measure kinetics of propagation of hydride transformation front.

9.1 Experiment

9.1.1 Fabrication of $Mg_{0.95}Ti_{0.05}$ thickness gradient thin films

For this study, we designed experiments to measure kinetics of transformation to hydride. Wedge-like films of $Mg_{0.95}Ti_{0.05}$ (Mg95) composition was co-deposited using Mg and Ti sources at 0.2 nm/sec and 0.005 nm/sec deposition rates, respectively. The film was grown on a Al_2O_3 (001) substrate at room temperature using electron-beam deposition, and the linear thickness variation from 0 to 400 nm was created along the 10 mm length (Fig. 9.1(a)). A part of the substrate was intentionally uncovered by the Mg95 thin film for IR imaging to obtain a reference intensity. The sample was capped by a 5 nm thick Pd layer to prevent oxidization and to facilitate splitting of hydrogen molecules at the Pd surface.

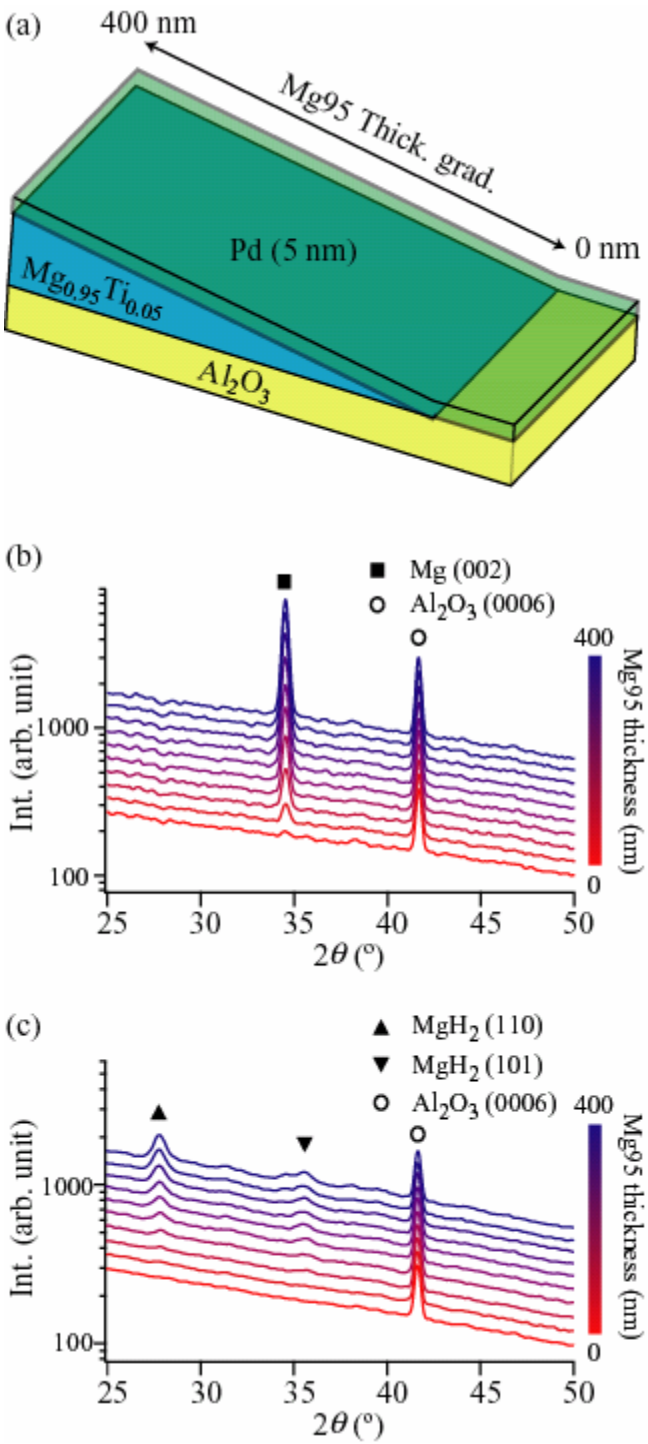

Fig. 9.1 (a) Schematic, (b) θ-2θ XRD patterns before hydrogenation, and (c) θ-2θ XRD patterns after hydrogenation of the thickness gradient Mg95 thin film. Reflection peak position of Al_2O_3 (006), Mg (002), MgH_2 (110), and MgH_2 (101) are

marked by open circles, the black square, the black triangle, and the upside down black triangle, respectively.

9.1.2 Characterization of crystallinity using x-ray diffraction

The crystallinity of an identically deposited sample was measured along the film length using a Bruker D8 scanning x-ray dffractometer (XRD) with an area detector using CuK_{α} radiation (0.15418 nm). In Fig. 9.1(b), ten representative θ-2θ XRD scans of the Mg95 (in logarithmic scale) of different thicknesses are shown. The scans were offset, and thickness of the sample is indicated by the color. The XRD scans show Al_2O_3 (006) peaks at 41.68 ° and Mg (002) peaks at 34.40 °, with the intensity of the Mg peak decreasing with the film thickness. This indicates that the film consists of the epitaxially grown [001]-orientated Mg(Ti) phase.

9.1.3 Investigation of propagation of hydride formation

In order to study the kinetics of hydride formation, the sample was promptly transferred after deposition to the IR imaging chamber, and then clamped down on the heating stage. The chamber was argon-purged twice and then pumped down to 1 x 10^{-6} bar or less using the cryo-pump. First, the sample was heated to 100 ºC at 5 ºC/min, and the temperature was kept throughout the experiment. Recording of the IR images (every 30 second) was started immediately after the temperature reached 100 ºC. For about two hours, the IR images were collected without hydrogen gas in order to stabilize the sample temperature and to collect the background intensity. Then the chamber was pressurized with hydrogen to 1 bar within 60 sec. This pressure was

then kept unchanged throughout the measurement. The schedule of the experiment can be found on top of Fig. 9.2(g).

9.2 Results and discussion

Figure 9.2(a), (b), and (c) are the IR images recorded just before setting the pressure (0 min), and 10 min and 40 min after setting P_H = 1 bar, respectively. The images are showing the top view of the thin film. The sample is outlined by white dashed lines, which show two regions of different IR intensities: the region A of the film (with thickness increasing from right to left) and region B, which has the exposed substrate surface. Before hydrogenation (Fig. 9.2(a)), the region A is significantly darker than region B. After 10 min under 1 bar of hydrogen (Fig. 9.2(b)), we observed that the bright region moved some distance inside the film. At the same time, the region B became brighter. As the experiment continued, the bright region gradually expanded to the thicker parts of the film (see Fig. 9.2 (c)). Finally, after about 5 hours of hydrogenation, the intensity of the whole film became uniform and comparable to the intensity of the exposed substrate region. In XRD patterns obtained after completion of the hydrogenation experiment (24 h) (Fig. 1(c)), a reflection peak of the Mg (002) plane had almost disappeared, but instead, reflection peaks of MgH_2 (110) (2θ = 27.91) and MgH_2 (101) (2θ = 35.73) are observed. This indicates near-complete hydrogenation of the film at 100 ˚C. After completion of the hydrogenation experiment, the small reflection peak of Mg (002) was still observed. This may be because some amount of hydrogen was released from the sample while it was transferred from the chamber to the XRD machine.

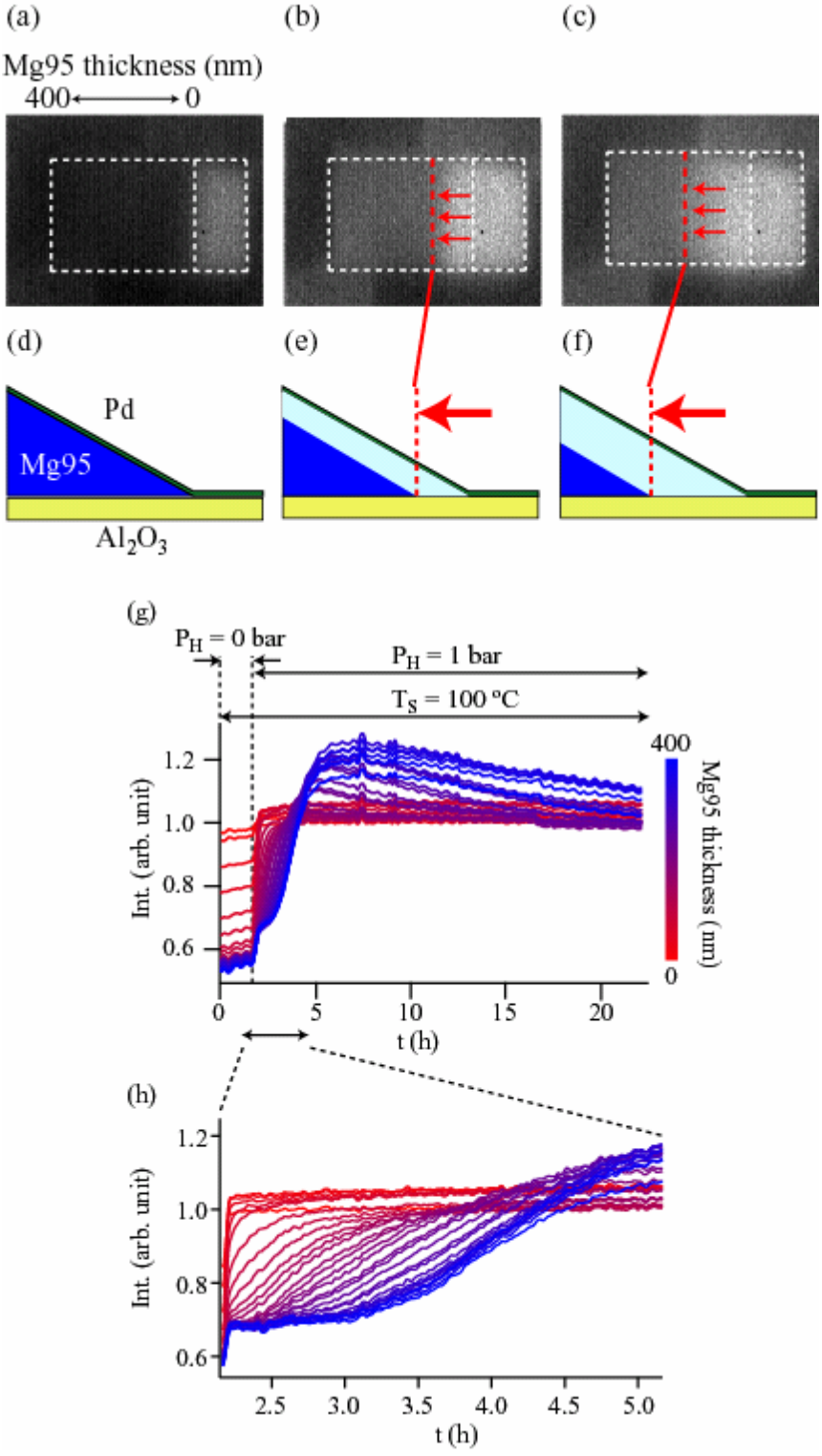
(a)
(b)
(c)
Mg95 thickness (nm)
400
0
(d)
(e)
(f)
Pd
Mg95
Al_2O_3
(g)
P_H = 0 bar
P_H = 1 bar
T_S = 100 °C
Int. (arb. unit)
t (h)
400
0
Mg95 thickness (nm)
(h)
Int. (arb. unit)
t (h)

Fig. 9.2 IR image of the Mg95 thickness gradient thin film at (a) 0 min, (b) 10 min, and (c) 40 min after setting the hydrogen gas pressure to 1 bar. Cross-sectional schematic of (a), (b), and (c) are shown in (d), (e), and (f), respectively. (g) Normalized IR intensity curves of 25 measurement points. Hydrogen gas pressure (P_H) and sample temperature (Ts) are denoted at the top of the graphs.

In order to explain our observations, we assume the formation of a MgH_2 hydride layer uniformly under the Pd layer as it is shown schematically in Fig. 9.2(d)-(f). From Fig. 9.2(a) and (d) it is clear the IR contrast between A and B regions has been formed by the strong emissivity of Al_2O_3, low emissivity of the metallic film and low transmission of the substrate radiation through the metallic film.[119-121] With the formation of a hydride layer, Fig. 2(b) and (e), an upper part of the film becomes much less conductive, and its IR emissivity increases. Moreover, for the thinner parts of the film, the hydride phase exists throughout its thickness and therefore is able to transmit the strong emissivity radiation of Al_2O_3.[119] Thus, the brightest part of the sample expands, and the dark/bright boundary moves to the left, as seen in Fig. 9.2(b-c) and (e-f). With this picture in mind, the thickness of the transformed hydride layer $\Delta\delta$ at any given time can be estimated from the change in the position of the dark/bright boundary Δl between A and B regions: $\Delta\delta = h_0 \frac{\Delta l}{l_0}$, where h_0 and l_0 are the height and the length of the wedge film, respectively. By tracking the propagation of the front line of the dark-to-bright transition, we can directly observe the dynamics of the formation of the hydride. Assuming that the

speed of hydride formation is constant throughout the measurement, we estimate the rate as 5 nm/min.

25 spots (every ≈ 0.4 mm) were selected along the thickness gradient to follow the changes of IR intensity with time at each spot during the experiment. Fig 9.2(g) shows the 25 normalized intensity curves (IR intensity of a selected spot / IR intensity of the substrate) as a function of time (t). A blow up of the initial 3 h data after setting P_H = 1 bar is shown in Fig. 2(h). The film thickness of each spot is represented by the curve color according to the color bar on right-hand side. The first evident change was observed when the P_H was set to 1 bar. In a short time, the curves with thinner Mg95 (red) were reached ≈ 1.0 and saturated. This means that the thinner Mg95 was completely converted into magnesium hydride, and the IR emission from the bottom of the Mg95 was detected. In contrast, the curves with thicker Mg95 (blue) showed slower increase in their intensity for ≈ 1 h, and then showed the second rapid increase until they saturated at around 5 h. This change can be explained in such a way that 1) the first rapid increase in intensity was due to the formation of the magnesium hydride (higher IR imissivity) at the surface of the Mg95 (lower IR emissivity), 2) the second rapid increase due to reaching of the hydride to the substrate, and 3) the slower increase due to the gradually increased volume of hydride with higher IR emissivity. After reaching the maximum, intensity of those curves decreased and approached 1.0. We guess, on each curve, that the effects of increase in IR emissivity due to optical property change and due to increase in local temperature (magnesium hydride formation is exothermic reaction)[122] take place together. The latter effect was pronounced with the thickness of the Mg95 as the total heat of

formation of the hydride was proportional to the volume of the Mg95. Therefore, the curves showed more overshoot with thicker Mg95. The effect was negligible with Mg95 thinner than 220 nm.

The microstructure of another Mg95 sample identically prepared experienced hydrogenation up to ≈ half of total thickness is under investigation using transmission electron microscopy (TEM) to confirm that the hydride formation front propagates from top to bottom of the thin film, and that the saturation in IR intensity curves corresponds to completion of hydride formation.

The Mg95 thin film was converted to hydride throughout its thickness when the intensity of the curve saturated. Thus we could tell, by tracking the saturation of each curve, how long it took to hydride a particular thickness of the Mg95 thin film throughout its thickness. Therefore, plotting thickness of the Mg95 thin film of each intensity curve against time it took from setting P_H = 1 bar to saturate (red cross of Fig. 9.3), the speed of formation of a hydride phase could be quantitatively studied. The saturation time was extracted from the sigmoid fitting curve of the each raw intensity curve. The results from another sample measured separately were also added to the figure (blue triangles). The only difference between these samples was how quickly the hydrogen gas was injected. When data of each sample was collected, the hydrogen gas pressure was set to 1 bar quickly (within less than 5 seconds), and slowly (less than 60 seconds) for samples with blue and red data points, respectively. Figure 9.3 indicates that the hydride formation behavior of each sample was composed of two parts, namely, the initial fast formation (region I) then followed by the slower formation (region II). For each part, data points were almost on the straight

fitting line. By fitting the data points of each parts, the speed of the hydride formation (nm/min) was obtained from the slope of the straight line. Comparison of the data trend of two samples indicated that velocity of propagation of hydride phase was faster when the hydrogen gas was injected more quickly. We guess the key to understand this behavior is the formation of the hydride cover layer at the surface of the thin film. Before the formation of the cover layer, hydrogen atoms might be able to diffuse into Mg95 rather easily, but once the cover layer is formed, it disturbs the hydrogen diffusion, and the slower formation of the hydride phase ensures.

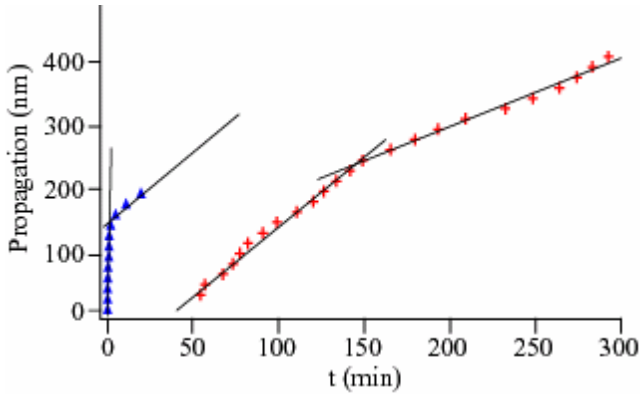

Fig. 9.3 Propagation depth of hydride as a function of time after setting the hydrogen gas pressure to 1 bar. Straight fitting lines are added as the guide to the eye.

When the hydrogen gas was injected quickly (blue), completion of hydride formation up to 140 nm (blue) within less than 2 min agrees with the reported hydride formation behavior of Mg-Ti thin films.[95]

9.3 Conclusion

In summary, the kinetics of the propagation of magnesium hydride formation into Mg95 was directly observed by making a thickness gradient thin film on an Al_2O_3 (0001) substrate using IR imaging. Analysis of the IR images collected in the process of hydrogenation of the Mg95 revealed that the formation of hydride composed of two steps: initial rapid propagation in region I and the second slower propagation in region II. The speed of the hydride formation determined from the slope of the straight-fitting lines were 1.7 ~ 98.4 nm/min for region I and 1.1 ~ 2.2 nm/min for region II.

Chapter 10 Conclusions and future work

10.1 Conclusion

Combinatorial synthesis using electron beam (e-beam) deposition has been used to systematically explore and evaluate a variety of intermetallics. We have developed a new combinatorial e-beam deposition chamber where the shadow deposition is achievable for both co-deposition and layer-by-layer deposition. By changing the mask design and mask motion, composition gradient and thickness gradient, which allow systemtic and detailed investigation of physical properties as a function of changing composition and thickness, of different layout designs can be fabricated. We have looked at intermetallic systems including exchange-coupled soft/hard magnetic bilayers, and hydrogen storage Mg-(transition metal)s (TM).

In order to study the effect of the soft magnetic layer on the exchange coupling, we have fabricated Fe_xCo_{1-x}/CoPt, Ni/CoPt, Co/CoPt, Fe/Sm_2Co_7, Ni/Sm_2Co_7, and Co/Sm_2Co_7 soft/hard magnetic bilayer samples. By using a magneto-optical Kerr effect (MOKE) measurement set up, we have observed continuous change in hysteresis loops, which delineated the one-phase-like to two-phase-like transition in exchange coupling between the soft layer and the hard layer. The exchange length (λ_x), which is the thickness of the soft layer at which the first sign of two-phase-like behavior is observed, is used to quantitatively evaluate the exchange coupling dependence on different magnetic parameters. We have found that λ_x is almost proportional to the inverse of magnetization of the soft layer. We also found that λ_x is decreased if the domain wall width of the hard layer is large.

In order to study the effect of grain-mixturing of the hard layer, which results in easy axes pointing in various directions, on the exchange coupling, we have made three Fe/CoPt soft/hard magnetic gradient bilayer samples. The crystallinity of the CoPt hard layer was controlled by changing the deposition temperature and post-deposition heat treatment. We found stronger exchange coupling between the soft layer and the hard layer when there is less grain-mixturing of the CoPt hard layer. This indicates that the exchange coupling efficiency can be maximized by tuning the crystallinity of the hard layer.

In order to study the effect of dipolar interaction between the soft phase and the hard phase on the exchange coupling, we have made Fe/Cu/CoPt soft-magnetic/non-magnetic/hard-magnetic trilayers with continuously varied Cu layer thickness. We used the nucleation field (H_N) from magnetic thin film trilayer systems to probe the role played by the soft-hard dipolar interaction. The value of the dipolar field (H_d) was determined by fitting the behavior of H_N as a function of thickness of the Cu non-magnetic layer. We found a proportional relationship between H_d and the interface roughness of the CoPt hard layer. In addition, H_d increased for increased grain size of the CoPt hard layer up to ≈ 14 nm, then it decreased to ≈ 0 for further grain size.

To rapidly detect hydrogen absorption and desorption of the combinatorial thin film samples, we have developed a new infrared (IR) imaging set up.

In order to systematically study hydrogen absorption and desorption properties dependence on composition, we have fabricated $Mg_x(TM)_{1-x}$ (TM = Ni and Ti) composition spreads. IR imaging experiments with hydrogenation of $Mg_x(TM)_{1-x}$

composition spreads have convincingly demonstrated that the method is able to capture reaction of the films with hydrogen gas; increase in intensity with absorption and decrease with desorption. IR imaging revealed that kinetics, equilibrium pressure, and amount of hydrogen reaction, of absorption and desorption changes continuously with changing composition.

In order to directly observe dynamics of transformation of Mg-Ti thin films into hydride, we have fabricated $Mg_{0.95}Ti_{0.05}$ (Mg95) thickness gradient thin films. By observing the IR images, we found that formation of hydride propagates from top of the thin film. Analysis of the IR images revealed that the speed of hydride formation is ≈ 5 nm/min provided that the speed of hydride formation is constant throughout the measurement.

10.2 Future work

There are a variety of other interesting experiments related to the investigation of the exchange-coupled magnets and hydrogen storage materials discussed in this thesis. Here, we list some ongoing and future work.

10.2.1 Exchange-coupled magnet

A. Optimization of the $SmCo_5$ hard layer. $SmCo_5$ is considered to be a better hard phase to enhance the energy product ($(BH)_{max}$) of the exchange-coupled magnets due to its large coercive field and saturation magnetization compared with CoPt and Sm_2Co_7. There are a variety of reports of successful synthesis of $SmCo_5$ layers using various deposition techniques.[123-125] However, a reproducible method for

achieving stable $SmCo_5$ thin films is still lacking due to the high vapor pressure of Sm. We will optimize the deposition rate of Sm and Co, deposition temperature, thickness and deposition temperature of the Cr buffer layer, annealing time, and cooling rate in order to obtain high quality $SmCo_5$ layers.

B. $SmCo_5$ hard layer thickness. In order to enhance $(BH)_{max}$ of the exchange-coupled magnets in soft/hard magnetic bilayer systems, infinitely thin hard layer is preferable because of the higher total magnetization of the system. However, our preliminary experiments showed that the thinner the hard layer, the more it is softened by the presence of the soft layer, if the thickness of the hard layer is less than its domain wall width. We will find the optimum thickness of the $SmCo_5$ hard layer by making gradient $Fe/SmCo_5$ soft/hard thin films.

C. $Fe/SmCo_5$ multilayers. Fabrication of $Fe/SmCo_5$ soft/hard magnetic multilayers have already been reported.[124] However, the reported $(BH)_{max}$ is still lower than the value theoretically predicted. In order to enhance $(BH)_{max}$, we can optimize the thickness of the Fe soft layer and the $SmCo_5$ hard layer, and modify the growth conditions.

10.2.2 Hydrogen storage materials

A. Microstructure dependence. There are many reports of relationship between hydrogen absorption and desorption properties and microstructure of the hydrogen storage materials.[106-111] We can systematically control the microstructure of the thin film samples by means of tuning the growth temperature or trying different types of substrates. IR imaging of these samples will give us detailed

relationship between hydrogen absorption and desorption properties and the microstructure of the hydrogen storage materials.

B. $Mg_x(TM)_{1-x}$ thickness gradient thin films. As discussed in this thesis, we established a new method which enables us to study dynamics of transformation of the hydrogen storage thin film materials into hydride using IR imaging of the thickness gradient thin film. By applying this method to $Mg_x(TM)_{1-x}$ composition spreads with different transition metals, we will reveal detailed kinetics dependence on composition, and find the best composition showing the fastest absorption and desorption.

C. $Pd_x(TM)_{1-x}$ composition spread capping layer. Pd is often used as a capping layer to protect the hydrogen storage materials from oxidization and facilitate splitting of hydrogen molecules at its surface. However, Pd is very expensive and amount in the ore is not so abundant. So far, there is few report of new capping layers. Using combinatorial synthesis of $Pd_x(TM)_{1-x}$ composition spread capping layers on the hydrogen storage materials such as Mg, we may discover a new compound having comparable or better properties than Pd.

References

[1] X. D. Xiang, and P. G. Schultz, *Physica C* **428**, 282-287 (1997).

[2] X. D. Xiang, X. Sun, G. Briceno, Y. Lou, K. A. Wang, H. Chang, W. G. Wallace-Freedman, S, W. Chen, and P.G.. Schultz, *Science* **268**, 1738 (1995).

[3] J. C. Phillips, Physics of High-Tcc Superconductors, Academic Press, New York, (1989).

[4] H. Chang, I. Takeuchi, and X. D. Xiang, *Appl. Phys. Lett*. **74**, 1165 (1999).

[5] I. Takeuchi, H. Chang, C. Gao, P. G. Schultz, X. D. Xiang, R. P. Sharma, M. J. Downers, and T. Venkatesan, *Appl. Phys. Lett.* **73**, 894 (1998).

[6] J. Wang, Y. Too, C. Gao, I. Takeuchi, X. Sun, H. Chang, X. D. Xiang, and P. G. Schultz, *Science* **279**, 1712 (1998).

[7] H. Chang, C. Gao, I. Takeuchi, Y. Yoo, J. Wang, P. G. Schultz, X. D. Xiang, R. P. Sharma, M. Downes, and T. Venkatesan, *Appl. Phys. Lett.* **72**, 2185 (1998)..

[8] I. Takeuchi, O. O. Famodu, J .C. Read, M. A. Aronova, K. S. Chang, C, Craciunescu, S. E. Lofland, M. Wutting, F. C. Wellstood, L. Knauss, and A. Orozco, *Nature Materials* **2**, 180 (2003).

[9] D.A. R. Barkhouse, A. Bonakdarpour, M. Fleischauer, T. D. Hatchard, and J. R. Dahn, *J. Magn. Magn. Mater.* **261**, 399 (2003).

[10] M. Yu, H. Oguchi, A. J. Zambano, I. Takeuchi, J.P. Liu, D. Josell, and L. A. Bendersky, *Mater. Sci. Eng. B* **142**, 139 (2007).

[11] T. FUkumura, M. Ohtani. M. Kawasaki, Y. Okimoto, T. Kageyama, T. Koida, T. Hasegawa, Y. Tokura, and H. Koinuma, *Appl. Phys. Lett.* **77**, 3426 (2000).

[12] G. Briceno, H. Chang, X. Sun, P. G. Schultz, and X. D. Xiang, *Science* **270**, 273 (1995).

[13] T. Takeuchi, D. Fukuma, and J. Matsui, *Anal. Chem.* **71**, 285 (1999).

[14] M. Gross, D. C. Muller, H. C. Nothofer, U. Sherf, D. Neher, C. Brauchle, and K. Meerhoz, *Nature* **405**, 661 (2000).

[15] C. H. Reynolds, *J. Comb. Chem.* **1**, 297 (1999).

[16] S. Sakahara, K. Yajima, R. Belosludoy, S. Takami, M. Kubo, and A. Miyamoto, *Appl. Surf. Sci.* **189**, 253 (2002).

[17] J. D. Hewes, and L. A. Bendersky, *Appl. Surf. Sci.* **189**. 196 (2002).

[18] M. Tirrell, E. Kokkoli, M. Biesalski, *Surf. Sci.* **500**, 61 (2002).

[19] J. C. Zhao, Prog. *Mater. Sci.* **51**, 557 (2006).

[20] J. M. Tarascon, C. Delacourt, A. S. Prakash, M. Morcrette, M. S. Hegde, C. Wurm, abd C. Masquelier, *Dalton Trans.*, **2988** (2004)

[21] S. H. Lim, M. Murakami, J. H. Yang, S. Y. Young, J. Hattrick-Simpers, M. Wuttig, L. G. Salamanca-Riba, and I. Takeuchi, *Appl. Phys. Lett.* **92**, 01298 (2008).

[22] Y. Yamada, T. Fukumura, M. Ikeda, M. Ohtani, H. Toyosaki, A. ohtomo, F. Matsukura, H. Ohno, and M. Kawasaki, *J. Supercond.* **18**, 109 (2005).

[23] C. J. Long, J. Hattrick-Simpers, M. Murakami, R. C. Srivastava, I. Takeuchi, V. L. Karen, and X. Li, *Rev. Sci, Instrum.* **78**, 072217 (2007).

[24] I. Takeuchi, C. J. Long, O. O. Famodu, M. Murakami, J. Hattrick-Simpers, and G. W. Rudloff, *Rev. Sci. Instrum.* **76**, 062223 (2005).

[25] R. Gremaud, C. P. Broedersz, D. M. Borsa, A. Borgschulte, P. Mauron, H. Schreuders, J. H. Rector, R. Dam, and R. Griessen, *Adv. Mater.* **19**, 2813 (2007).

[26] C. Kittel, Introduction to Solid State Physics, John Wiley & Sons, Inc., New York, 1996 (Chapter 2).

[27] A. K. Zvezdin, and V. A. Kotov, Modern Magnetooptics and Magnetooptical Materials, Institute of Physics Publishing, Bristol, 1997 (Chapter 1 and 3).

[28] R. D. Hudson, Infrared System Engineering, John Wiley & Sons, Inc., New York, 1969 (Chapter 2).

[29] S. Chikazumi, Physics of Magnetism, John Wiley & Sons, Inc. New York, 1964 (Chapter 2).

[30] C. Kittle, *Rev. Mod. Phys.* **21**, 542 (1949).

[31] J. M. D. Coey, *J. Magn. Magn. Mater.* **248**, 441 (2002).

[32] T. Chin, *J. Magn. Magn. Mater.* **209**, 75 (2000).

[33] P. Campbell, Permanent Magnet Materials and their Application, Cambridge University Press, 1994 (Chapter 1)

[34] J. F. Herbst, *Rev. Mod. Phys.* **63**, 819 (1991).

[35] M. Sagawa, S. Hirosawa, H. Yamamoto, S. Fujimura, and Y. Matsuura, *Jpn. J. Appl. Phys.* **26**, 785 (1987).

[36] J. J. Croat, J, F, Herbst, R. W. Lee, and F.E. Pinkerton, *J. Appl. Phys.* **55**, 2078 (1984).

[37] G. C. Hadjipanayis, R. C. Hazelton, and K. P. Lawless, *J. Appl. Phys.* **55**, 2073 (1984).

[38] N. C. Koon, and B, N, Das, *J. Appl. Phys.* **55**, 2063 (1984).

[39] J. F. Herbst, J. J. Croat, F.E. Pinkerton, and W.B. Yelon, *Phys. Rev.* **29**, 4176 (1984).

[40] E. F. Kneller, and R. Hawig, *IEEE Trans. Magn.* **27**, 3588 (1991).

[41] R. Skomski, and J. M. D. Coey, *Phys. Rev. B* **48**, 15812 (1993).

[42] E. Goto, N. Hayashi, T. Mitashita, and K. Nakagawa, *J. Appl. Phys.* **36**, 2951 (1965).

[43] R. Fischer, T. Schrefl, H, Kronmüller, and J. Fidler, *J. Magn. Magn. Mater.* **150**, 329 (1995).

[44] E.C. Stoner, and E. P. Wohlfrath, *Philos. Trans. R. Soc. London, Ser. A* **240**, 599 (1948).

[45] T. Leineweber, and H. Kronmüller, *J. Magn. Magn. Mater.* **176**, 145 (1997).

[46] H. Ono, N. Waki, M. Shimada, T. Sugiyama, A. Fujiki, H. Yamamoto, M. Tani, *IEEE Trans. Magn.* **37**, 2552 (2001).

[47] J. Zhang, Y. K. Takahashi, R. Gopalan, and K. Hono, *Appl. Phys. Lett.* **86**, 122509 (2005).

[48] H. Zeng, J. Li, J. P. Liu, Z. L. Wang, and S. Sun, *Nature* **420**, 395 (2002).

[49] J. S. Jiang, J. E. Pearson, Z. Y. Liu, B. Kabius, S. Trasobares, D. J. Miller, S. D. Bader, D. R. Lee, D. Haskel, G. Srajer, and J. P. Liu, *J. Appl. Phys.* **97**, 10K311 (2005).

[50] Hong-wei Zhang, Shao-ying Zhang, Bao-gen Shen, and Helmut Kronmüller, *J. Magn. Magn, Mater.* **260**, 352 (2003).

[51] Eckart F. Kneller, *Member, IEEE*, and Reinhard Hawig, *IEEE Trans. Mag.* **27**, 3588 (1991).

[52] Z. J. Guo, J. S. Jiang, J. E. Pearson, S. D. Bader, and J. P. Liu, *Appl. Phys. Lett.* **81**, 2029 (2002).

[53] A. J. Zambano, H. Oguchi, I. Takeuchi, Y. Choi, J. S. Jiang, J. P. Liu, S. E. Lofland, D. Josell, and L. A. Bendersky, *Phys. Rev. B* **75**, 144429 (2007).

[54] Ralph Skomski and J. M. D. Coey, *Phys. Rev. B* **48**, 15812 (1993).

[55] R. Fischer, T. Leineweber, and H. Kronmüller, *Phys. Rev. B* **57**, 10723 (1998).

[56] M. R. Pufall, W. H. Rippard, and T. J. Silva, *Appl. Phys. Lett.* **83**, 323 (2003).

[57] M. Murakami, S. Fujino, S.-H. Lim, L. G. Salamanca-Riba, M. Wutting, I. Takeuchi, B. Varughese, H. Sugaya, T. Hasegawa, and S. E. Lofland, *Appl. Phys. Lett.* **88**, 112505 (2006).

[58] M. Abes, O. Ersen, C. Meny, G. Schmerber, M. Acosta, J. Arabski, C. Ulhaq-Bouillet, A. Dinia, P. Panissod, and V. Pierron-Bohnes, *J. Appl. Phys.* **101**, 063911 (2007).

[59] H. Zeng, J. Li, J. P. Liu, Z. L. Wang and S. Sun, *Nature* **420**, 395-398 (2002).

[60] C. Rong, H. Zhang, R. Chen, S. He and B Shen , *J. Magn. Magn. Mater.* **302,** 126-136 (2006).

[61] L.S. Birks, H. Friedman, *J. Appl. Phys.* **17**, 687 (1946).

[62] P. Bruno and C. Chappert, *Phys. Rev. Lett.* **67**, 1602 (1991).

[63] M. A. Ruderman, and C. Kittel, *Phys. Rev.* **96**, 99 (1954).

[64] D.T. Margulies, M.E. Schabes, W. Mc. Chesney and E.E. Fullerton, *Appl. Phys. Lett.* **80**, 91 (2002).

[65] S. S. P. Parkin and D. Mauri, *Phys. Rev. B* **44**, 7131 (1991).

[66] S. T. Chui, *J. Appl. Phys.* **85**, 4397 (1999).

[67] DOE 2007 Annual Merit Review Proceedings Hydrogen Storage, http://www.hydrogen.energy.gov/annual_review07_storage.html

[68] L. Schlapbach and A. Zuttel, *Nature*, **414**, 353 (2001)

[69] B. Dam, R. Gremaud, C. Broedersz, and R. Griessen, *Scripta Materialia*, **56** 853 (2007)

[70] C. H. Olk, G. G. Tibbetts, D. Simon, and J.J. Moleski, *J. Appl. Phys.*, **94**, 720 (2003)

[71] G. Soloveichik, J. Lemmon, J. Cui, Y. Gao, T. Raber, J. Rijssenbeek, G. Rubinzstajn, and J.C. Zhao, DOE Presentation, (2007) http://www1.eere.energy.gov/hydrogenandfuelcells/pdfs/ht_ge_soloveichik.pdf

[72] D. Sperling, M. A. DeLuchi, Ann. *Rev. Energy* **14**, 375 (1989).

[73] a) C. C. Elam, C. E. G. Padr, G. Sandrock, A. Luzzi, P. Lindblad, E. F. Hagen, *Int. J. Hydrogen, Energy* **28**, 601 (2003). B) J. A. Ritter A. D. Ebner, J. Wang, R. Zidan, *Mater. Today* September, 18 (2003).

[74] M. Conte, A. Iacobazzi, M. Ronchetti, R. Vellone, *J. Power Sources* **100**, 171 (2001).

[75] T. Honma, Nenryo-denchi no Subete, Kogyo Chosa Kai, Japan (2003).

[76] M.A. Paevey, Fuel from Water, Merit, Louisville, KY 1998.

[77] P. Hoffmann, The forever Fuel, Westview Press, Boulder, CO 1981.

[78] R. M. Dell D. A. J. Rand, *J. Power Sources* **100**, 2 (2001).

[79] B. D. McNicol, D. A. J. Rand, K. R. Wiliams, *J. Power. Sources* **100**, 47 (2001).

[80] A. B. Stambouli, E. Traversa, *Renewable Sustainable Energy Rev.* **6**, 297 (2002).

[81] M. Z. Jacobson, W. G. Colella, and D. M. Golden, *Science* **308**, 1901 (2005).

[82] K. Hashimoto, T. Kawai, and T. Sakata, *J. Phys. Chem.* **88**, 4083 (1984).

[83] W. Deng, X. Xu, and W. A. Goddard, *Phys. Rev. Lett.* **92**, 166103-1 (2004).

[84] J. M. Ogden, M. M. Stenbugler, T. G. Kreutz, *J. Power Sources* **79**, 143 (1999).

[85] G. D. Berry, S. M. *Aceves, Energy Fuels* **12**, 49 (1998).

[86] S. Louis, Hydrogen in Intermetallic Compounds I, in: Topics in Applied physics, Vol. 63, Springer, Berlin p.350 (1988).

[87] DOE Basic Research Needs for the Hydrogen Economy (February 2004) http://www.sc.doe.gov/bes/hydrogen.pdf

[88] K. Chlopek, C. Frommen, A. Léon, O. Zabara, and M. Fichtner, *J. Mater. Chem.* **17**, 3496 (2007).

[89] B. Bogdanovic, R. A. Brand, A. Marjanovic, M. Schwickardi, and J. Tolle, *J. Alloy. Compd.* **302**, 36 (2000).

[90] L. Pan, M. B. Sander, X. Huang, J. Li, M. Smith, E. Bittner, B. Bockrath, and J. K. Johnson, *J. Am. Chem. Soc.* **126**, 1308 (2004).

[91] A. M. Seayad and M. Antonelli, *Adv. Mater.* **16**, 765 (2004).

[92] L. Schlapbach, I. Anderson, J. P. Burger, in Electronic and Magnetic Properties of Metals and Ceramics Part III, Vol.3B. (Ed: K. H. J. Buschow), VCH, Weinheim, Germany pp.271 (1994).

[93] M. Planck, The Theory of Heat Radiation, Dover, New York (1991).

[94] B. Farangis, P. Nachimuthu, T.J. Richardson, J. L. Slack, R.C.C. Perera, E.M. Gullikson, D. W. Lindle, and M. Rubin, *Phys. Rev. B*, **67**, 85106 (2003)

[95] D.M. Borsa, R. Gremaud, A.Baldi, H. Schreuders, J.H. Rector, B. Kooi, P. Vermeulen, P.H.L. Notten, *Phys. Rev. B*, **75**, 205408 (2007)

[96] J.L. Murray in Binary Alloys Phase Diagrams, Second Edition, Ed. T.B. Massalski, ASM International Materials Park, Ohio (1990), p. 2559

[97] W. Lohstroh, R. J. Westerwaal, J. L. van Mechelen, C. Chacon, E. Johansson, B. Dam, and R. Griessen, *Phys. Rev. B*, **70**, 165411 (2004)

[98] J.L. Murray in Binary Alloys Phase Diagrams, Second Edition, Ed. T.B. Massalski, ASM International Materials Park, Ohio (1990), p. 2559

[99] DOE Targets for on-board hydrogen storage systems, http://www1.eere.energy.gov/hydrogenandfuelcells/storage/current_technology.html

[100] A. Zuttel, P. Wenger, S. Rentsch, P. Sudan, P. Mauron, and C. Emmenegger, *J. Power Sources* **118**, 1 (2003.)

[101] Y. Nakamori, and S. Orimo, *J. Alloys Compd.* **370**, 271 (2004).

[102] T. Kohno, H. Yoshida, F. Kawashima, T. Inaba, I. Sakai, M. Yamamoto, and M. Kanda, *J. Alloys Compd.* **311**, L5 (2000).

[103] B. Bogdanovic, and M. Schwichardi, *J. Alloys Compd.* **253**, 1 (1997).

[104] M. Hirscher, M/ Becher, M. Haluska, U. Dettlaff-Weglikowska, A. Quintel, G. S. Duesberg, T. M. Choi, P. Downes, M. Hulman, S. Roth, I. Stepanek, and P. Bernier, *Appl. Phys. A* **72**, 129 (2001).

[105] Yildrim, and S. Ciraci, *Phys. Rev. Lett.* **94**, 175501 (2005).

[106] S. Orimo, and H. Fujii, *Appl. Phys. A* **72**, 167 (2001).

[107] R. Schulz, J. Huot, G. Liang, S. Boily, G. Lalande, M. C. Denis, and J. P. Dodelet, *Mater. Sci. Eng. A* **267**, 240 (1999).

[108] L. Zaluski, A. Zaluska, J. O. StromOlsen, *J. Alloys Compd.* **253**, 70 (1997).

[109] C. Suryanarayana, and C. C. Koch, *Hyperfine Interact.* **130**, 5 (2000).

[110] N. Cui, P. He, and J. L. Luo, *Acta. Mater.* **47**, 3737 (1999).

[111] J. Huot, G. Liang, R. Schulz, *Appl. Phys. A* **72**, 187 (2001).

[112] P. H. Notten, and P. Hokkeling, *J. Electrochem. Soc.* **138**, 1877 (1991).

[113] A. Zaluska, L. Zaluski, and J. O. Ström-Olsen, *Appl. Phys. A* **72**, 157 (2001).

[114] C. M. Jensen, and K. J. Gross, *Appl. Phys. A* **72**, 213 (20001).

[115] G. Barkhordarian, T. Klassen, and R. Bormann, *Scr. Mater.* **49**, 213 (2003).

[116] J. J. Vajo, S. L. Skeith, and F. Mertens, *J. Phys. Chem. B* **109**, 3719 (2005).

[117] F. Schüth, B. Bogdanović, and M. Felderhoff, *Chem. Commun.* **2249** (2004).

[118] A. M. Seayad, and D. M. Antonelli, *Adv. Mater.* **16**, 765 (2004).

[119] J. Isidorsson, I. A. M. E. Giebels, H. Arwin, and R. Griessen, *Phys. Rev. B* **68**, 15112 (2003).

[120] P. van der Sluis, M. Ouwerkerk, and P. A. Duine, *Appl. Phys. Lett.* **70**, 3356 (1997).

[121] I. A. M. E. Giebels, J. Isidorsson, E. S. Kooij, A. Remhof, N. J. Koeman, J. H. Rector, A. T. M. Van Gogh, and R. Griessen, *J. Alloys Compd.* **330**, 875 (2002).

[122] C. Rongeat, I. Llamas-Jansa, S. Doppiu, S. Deledda, A. Borgschulte, L. Schultz, and O. Gutfleisch, *J. Phys. Chem. B* **111**, 13301 (2007).

[123] A. Singh, V. Neu, R. Tamm, K. Rao, S. Faehler, W. Skrotzki, L. Schultz, and B. Holzapfel, *J. Appl. Phys.* **99**, 08E917 (2006).

[124] J. Zhang, Y. K. Takahashi, R. Gopalan, and K. Hono, *Appl. Phys. Lett.* **86**, 122509 (2005).

[125] J. Sayama, T. Asahi, K. Mizutani, and T. Osaka, *J. Phys. D: Appl. Phys.* **37**, L1 (2004).